UC San Diego

UC San Diego Electronic Theses and Dissertations

Title

PEDOT:PSS/Parylene C ECoG Microelectrode Arrays for Multi-Modal Recording of Brain Activity in Birds and Rodents

Permalink

https://escholarship.org/uc/item/3zt68534

Author

Hossain, Lorraine Amena

Publication Date

2020

Peer reviewed|Thesis/dissertation

eScholarship.org Powered by the California Digital Library
University of California

UNIVERSITY OF CALIFORNIA SAN DIEGO

PEDOT:PSS/Parylene C ECoG Microelectrode Arrays for Multi-Modal Recording of Brain Activity in Birds and Rodents

A dissertation submitted in partial satisfaction of the requirements for the degree Doctor of Philosophy

in

Materials Science and Engineering

by

Lorraine Amena Hossain

Committee in charge:

Professor Shadi Dayeh, Chair
Professor Timothy Gentner, Co-Chair
Professor Anna Devor
Professor Eric Halgren
Professor Tse Nga Ng
Professor Paul Yu

2020

Copyright

Lorraine Amena Hossain, 2020

All rights reserved.

The Dissertation of Lorraine Amena Hossain is approved, and it is acceptable in quality and form for publication on microfilm and electronically:

_____

_____

_____

_____

_____
Co-Chair

_____
Chair

University of California San Diego

2020

DEDICATION

I would like to wholeheartedly dedicate this dissertation to my parents, whose continued love and support made all the difference. Even though I was on the other side of the country, you both proved that love overcomes geographical distance, through countless virtual hugs, cheerful cards with nostalgic baby photos, and our yearly tradition of cruises – which sadly ends this year. Thank you for believing in me even when I had trouble believing in myself. Love you so much, Amma and Abba!

TABLE OF CONTENTS

SIGNATURE PAGE iii
DEDICATION iv
TABLE OF CONTENTS v
LIST OF ABBREVIATIONS vii
LIST OF SYMBOLS viii
LIST OF FIGURES ix
LIST OF TABLES xii
ACKNOWLEDGEMENTS xiii
VITA xv
ABSTRACT OF THE DISSERTATION xvii
INTRODUCTION 1
Chapter 1 Fabrication and Characterization of PEDOT/Parylene C Devices 5
1.1 Device form factor development 5
1.2 Monolithic nanofabrication process 6
1.3 Fabrication of Au nanorod devices to enhance PEDOT:PSS adhesion 11
1.4 Electrochemical characterization of devices 13
1.5 Longevity effect on devices 14
Chapter 2 Recording of Stimulus Locked Single Units in Songbirds 16
2.1 Experimental Design 18
2.2 Combined surface and depth probe recording 19
2.3 Subject Selection and Stimuli Generation 20
2.4 Acute recordings in anesthetized songbirds 21
2.5 Data processing of electrophysiology 23
2.5.1 Spike Sorting and Unit Characterization 23
2.5.2 Cross Correlation Analysis 24
2.5.3 Analysis of Stimulus Evoked Response 25
2.6 Comparison between surface and depth electrophysiology 26
2.6.1 Comparison of Depth- and Surface-Recorded Single Unit Waveform Characteristics 27
2.6.2 Correlation Between Putative Surface SUA and Depth SUA 28
2.6.3 Auditory Stimulus Driven Modulation of Putative Surface SUA and Depth SUA 30
2.7 Discussion 32

Chapter 3 Diameter and material dependence for recording single unit activity 37
3.1 Experimental Design 37
3.2 Diameter and material dependence analysis 38
3.3 Combined form factor for diameter and material dependence analysis 48
Chapter 4 Multimodal Chronic Recordings in Awake Mice 55
4.1 Sensitivity verification in acute setting 56
4.2 Chronic recording setup in awake subjects 58
4.2.1 Custom device connectivity 58
4.2.2 Electrophysiology recording 63
4.2.3 Calcium imaging using 2-photon microscopy 66
4.3 Behavioral electrophysiological recordings and calcium imaging 67
4.4 Single unit analysis 69
4.5 Discussion 70
Chapter 5 Conclusion 72
REFERENCES 73

LIST OF ABBREVIATIONS

AuNR	Gold Nanorod
CSF	Cerebral Spinal Fluid
ECoG	Electrocorticography
EIS	Electrochemical Impedance Spectroscopy
HPF	High Pass Filter
ISI	Inter-Spike-Interval
LFP	Local Field Potential
LPF	Low Pass Filter
MUA	Multi-Unit Activity
PBS	Phosphate-Buffered Saline
PCA	Principle Component Analysis
PCB	Printed Circuit Board
PEDOT:PSS	Poly(3,4-ethylenedioxythiophene) polystyrene sulfonate
PlAu	Planar Gold
PtNR	Platinum Nanorod
SNR	Signal to Noise Ratio
SUA	Single-Unit Activity

LIST OF SYMBOLS

kHz	Kilohertz
kΩ	Kiloohm
MΩ	Megaohm
µm	Micron
mm	Millimeter
ms	Millisecond
nm	Nanometer

LIST OF FIGURES

Figure 1 Two-step mask design for chronic electrocorticography arrays 6

Figure 2 Fabrication procedure for PEDOT:PSS/Parylene C Microelectrodes 9

Figure 3 Optical images of a sample device at different stages of the fabrication procedure 10

Figure 5 Imaging of device 11

Figure 6 Fabrication procedure for nanorod devices 12

Figure 7 Electrode comparison between planar Au and the Au nanorod structure 13

Figure 8 Electrochemical impedance spectroscopy for 32 electrode PEDOT:PSS/parylene C array with 20µm diameter size 14

Figure 9 Aging study on device 14

Figure 10 Histogram of electrode impedance measured at 1kHz before, during, and after an implantation in vivo in Starling birds 15

Figure 11 Experimental paradigm and example spiking activity 19

Figure 12 Single unit characteristics 27

Figure 13 Cross-correlograms 29

Figure 14 Stimulus driven responses. 31

Figure 15 Device geometry for varying diameter experiment 37

Figure 16 Classification of unit labeling: single unit, multi-unit, noise, and artifact 38

Figure 17 Comparison on the same dataset for two different spike sorting software: Spike2 (A-B) and Kilosort (C-D) 39

Figure 18 Peak to trough amplitude of the average waveform for single units vs. electrode diameter comparison between two spike-sorting software: Spike2 and Kilosort 40

Figure 19 Device geometry for 64 channel variable diameter array 41

Figure 20 Impedance measured in both saline solution and in vivo at 1kHz for large scale variable diameter device 42

Figure 21 Average waveform of single units for three electrode materials: PtNR, PEDOT:PSS, and Planar Au 43

Figure 22 Amplitude vs. Diameter for different electrode interfaces 43

Figure 23 Baseline standard deviation vs. diameter and signal to noise ratio vs. diameter for different electrode interfaces 44

Figure 24 Example full width half max calculation for a single unit 45

Figure 25 Full width half max vs. diameter for three electrode materials. 46

Figure 26 Full width half max vs. spike rate for three electrode materials. 46

Figure 27 Peak-to-trough vs. spike rate for units detected from three different materials 47

Figure 28 Device geometry for variable diameter multi-material device 49

Figure 29 HPF electrophysiology data for electrodes with the same material (PEDOT:PSS) and varying diameters 50

Figure 30 Raw electrophysiology data of electrodes with the same diameter (80 µm) and varying material 50

Figure 31 Waveform of single unit detected across three electrodes with varying material 51

Figure 32 Common reference subtraction to remove noise artifact from target trace 52

Figure 33 High pass filtered traces of common reference subtraction analysis 52

Figure 34 Periodograms to determine the frequencies to remove through notch filtering 53

Figure 35 Noise removal through notch filtering 54

Figure 36 Localized electrophysiological response in acute setting 57

Figure 37 Chronic device form factor with Omnetic connector 59

Figure 38 Chronic implantation with custom PCB utilizing Molex connector 60

Figure 39 Importance of bonding device to glass window prior to implantation 60

Figure 40 Optimized chronic device 61

Figure 41 Custom headstage for chronic rodent implants 62

Figure 42 Recording setup for chronic recording of an awake mouse 62

Figure 43 Impedance measurements of chronic implants for up to 60 days 63

Figure 44 Trial averaged electrophysiological response to optogenetic stimulation on two electrodes 64

Figure 45 Trial average electrophysiological response to sandpaper stimulation for two electrodes 65

Figure 47 Two-photon imaging of cortical column through an implanted parylene C/PEDOT:PSS device..... 66

Figure 48 Simultaneous Ca imaging and electrophysiology in chronically implanted, awake mice 68

Figure 49 High frequency activity detection in response to airpuff stimulation 69

Figure 50 Time locking of the mouse motion..... 70

LIST OF TABLES

Table 1 Single unit characterization and statistics 24

Table 2 Number of single units significantly with auditory onset for each subject 32

Table 3 Diameter and impedance for common reference analysis 51

ACKNOWLEDGEMENTS

I would like to express my sincere gratitude to Professor Shadi Dayeh for his support as the chair of my committee and as my faculty advisor. His guidance and mentorship has greatly shaped my graduate school experience and continues to inspire me.

I would also like to extend my gratitude to my co-advisor Professor Timothy Gentner for his insightful input to my research and positive reinforcements, to my collaborator and faculty committee member Professor Anna Devor for her thorough feedback to strengthen my research and faith in my ability to promote our research at conferences, to my collaborator and faculty committee member Professor Eric Halgren for his mentorship on signal processing, to my faculty committee member Professor Tina Ng for her clear instructions in the fundamentals of semiconductors, and to my faculty committee member Professor Paul Yu for his knowledge on GaN LED fabrication that helped create the initial framework of my graduate research.

I would like to acknowledge my past and present IEBL lab members, Atsunori Tanaka, Mehran Ganji, YunGoo Ro, Hongseok Oh, Sang Heon Lee, Keundong Lee, Youngbin Tchoe, Woojin Choi, Andrew Bourhis, Samantha Russman, Ritwik Vatsyayan, Po Chun Chen, Jihwan Lee, Tianhai Wu, Namseok Park, Ren Liu, Renjie Chen, Joonseop Sim, Nasim Vahidi, Ahmed Taha El-Thakeb, Siarhei Vishniakou, Supanee Sukrittanon, and Keisuke Matsushita. Additionally, I would like to acknowledge my collaborators, Martin Thunemann, Ezequiel Arneodo, Kıvılcım Kılıç, John Hermiz, Nick Rogers, Dan Cleary, and Srihita Rudraraju.

Chapter 2, in full, is a reprint of the material as it appears in Frontiers in Neuroscience, 2020. Hermiz, John; Hossain, Lorraine; Arneodo, Ezequiel; Ganji, Mehran; Rogers, Nicholas; Vahidi, Nasim; Halgren, Eric; Gentner, Timothy Q.; Dayeh, Shadi A.; Gilja, Vikash, Frontiers, 2020. The dissertation author was the primary author of this paper with two other first co-authors.

The statistical analysis reported in the paper was conducted by fellow first co-author Dr. John Hermiz.

Chapter 3, in part, is currently being prepared for submission for publication of the material. Hossain, Lorraine; Arneodo, Ezequiel M.; Oh, Hongseok; Gentner, Timothy Q.; Dayeh, Shadi A. The dissertation author will be the primary author of this material.

Chapter 4, in part, is currently being prepared for submission for publication of the material. Hossain, Lorraine; Rogers, Nick; Oh, Hongseok; Lee, Keundong; Lee, Sang Heon; Kılıç, Kıvılcım; Gilja, Vikash; Devor, Anna; Dayeh, Shadi A.; Thunemann, Martin; The dissertation author will be the primary author of this material.

VITA

2015	Bachelor of Science, The Pennsylvania State University
2015-2020	Research Assistant, University of California San Diego
2016	Master of Science, University of California San Diego
2020	Doctor of Philosophy, University of California San Diego

PUBLICATIONS

Eichfeld S, Eichfeld C, Lin Y, Hossain L, Robinson J (2014). Rapid, non-destructive evaluation of ultrathin WSe_2 using spectroscopic ellipsometry. APL Materials 2, 092508.

Azizi A, Eichfeld S, Geschwind G, Hossain L, *et al*. (2015) Freestanding van der Waals Heterostructures of Graphene and Transition Metal Dichalcogenides. ACS Nano, 9 (5) 4882-4890.

Browning P, Eichfeld S, Zhang K, Hossain L, *et al*. (2015) Large-area synthesis of WSe_2 from WO_3 by selenium-oxygen ion exchange. 2D Materials. 2, 014003.

Eichfeld S, Hossain L, Lin Y, Robinson J, *et al*. (2015) Highly Scalable, Atomically Thin WSe2 grown via Metal-Organic Chemical Vapor Deposition. ACS Nano. nn5073286.

Ganji M, Hossain L, Tanaka A, Thunemann M, *et al.* (2018) Monolithic and Scalable Au Nanorod Substrates Improve PEDOT-Metal Adhesion and Stability in Neural Electrodes. Advanced Healthcare Materials, 7, 1800923.

Ganji M, Paulk A, Yang J, Vahidi N, Lee SH, Liu R, Hossain L, *et al*. (2019) Selective Formation of Porous Pt Nanorods for Highly Electrochemically Efficient Neural Electrode Interfaces. Nano Letters 19 (9), 6244-6254.

Rogers N, Hermiz J, Ganji M, Kaestner E, Kılıç K, Hossain L, *et al*. (2019) Correlation Structure in Micro-ECoG Recordings is Described by Spatially Coherent Components. PLoS Comput Biol 15 (2), e1006769.

Paulk A, Yang J, Cleary D, Soper D, Lee SH, Ganji M, Ro YG, Oh H, Hossain L, *et al.* (2019) Microscale physiological events on the human cortical surface detected with PEDOT:PSS Electrodes. bioRxiv, 770743.

Paulk A, Yang J, Cleary D, Soper D, Halgren M, O'Donnell A, Lee SH, Ganji M, Ro YG, Oh H, Hossain L, *et al.* (submitted) Microscale physiological events on the human cortical surface. PNAS.

Hermiz J*, Hossain L*, Arneodo EM*, Ganji M, *et al.* (2020) Stimulus Driven Single Unit Activity From Micro-Electrocorticography. Front. Neurosci. 14:55. (*first authors)

FIELDS OF STUDY

Major Field: Material Science and Engineering

Studies in MgZn diffusion couples

Professor Zi-Kui Liu

Studies in process property relations of MOCVD grown WSe_2 thin films
Professor Joshua Robinson

Studies in MOCVD selective area growth of GaN LEDs
Professor Shadi Dayeh

Studies in fabrication and characterization of microelectrode arrays
Professor Shadi Dayeh

Studies in electrophysiology recordings and neural signal processing
Professors Shadi Dayeh, Timothy Gentner, and Anna Devor

ABSTRACT OF THE DISSERTATION

PEDOT:PSS/Parylene C ECoG Microelectrode Arrays for Multi-Modal Recording of Brain Activity in Birds and Rodents

by

Lorraine Amena Hossain

Doctor of Philosophy in Materials Science and Engineering

University of California San Diego, 2020

Professor Shadi Dayeh, Chair

Professor Timothy Gentner, Co-Chair

Understanding cognitive processing in intact brains is the subject of intense research efforts that aim to resolve individual and network activity of neuronal cells across different layers of the brain. While efforts to record a large number of individual cellular activity in intact brains are underway, the network-level coordinated activity of neurons result in long-range, low frequency

oscillations that carry significant electrophysiological information and is the gold standard for recording neural correlates of cognition from animals and humans. Recently, recording of individual cellular activity, commonly referred to as single units, with high signal-to-noise ratio from the cortical surface was accomplished. Critical to this milestone in electrophysiology was the use of organic microelectrode arrays that (1) possess superior electrochemical junction characteristics enabling them to have contact diameters that are similar to neuronal sizes yet while maintaining low electrochemical impedances and low noise, and (2) enable conformal coverage of thin parylene C device carrier layers to the brain curvature. The small contact diameter, and therefore listening sphere, its low noise, and its intimate contact with the surface of the brain are all attributed as essential conditions to permit the recording of single unit activity from the brain's surface.

This thesis appraises the development of novel microelectrode arrays that record single units from the brain's surface, and their application in recording brain activity from anesthetized and awake animal models. The first part of the dissertation discusses the application of Poly(3,4-ethylenedioxythiophene) polystyrene sulfonate, commonly known as PEDOT:PSS – a semiconductive polymer with excellent electrochemical properties – as well as microelectrode contacts that employ large surface area one-dimensional nanostructures, to the electrophysiological investigations in songbird experiments. Significantly, we observed strong correlation of surface-recorded single units with spectrotemporal features of replayed birdsongs across trials and that were also validated with simultaneously implanted depth electrodes. This finding has implications for minimally destructive brain-machine interfaces that can make use of surface-recorded units. Additionally, we carried out systematic investigations to understand the influence of the electrode contact diameter and the contact material on resolving single unit activity

from the surface of the brain. Our initial results suggest that contacts with lower impedances result in higher signal amplitude as well as higher biological noise amplitude, due to their sensitivity and that amplitude of single units generally decreases with diameter.

While acute recordings can streamline testing of neurotechnologies, chronic recordings are important for applications in which subjects can ultimately engage in behavioral experiments. To this end, the last part of this dissertation concerns with the development and optimization of a chronically stable device form factor. This device leverages the transparency of the parylene C substrate to perform simultaneous electrophysiological recording and multi-photon imaging of neuronal activity in awake mice. We recorded stimulus-evoked calcium indicator responses that correlated with local field potential (LFP) response and higher frequency multi-and single unit activity. This dissertation encompasses advances in the scalable, monolithic fabrication procedure for high-yield PEDOT:PSS microelectrode arrays on parylene C substrates and their utility of electrocorticography (ECoG) recording capability of neuronal activity from intact brains.

INTRODUCTION

The last decade witnessed an explosion of interest in brain mapping devices that often combined different modalities recently. This work concerns mainly with electrophysiological devices that are transparent to permit optical interrogation of the brain activity. Electrophysiological devices can interface with the brain by recording across the depth of the cortical layers and deep brain structures with depth electrodes or by recording the cumulative activity from the surface using surface electrodes.

Depths probes include the widely used Utah and Michigan arrays which are intracortical, that is, they penetrate into the tissue of the brain. While this allows for high resolution mapping of neuronal activity in the vicinity of the probes, the invasive nature of these probes causes tissue damage that facilitates biofouling and potential shielding of the electrode. Surface probes like electrocorticography (ECoG) devices are placed on the cortical surface without penetrating the brain tissue and are therefore less invasive. However, the greater separation of the contacts in ECoG devices from neurons reduce the spatiotemporal resolution when compared to depth probes. Several very exciting reports over the last few years from the Buzsáki and Malliaras labs demonstrated the detection of single unit activity from surface probes using thin conformal electrodes with conductive PEDOT:PSS coatings[1,2].

The surge in the development of neurotechnologies has already accelerated our understanding of brain function[3,4] and enabled new neuroprosthesis therapies[5–8]. ECoG technology[2,9–12] has been used in a variety of species as well as over different cortical areas and have shown much promise for chronic recordings of motor activity[13–15]. But existing clinical ECoG devices are built on thick silicone substrates and cannot conform to the curvilinear nature of the cortical surface. Maintaining a full contact with the brain can establish higher fidelity recordings

as demonstrated by Kim et al with the use of conformal and thinner polyimide substrates[16]. The use of flexible polymers like parylene provide adequate conformality and they can be fabricated on and then lifted off from sturdier carrier substrates[17].

In order to increase the spatial resolution of ECoG devices, contacts must be brought close together and their diameters must be decreased. But smaller diameters result in larger electrochemical impedances that is usually accompanied with higher noise and loss of signal fidelity. To enable such scaling, the electrode contact material properties must be developed such that they exhibit low electrochemical impedances at small diameters. Organic coatings offer one promising alternative to traditional metal electrodes. Khodagholy et al. utilized the conductive polymer Poly(3,4-ethylenedioxythiophene) polystyrene sulfonate (PEDOT:PSS) to record single unit activity from the surface of the brain[2]. Electrode made of hard materials, like Pt, rely on surface screening of charges and in some cases redox reactions to transduce electrochemical activity. The organic PEDOT:PSS enables intercalation of ions into the material permitting volumetric transduction of electrochemical activity with both capacitive charge screening and faradaic redox reactions and charge transfer. Therefore, the noise that correlates with the contact impedance is therefore reduced[18].

The electrochemistry of PEDOT:PSS is fascinating. Stavrinidou and collaborators measured ion mobility in PEDOT:PSS and found a reversible de-doping cycle with reproducible values after a few cycles[19]. The addition of secondary doping like sorbitol, poly-ethylene glycol, dimethyl sulfoxide (DMSO), N-methylpyrroloidone, N-dimethylformamide, and tetrahydrofuran can further increase conductivity by 2-3 orders, and can enhance properties even if fully removed from the electrodes[20]. Mechanisms behind this include reduced coulombic interaction by screening polar solvents, dipole interactions that change PEDOT chain conformation, and changing the

surface morphology by segregating excess PSS[20]. Starbird et al. created PEDOT aerogels exhibiting a skeletal density of 1.01 g/cm^3 and bulk density of 0.12 g/cm^3 through the use of a starch template to improve the impedance magnitude and phase of their electrodes[21]. Schander et al. reported on the stability of PEDOT from *in vivo* chronic experiments, further validating that PEDOT:PSS is a viable contender as a neural interface[22].

The minimally invasive nature of surface probes as compared to penetrating depth probes offers promising advantages regarding damage to the surrounding tissue, and can be especially useful in chronic implants. Indeed, mechanical trauma from insertion of depth probes has been shown to induce wound healing and edema, with necrotic tissues observed beyond six weeks after implant[23]. Biran et al. reported on chronic foreign body reaction after acute inflammatory response[24]. This can be observed with the presence of reactive astrocytes or glial scars and activated microglia[24,25]. Additionally, probes demonstrated a gradual downward displacement in addition to glial scar formation, which eventually caused electrode failure[26].

To reduce biofouling reactions in the tissue, several biotic/abiotic strategies can be implemented. Soft, biocompatible polymer substrates such as parylene-C, polyimide, and SU8 exhibit low Young's modulus to match the elasticity of the brain, however buckling can occur[27]. Another strategy for reducing tissue damage is to optimize the probe insertion condition as well as the probe design. Szarowski et al. argued that the probe geometry has little effect on glial scar formation[28]. The use of polymer coatings that locally release bioactive drugs can further reduce device encapsulation. Dexamethasone (DEX) and laminin-1 disperse astroglial scarring, and Chondroitinase ABC, nerve growth factor, brain-derived neurotrophic fact, and neurotrophin-3 can promote neural regeneration[29]. Researchers have also incorporated stiffening agents like polyethylene glycol, collagen, sugar, poly(lactic-co-glycolic acid), tyrosine-derived terpolymer,

chitosan, and dried silk fibroin from Bombyx Mori silkworms[27]. Reduced biofouling can increase the device lifetime, offering promising insight into long-term cognitive functions.

Chapter 1 Fabrication and Characterization of PEDOT/Parylene C Devices

1.1 Device form factor development

The fabrication procedure for the PEDOT:PSS/Parylene C microelectrode arrays is both monolithic and scalable, which enables modifications to the geometry of the device as well as individual layers within the device and therefore rapid device prototyping. The photo-definable electrode patterns were designed using L-edit software. Once a pattern was created, the design was printed in chrome onto a glass mask. This mask then shadowed the regions of the pattern during ultraviolet (UV) light exposure to the photoresist. Several electrode geometries were utilized, with features determined by the specific application. The recording system utilized ports of 32 channels, so the majority of the devices had 32 channels or some multiples of 32. The devices fabricated for the smaller animal models like songbirds and rodents typically had 32 electrodes with 20μm diameters to better isolate signals from individual neurons. The spatial coverage of these electrodes spans an area of nearly $1mm^2$. Figure 1 depicts the mask design for chronic surface recordings.

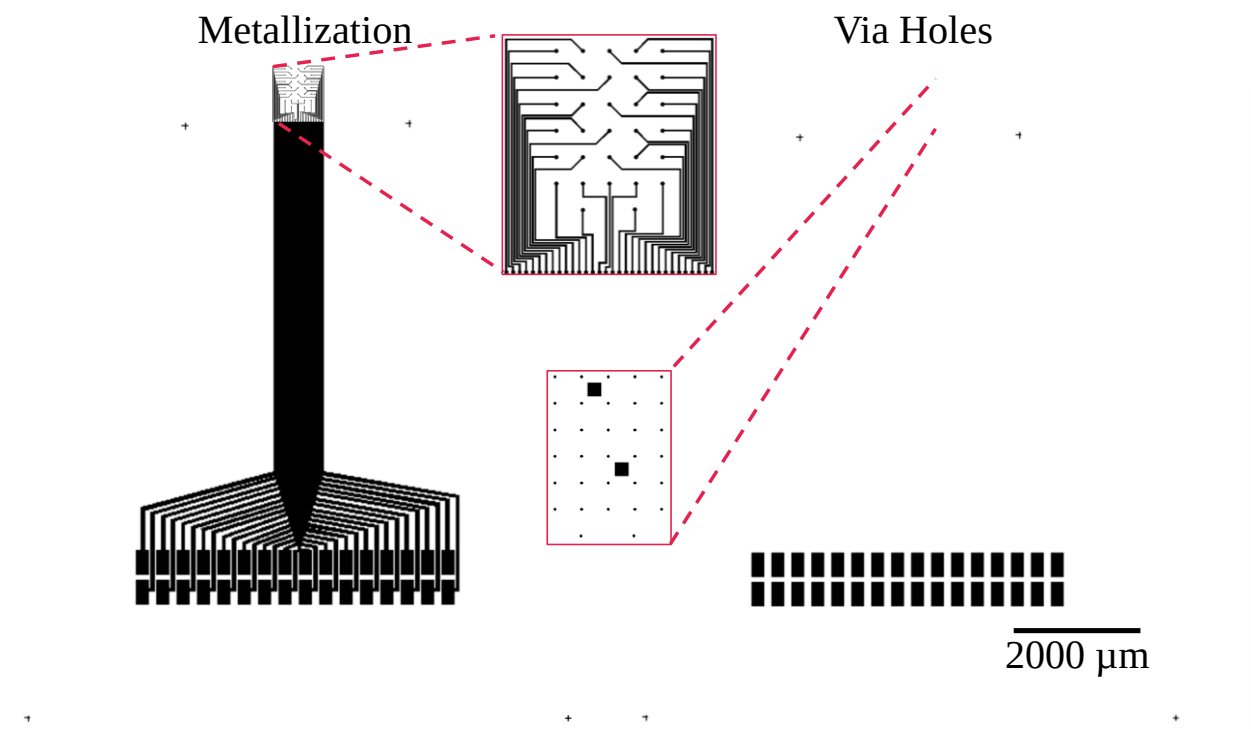


Figure 1 Two-step mask design for chronic electrocorticography arrays. The metallization mask defines the metal leads and has electrode diameters of 30µm. The via hole mask defines the exposed regions of metal - the electrode sites and connector pads – and has electrode diameters of 20µm.

There are four small cross marks at the corners of the masks; these were the alignment markers to overlay the via holes pattern over the metallization pattern. While the electrode and contact pad shape was the same for both the metallization and via holes masks, the size is slightly smaller for the via holes mask. For the metallization mask, the electrodes had a diameter of 30µm and the contact pads had a length of 430µm, whereas for the via holes mask, the dimensions were 20µm and 380µm for the electrode diameter and contact pads, respectively.

1.2 Monolithic nanofabrication process

Fabrication of these microelectrodes was conducted in a Class 100 Cleanroom facility for the photolithographic processes and a Class 1000 facility for the layer deposition and lift-off/etching. The process began with cleaning a sacrificial wafer, typically glass or silicon, by placing the wafer in a beaker filled with acetone, ultrasonicating for 5 minutes in acetone,

transferring to a beaker of isopropyl alcohol, ultrasonicating for 5 minutes in isopropyl alcohol, removing the wafer from solution, rinsing with isopropyl alcohol, rinsing with deionized water, and drying with a nitrogen gun. Then an anti-adhesion layer of micro90 diluted with deionized water (0.1%) was spun-coated at 1050 rpm onto the wafer and allowed to air-dry. Through chemical vapor deposition (CVD), a process in which an aluminum boat filled with solid parylene C dimer is heated up until the dimer is sublimed into a vapor which evenly coats the pressurized chamber containing the wafers. A PDS 2010 Parylene Coater was used to deposit the base parylene C substrate at thickness of ~2.1-2.5μm. Thicknesses of individual layers were measured using a Dektak 150 Surface Profiler. Next photolithography was conducted to pattern the metal electrodes and leads. A 6μm thick layer of NR9-3000 photoresist was spin-coated and soft baked onto the wafer, followed by UV exposure using a Karl Suss MA6 Mask Aligner beneath a mask mentioned in section 1.1, a hard bake, development involving light agitation in RD6 developer solution, and a rinse with deionized water. Following a one minute oxygen descum step in an Oxford Plamaslab 80+ RIE to activate the surface, a BJD 1800 Ebeam Evaporator was used to deposit a 10nm thick Ti layer and a 100nm thick Au layer by electron beam evaporation. This process entailed orienting a beam of thermionically emitted electrons from a heated filament tip onto an inert crucible filled with the target metal. The target metal heats and evaporates, and under vacuum has a long diffusion length that leads to an even coating of the metal within the chamber. After extracting the cooled wafer from the Ebeam evaporator, the wafer is placed in an acetone bath to dissolve the patterned photoresist and lift-off the metal residing on top of the photoresist pattern, leaving behind Ti/Au in the shape of the electrode array. An additional one minute oxygen descum step in an Oxford Plamaslab 80+ RIE was then performed to roughen the parylene surface and improve the adhesion for the subsequent second layer of vapor-deposited parylene C, also at a thickness of ~2.1-2.5μm.

A less diluted layer of micro90 anti-adhesion (1%) was then spun-coated before depositing a third parylene C layer that was used in later steps as a sacrificial layer. The next layer was 2010 SU-8, which is a photodefinable epoxy slightly more robust than NR9 photoresists and is used to pattern a hard mask for etching the parylene C. The mask used to pattern the SU-8 consists of the electrode active sites and connector pads, as seen in Figure 1. The Oxford Plamaslab 80+ RIE is then used to dry etch through the parylene, leaving the remaining metal leads encapsulated and insulated. Next was a coating of the organic PEDOT:PSS solution, which consisted of 20 mL aqueous dispersion of PEDOT:PSS (pH 1000 from Clevios), 5 mL of ethylene glycol, 50 µL of dodecylbenzene sulfonic acid (DBSA), and 1 wt.% of (3-glycidyloxypropyl) trimethoxysilane (GOPS). This solution was spun-coated for 30s at 650 rpm, followed by evaporating off the solvents on a hotplate. Next, the sacrificial parylene C layer was peeled off so that PEDOT:PSS remained only on the contact region, and a thermal cure for one hour followed to allow the PEDOT:PSS polymer chains to crosslink and adhere to the electrode surface. Finally, the device was manually cut and separated from the hard carrier wafer to result in the conformal ECoG device. A summary of the fabrication is depicted below in Figure 2.

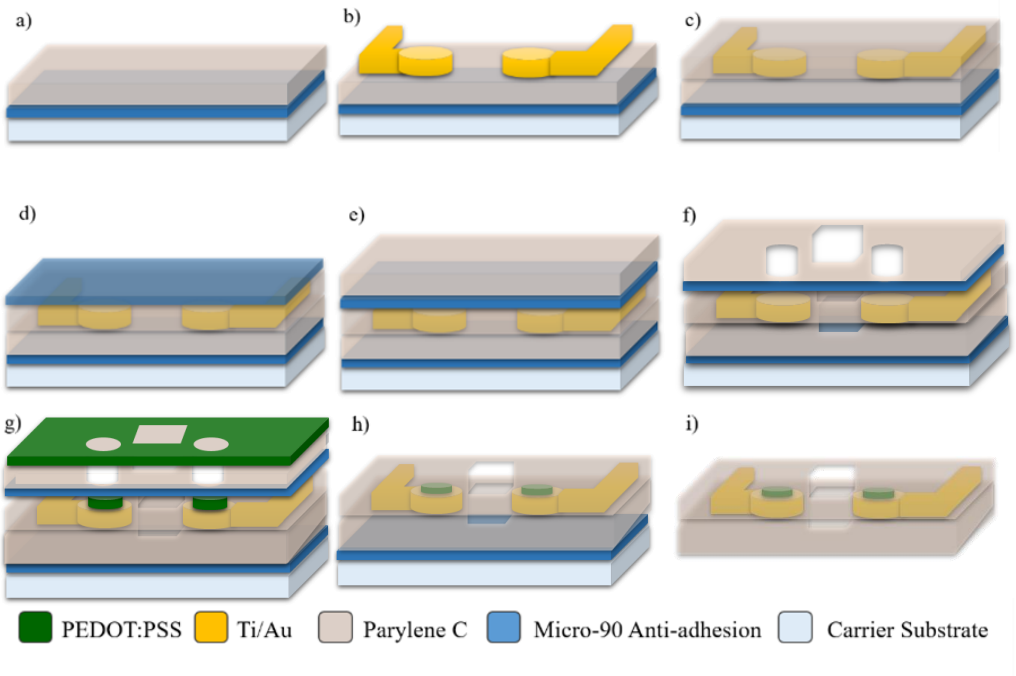


Figure 2 Fabrication procedure for PEDOT:PSS/Parylene C Microelectrodes. A First layer of parylene C deposited on carrier wafer with spun-coated anti-adhesion layer. B Metallization of Cr/Au electrode leads and contacts with electron beam deposition. C Encapsulation with the second parylene C layer. D Additional anti adhesion layer spin-coated. E Deposition of sacrificial third parylene C layer. F Via etching of the contact sites and perfusion holes, if applicable. G Spin-coating of PEDOT:PSS solution. H Delamination of the third parylene C layer and thermal curing of the PEDOT:PSS. I Final delamination of the device from the carrier wafer.

Images of the devices were acquired at various stages of the fabrication process through optical microscopy to validate the integrity of the device before proceeding to the next step.

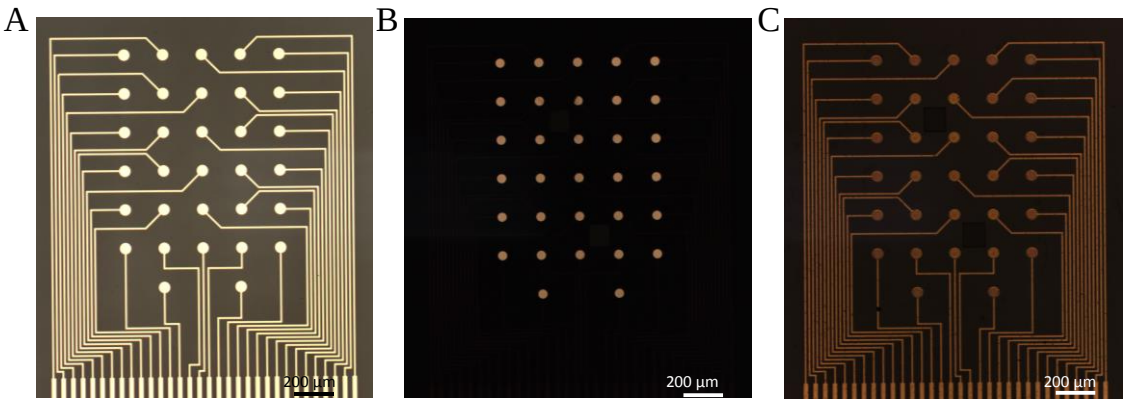


Figure 3 Optical images of a sample device at different stages of the fabrication procedure: A metallization, B via etching, and C PEDOT:PSS coating of electrodes.

Scanning electron microscopy with an FEI SFEG UHR SEM can provide further insight into the individual layers of the devices. The insulating nature of the parylene C substrate, however, introduces charging to the image, so the devices were coated with iridium prior to imaging to reduce the charging effect which can be noted in Figure 4A. The SEM image in Figure 4B and 4D shows that the PEDOT:PSS layer above the electrode has conformally coated the entire electrode. Upon removal of the charging effect seen in Figure 4A, uniform coating is seen across electrodes of varying diameters as seen in Figure 4C.

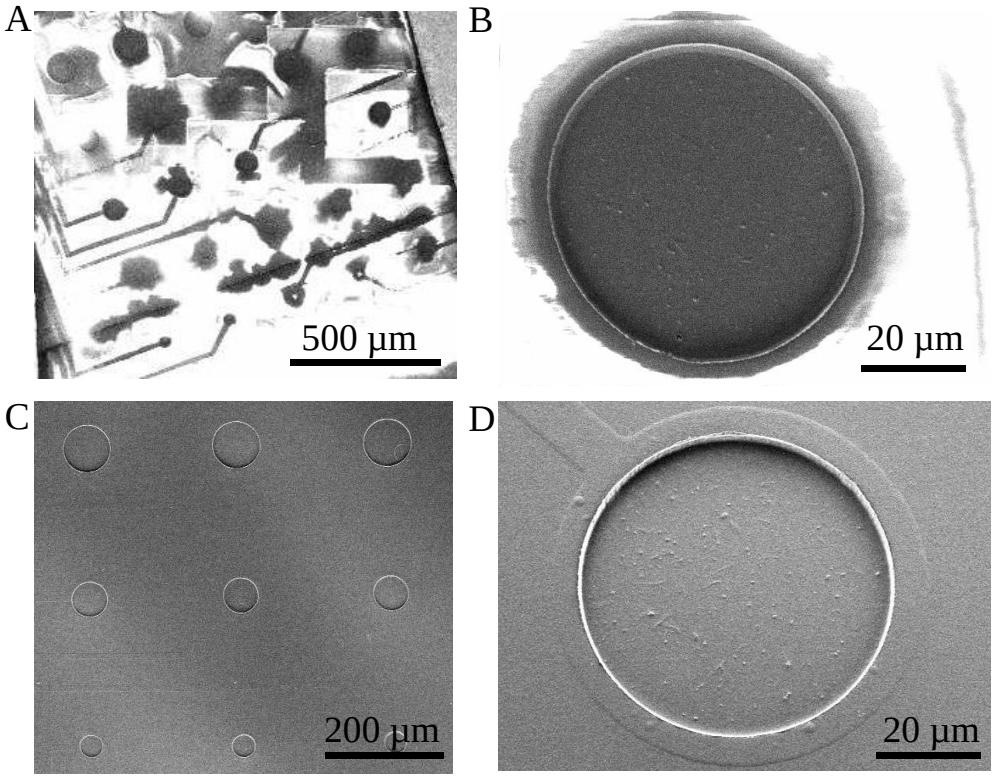


Figure 4 Scanning electron microscopy images of electrode. A and B depict the charging effect of the electron on insulating parylene C. C and D depict the improved imaging after coating the array with iridium before imaging.

This fabrication procedure is applicable for a wide variety of device geometries, with different electrode sizes and orientations, as well as with added features like perfusion and via holes. The device shown in Figure 5 has two square via holes, notably in Figure 5B and 5C, which

can aide in the conformality of the implant by allowing CSF fluid to escape from under the device as well as allow a window for a depth probe to be implanted for simultaneous surface and depth neural recording.

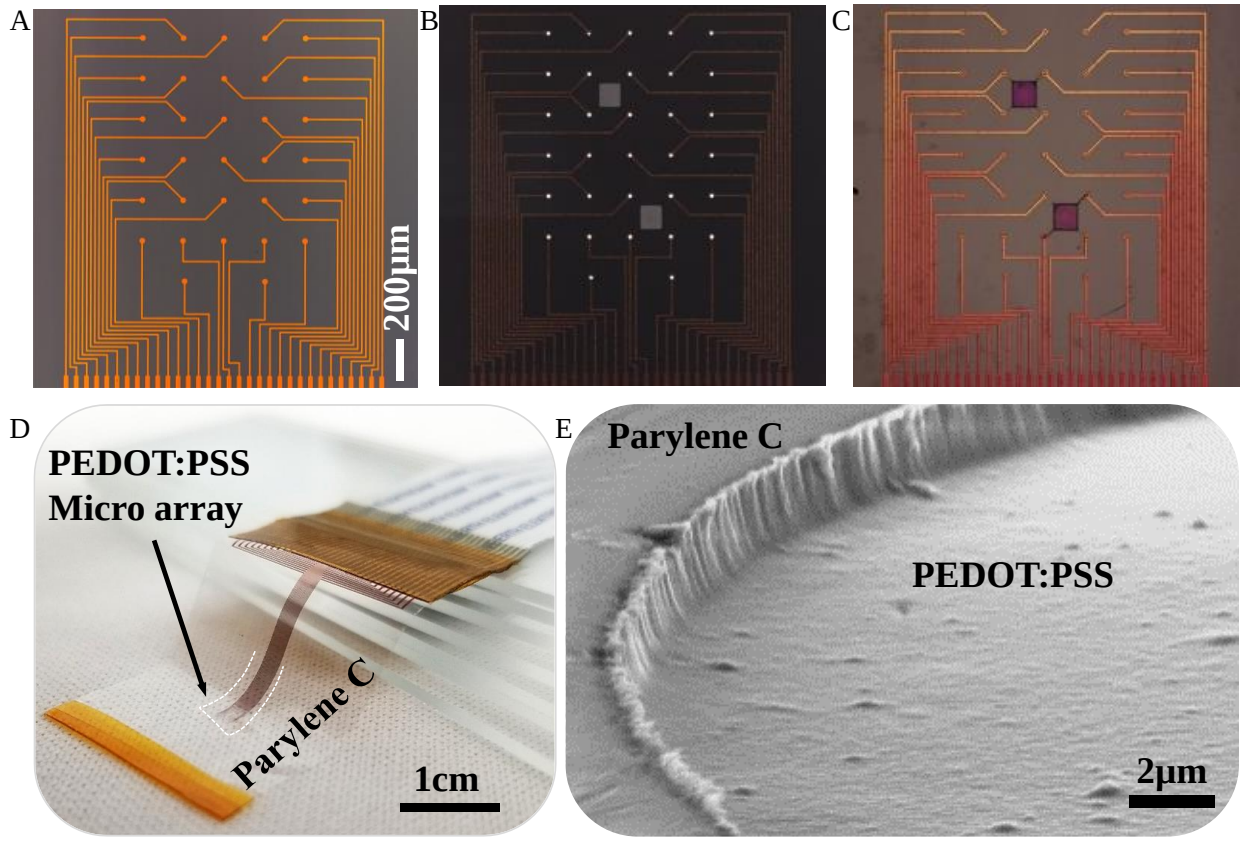


Figure 5 Imaging of device. A Optical images of device after metallization. B Optical image of device after via etching of the parylene C to expose electrode contact region. C Optical image of device after coating of PEDOT:PSS solution to the electrode contacts. Scale bar represents 200µm. D Use of parylene C as encapsulation layers allows the device to fit conformally to the cortical surface. Scale bar represents 1cm. E SEM image of electrode shows etched region of parylene C in which PEDOT:PSS is coated onto the metal electrode.

1.3 Fabrication of Au nanorod devices to enhance PEDOT:PSS adhesion

To further improve the adhesion of the Au-PEDOT:PSS interface, a modified procedure was used to increase the surface area of the Au layer[30]. The fabrication procedure begins similar to the planar Au process described in Section 1.3, including electron beam deposition for the metallization layer, in this case of a 15nm thick Cr adhesion layer and a 100nm thick Au contact layer. Then photolithography was conducted to selectively define the electrode sites, and a Denton

Discovery 18 Sputter System was used to add a base layer of 15nm Cr and 100nm Au, followed by a co-sputtered alloy of Au/Ag. The co-sputtering process switches between 400W RF power for Ag and 60W DC power for Au to achieve a thickness of about 0.5µm. This is followed by acetone liftoff of the negative photoresist and a dealloying step where the Ag is removed through a 2 minute submersion in nitric acid heated to 60°C. The subsequent steps follow those described in Section 1.2. A similar procedure was implemented with Pt instead of Au to produce Pt nanorod devices as well[31]. Figure 6 depicts the process for fabricating both Au nanorod (AuNR) and Pt nanorod (PtNR) electrodes.

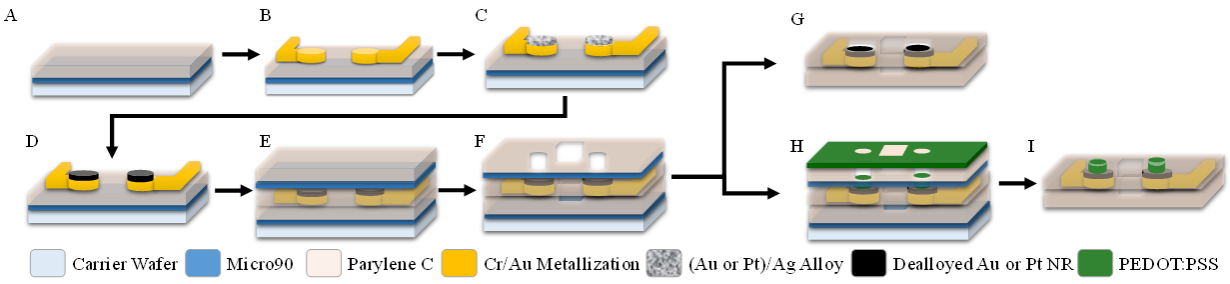


Figure 6 Fabrication procedure for nanorod devices. A First layer of parylene C deposited on carrier wafer with spun-coated anti-adhesion layer. B Metallization of Cr/Au electrode leads and contacts with electron beam deposition. C Patterning of either Au or Pt alloyed with Ag via sputtering. D Dealloying of the Ag from the (Au or Pt)/Ag alloy in heated nitric acid. E Encapsulation with the second and third parylene C layers. F Via etching of the contact sites and perfusion holes, if applicable. G Delamination of third parylene C layer and from the carrier wafer if fabricating PtNR electrodes. H Spin-coating of PEDOT:PSS solution if fabricating AuNR/PEDOT:PSS electrode. I Delamination of the third parylene C layer and from the carrier wafer of the AuNR/PEDOT:PSS device.

The three dimensional forest of Au or Pt nanorods causes the surface of the electrode to look much darker compared to the planar metal electrodes, as seen in Figure 6 and in Figure 7. The mark observed in all electrodes in Fig. 7 from both the planar and nanorod devices was caused from a defect in the via holes mask when etching the second and third parylene C layers. The roughened structure of the Au nanorod electrodes provided improved adhesion with PEDOT:PSS coatings[30].

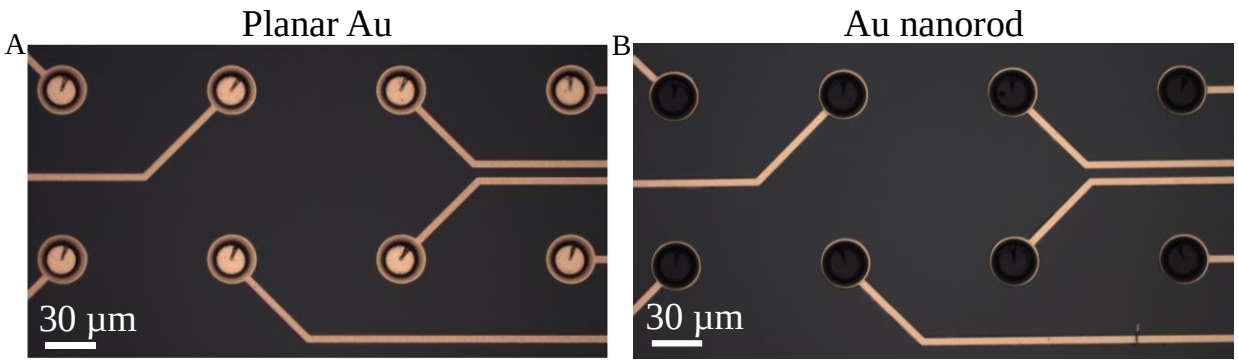


Figure 7 Electrode comparison between planar Au and the Au nanorod structure.

1.4 Electrochemical characterization of devices

To characterize the electrophysiological properties of the electrodes, we measure electrochemical impedance spectroscopy (EIS), which involves sending a current between a working electrode and counter electrode and measuring the potential drop with respect to the reference and measuring the ratio of the voltage to the current and the phase difference between the two. For in vitro testing, we use a conventional three terminal setup in phosphate-buffered saline (PBS) solution, with Ag/AgCl as our reference electrode, Pt as our counter electrode and our PEDOT:PSS device as the working electrode. In vivo recording utilizes Intan technology, which measures the impedance at 1 kHz. Figure 8 shows an example of electrochemical impedance spectra for 32 contacts with 20µm diameter. The spectra are nearly perfectly identical and show a narrow distribution in the impedance with an average of around 70kΩ at 1kHz. At lower frequencies, the impedance is dominated by capacitive coupling, whereas higher frequencies are more affected by series resistance seen as the phase approaches zero.

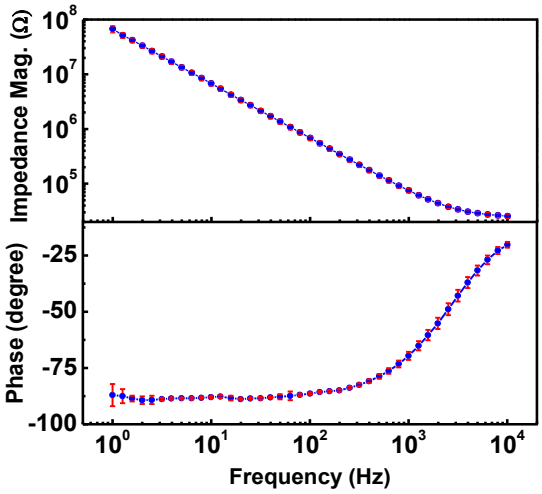


Figure 8 Electrochemical impedance spectroscopy for 32 electrode PEDOT:PSS/parylene C array with 20μm diameter size.

1.5 Longevity effect on devices

To determine the stability of the devices within semi-chronic implants, aging studies in heated saline were performed. The aging studies were conducted at 75°C for 2.2 days to simulate one month at body temperature. The device was secured to a glass wafer using kapton tape, and both the temperature and saline solution meniscus were monitored and adjusted consistently throughout the measurement. The EIS showed that there was minimal effect on the electrodes over this time frame.

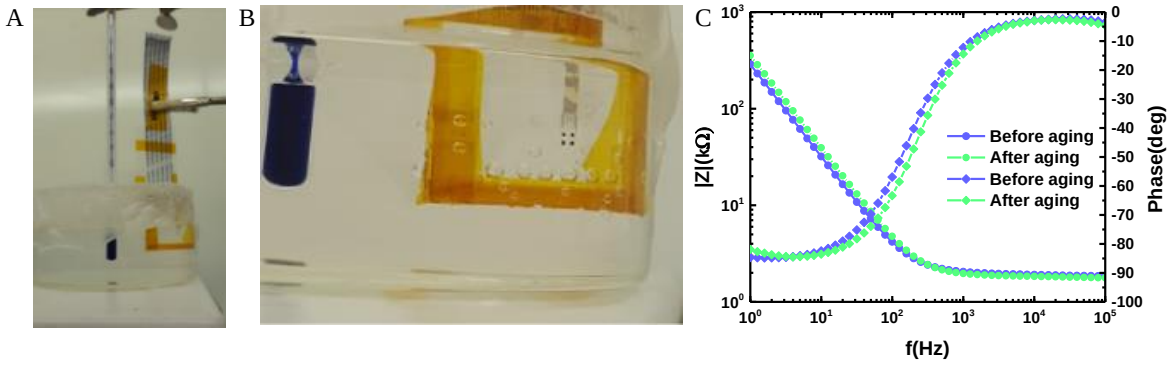


Figure 9 Aging study on device showed minimal change to the electrochemical impedance after 2.2 days in heated saline solution or-in effect-one month in vivo.

Additionally, the resilience of the electrodes to implantation effects was tested by comparing the EIS before, during, and after implantation *in vivo* in Starling birds as shown in Figure 10. Plotting the measured impedance at 1kHz for all 32 channels showed a narrow distribution prior to implantation. Upon implantation of the device during *in vivo* recordings, we observed greater variability in the impedance measurements compared to the ideal conditions in saline solution. A second impedance measurement during later stages of the recordings showed additional changes in the impedance. After removing the device from the subject and rinsing, the original impedance values for most except for two channels were recovered.

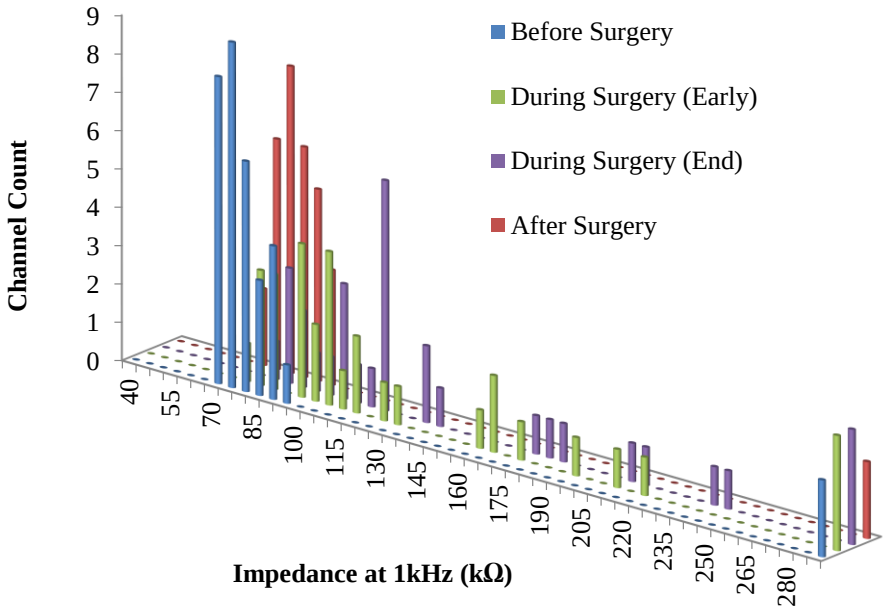


Figure 10 Histogram of electrode impedance measured at 1kHz before, during, and after an implantation in vivo in Starling birds.

Chapter 2 Recording of Stimulus Locked Single Units in Songbirds

Understanding how the brain manages and interprets language and speech is of profound importance for scientific and therapeutic pursuits. In the human model, complexities in language and synaptic responses hinder the full deconvolution of this model. Human experiments are also hard to conduct except during resection surgeries, which limits the freedom in the design of the behavioral experiments, and in specialized epilepsy monitoring. Nonhuman subjects can provide the opportunity to acquire a fundamental understanding of how animals process and produce sounds. Songbirds are a popular animal model to understand sound vocalization and sound production. Songbirds are believed to internalize sensory inputs and form vocal outputs with similar neural mechanisms to that of humans[32]. Prather et al. also reported several parallels in the neural network sound production in songbirds and humans, stating that while the mechanisms of language from a computational standpoint are unique to humans, the structuring of neural networks for sensorimotor learning and auditory perception in songbirds are very similar to that of humans[33]. Abe and Watanabe extended this conjecture further by stating that birds can provide a computational model for human speech due to their ability to instantaneously discriminate auditory stimuli through similar syntactic rules[34]. Melody recognition in songbirds is seen to depend on the overall spectral shapes of auditory stimuli rather than the need for pitch[35]. This finding challenged many traditional views that the discrimination of sound sequences without changes in pitch was a uniquely human[36–38]. Additionally, songbirds have been shown to utilize sparseness and normalization within the neural network to generate receptive fields to more complex stimuli patterns. Kozlov et al. developed a statistical method to neuronal response for natural stimuli like birdsong that is relatable to human speech[39]. In songbirds, the song system consists of discrete brain nuclei of hierarchical network with HVC at its top[40]. The HVC (motor vocal control nucleus)

is shown to be song-selective in zebra finches[41]. Differences between neural activity in zebra finches, white-crowned sparrows, and canaries suggest that HVC can provide insight to song perception across species[42]. Also spiking observed during auditory-only activity suggests that HVC has both auditory and motor functions[43]. Electrophysiology recorded in the HVC of anesthetized zebra finches with chronic bundles of isonel-insulated microwires or Pt-Ir electrodes showed varying response to the same syllable of birdsong under different contexts of a song motif[44]. In anesthetized starlings, researchers classified song motifs from bird's own song and conspecific song while recording electrophysiology with four tungsten wires insulated by epoxylite with impedances of 3-6 MΩ[45]. They found that the response of neurons to auditory stimulus was low and attributed this to having a large sample without preselection[45]. The response to bird's own song was mostly phasic with some sustained responses, however the conspecific song was not as tightly time-locked to stimulus[45]. Much more has been published on zebra finches, which have less complex song patterns. Electrophysiology recorded with nichrome wires coated with rhodium with impedances measuring between 200-800kΩ implanted into HVC showed that finches in the awake state exhibit suppression of response to auditory stimulus compared to anesthetized[46]. The paper also reports that preliminary recordings in RA also show the suppression of auditory response while awake[46]. Additionally, researchers at UC San Diego recorded electrophysiology in zebra finches while they were awake and singing using a 4 shank, 16/32 site Si Neuronexus probe coated with PEDOT[47]. The response to auditory stimulus was enough to decode using a recurrent neural network or temporal patterning, so that eventually the decoder was able to produce synthetic song[47]. While all these studies show interesting insights, the use of penetrating depth probes limits that longevity for these recordings, which invites the use of enhanced surface probes to this research area.

2.1 Experimental Design

We implanted a PEDOT:PSS coated micro-ECoG array over premotor nucleus HVC (used as a proper name) in anesthetized European starlings (Sturnus vulgaris, Figure 11A), and observed strong, reliable spiking responses, presumably tied to single neurons. To validate that we are sensing single unit activity (SUA) from the surface of HVC, we present subjects with potent auditory stimuli, namely the bird's-own-song (BOS) which is known to evoke strong responses in many HVC neurons[45,48], while recording simultaneously from laminar PEAs implanted in HVC below the micro-ECoG array (Figures 11B and 11C). This recording configuration enables conventional depth recording of neural units that are approximately 150μm to 2mm away from the surface recording sites. The simultaneous surface- and the depth-recorded SUA are driven reliably, and in a correlated manner, by the presentation of BOS (Figures 11D and 11E).

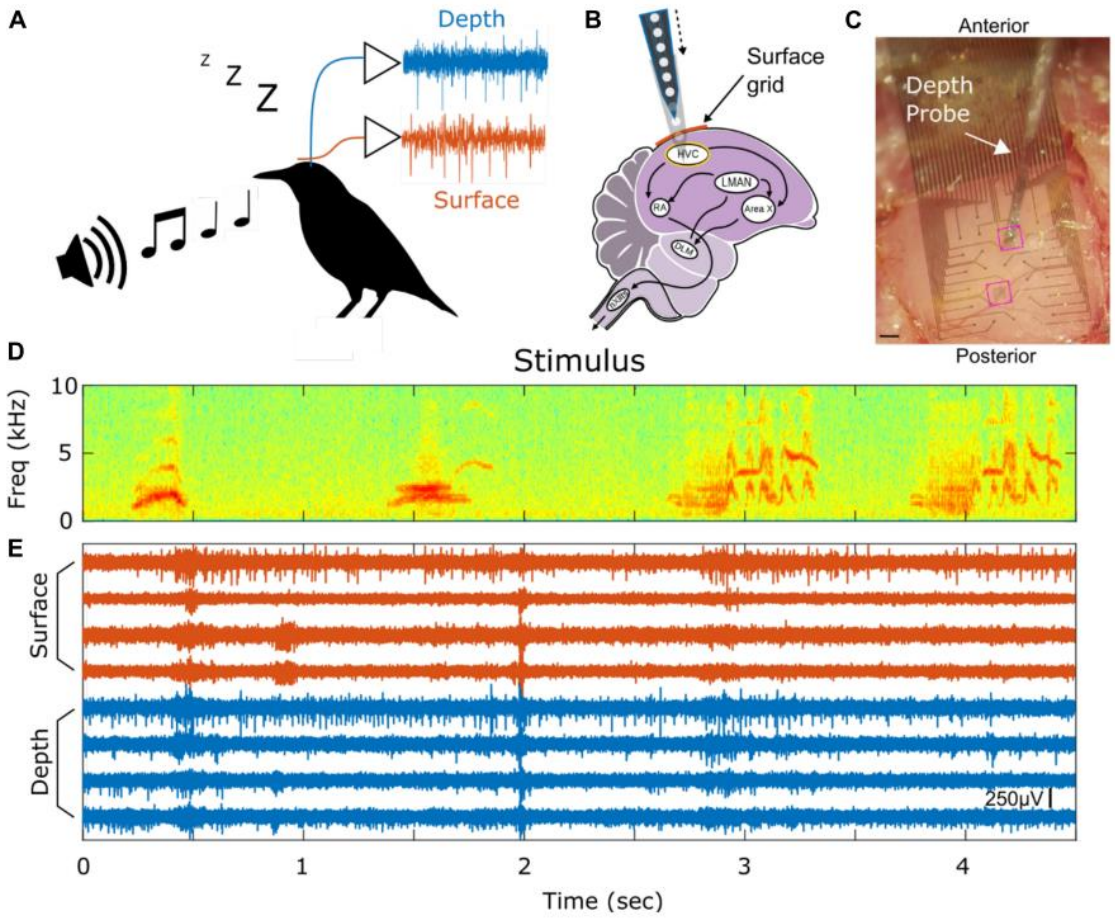


Figure 11 Experimental paradigm and example spiking activity. A Auditory stimuli are presented to anesthetized European Starlings while extracellular voltage waveforms are recorded simultaneously from surface (red) and depth (blue) probes. B The micro-ECoG surface array is placed over HVC and the PEA depth probe is inserted into HVC. HVC is at the top of the vocal production pathways as shown in the schematic of the songbird circuit (HVC, used as proper name; RA, robust nucleus of the archipallium; lMAN, lateral magnocellular nucleus of the anterior nidopallium; Area X, used as proper name; DLM, dorsolateral medial thalamus; nXIIts, tracheosyringeal division of 12th cranial nerve). C Picture of surface grid placed on top of HVC and a depth probe penetrating into the brain through the surface grid. Highlighted in pink rectangles are the two holes where the depth probe can be inserted. Scale bar is 200 μm. D Stimulus spectrogram showing a short portion of a bird's-own-song. E Eight high-pass filtered time series from 4 surface (red) and 4 depth (blue) electrodes showing simultaneously recorded spiking activity. The amplitude scale bar is 250 μV and is located in the bottom right of the figure. Zero is the onset of the auditory stimulus.

2.2 Combined surface and depth probe recording

The micro-ECoG electrode array was manufactured in the nano3 facility at UC San Diego using microfabrication techniques similar to those described in Ganji et al.[49] and summarized in Section 1.2. The array consisted of a 2.9μm thin parylene C substrate, gold interconnects and electrodes coated with PEDOT:PSS, resulting in a total thickness of ~4.2-5μm. The electrode

contacts had a diameter of 20μm and were arranged in a grid consisting of 32 electrodes with a 200μm pitch as shown in Figure 11C and Figure 5. Functional electrodes usually have an impedance around 75kΩ at 1 kHz as measured in a saline bath. Electrodes with impedances greater than 500kΩ are deemed not functional. The surface probe has two square holes to allow for a penetrating depth probe to be inserted in between surface electrodes (Figure 11C).

The depth probe is a commercially available silicon shank manufactured by NeuroNexus (Ann Arbor, MI, United States). One of three versions were used throughout the experiments: 16 site probe with 50μm spacing (A1 × 16-5 mm-50-177-A16) (birds b114, b1061), 32 site probe with three columns of electrodes staggered with an electrode spacing of 25 μm (A1 × 32-Poly3-5mm-25s-177-A32) (bird b1047), and 32 site probe with a linear array of electrodes spaced 20 μm (A1 × 32-Edge-5mm-20_177-A32) (birds b1107, 1067, 1159). The contact area of the 16 and 32 site probes is 177μm^2. Functional electrode impedance was typically 1–2 MΩ as measured in a saline bath.

2.3 Subject Selection and Stimuli Generation

Surgical and behavioral procedures were reviewed and approved by the UCSD Institutional Animal Care and Use Committee (IACUC). Acute experiments were performed on anesthetized European starlings, which typically weigh 55–102 g and are 21.6 cm long. In order to induce singing, testosterone was implanted subcutaneously. A 1–3 mm pellet was prepared by filling a segment of silicone tube (Silastic tubing 508-009) with Testosterone propionate solid (Sigma Aldrich T1875-5G) and sealing it at the ends with thick superglue. The animal was anesthetized using Isoflurane, and the pellet was implanted under the skin, through a small aperture achieved with the aid of scissors and a blunt instrument. The aperture was then closed by suture.

Animals were individually housed in a sound-isolation chamber in which audio was continuously recorded via a microphone (Earthworks M30) connected to a preamplifier (ART Tube MP), sampled at 48kHZ and digitized by the soundcard of a PC using custom software built around the ALSA libraries. Presence of song bouts was automatically monitored nightly from the day's recordings using custom software written in Python. Birds that would start singing tens to hundreds of bouts a day within the 10 days following implantation were selected for the study.

For each bird selected, a few bouts of birds own song (BOS) were selected, of about 40–60 s each. Stimuli presented included the following: (1) BOS; (2) BOS played in reverse (REV), in which the temporal structure of individual syllables and the global syllable order were reversed but overall spectrum was the same as the BOS; (3) song from a conspecific adult (CON). Several (30–60) presentations of each stimulus of choice were presented at intervals picked from a pseudo-random uniform distribution between 7 and 15s, with pseudo-random order within the session.

2.4 Acute recordings in anesthetized songbirds

Preparatory surgeries were conducted either the day before or the day of electrophysiological recording. Animals were anesthetized with isoflurane (Baxter Healthcare). The birds were head-fixed in a stereotaxic device, and the scalp was dissected along the midline. A custom-built, metallic fixation pin was then attached to the caudal part of the bird's skull with dental cement.

On the days of recordings, an animal was anesthetized with 20% urethane (60–100µl total; Sigma, St. Louis, MO, United States) administered into the pectoral muscle in 20-30µl aliquots at 30min intervals. The bird was placed in a sound-attenuating chamber, and its head was immobilized via the head-fixation pin.

A craniotomy and duratomy was performed over HVC following stereotaxic coordinates. The window was centered at 2.5 mm lateral and was large enough to fit the surface micro-ECoG array. The hippocampus on top of HVC was removed by suction. To ensure intimate contact between the surface array and tissue, cerebral spinal fluid (CSF) was removed from the surface of the brain by suction. The surface array was then placed on top of the brain using a micromanipulator (Narishige MO-10), and the depth probe was slowly lowered into the brain through one of the two via holes. Both hemispheres of the brain were used; whenever the brain tissue was visibly damaged by the procedure, the site was not further used for the experiment.

Electrophysiological recordings from both the surface array and depth probe were performed simultaneously with the same data acquisition system, Intan RHD2000 from Intan Technologies (Los Angeles, CA, United States). The Intan RHD2000 USB Controller was connected to a RHD2116 or RHD2132 headstage that was connected to the depth probe; a separate RHD2164 headstage was connected to a surface probe. The following adapter boards were used to connect the probe to the Intan headstage: a custom Flex Adapter[50] for the surface probe and a Plexon (Dallas, TX, United States) N2T A32-HST/32V adapter for the depth probe. Recordings were sampled at either 20 kHz or 30 kHz and data was acquired using either the Open Ephys GUI[51] or RHD2000 software provided by Intan. Default Intan filter settings were used with cutoffs set at 0.01 Hz and 7.5 kHz for data acquisition.

Stimuli were played using software written in Python, running on a single board computer (SBC) (Beaglebone Black). Synchronization with the recording system and later identification of the metadata of the stimuli was achieved by digital trigger pins and/or messages passed using the ZMQ library between the SBC and the Open Ephys recording software. To enable high precision of stimulus onset detection in the recordings, the stimuli were stereo, with one channel containing

a 1–5 kHz waveform that was recorded by the Intan system at the same sampling rate as the neural data. (The software is available on https://github.com/zekearneodo/ephysflow/tree/master/rig_tools).

2.5 Data processing of electrophysiology

2.5.1 Spike Sorting and Unit Characterization

All recordings were converted to KWD format, an HDF5 based data model for neural data. Data recorded in the Intan recording software RHD format was converted to KWD using custom software written in Python (Software available on https://github.com/zekearneodo/intan2kwik). OpenEphys software directly supplies KWD support. For visualizing high frequency activity, the raw recordings were high pass filtered forward and backward using a 3rd order Butterworth filter with a cutoff frequency of 300 Hz, to create a sharp cutoff without phase distortion, and stored as a separate KWD file. Spike sorting was performed using KiloSort[52]. The post hoc merge algorithm included in the KiloSort software was used after the main KiloSort algorithm assigned spikes to clusters. The clusters were manually verified by inspecting spike snippets, correlograms and principal components space using Phy[53] and custom Matlab scripts. Spike clusters were labeled either single unit (SUA), multi-unit (MUA), noise, or artifact – noise and artifact clusters were thrown out for all analyses. Clusters were deemed to be SUA if a sub-sampling of spike waveforms exhibited features that are stereotypical of action potential waveforms and if all the spikes in that cluster did not have a substantial number of refractory period violations (e.g., little to no spikes 0 to 2 ms after spiking). Clusters were deemed to be MUA if the spike waveform resembled that of an action potential waveform but had a substantial number of refractory period violations.

Aggregate spike waveform and timing statistics were computed over all single units (Table 1).

Table 1 Single unit characterization and statistics

	Surface (n = 23)	Depth (n = 46)	P-Value	Test
Duration	0.167 ms	0.5 ms	5.0e-6	Rank sum
Spike Rate	1.95 Hz	1.52 Hz	0.41	Rank sum
Amplitude	53.4 μV	107.3 μV	4.3e-5	Rank sum
Trough/Peak	−0.65	−0.32	7.0e-8	Rank sum
Symmetry	−0.73	−0.13	1.9e-4	Rank sum
Bursts or Not	14/23 = 61%	34/46 = 74%	0.27	Chi-square

The definition of each statistic is described here: "Duration" is the peak-to-trough interval; "Spike Rate" is the number of spikes that occurred divided by the number of seconds; "Amplitude" is the maximum minus the minimum point in the average waveform; "Trough/Peak" is the ratio of the trough and peak values; "Symmetry" is characterizes similarity in waveform shape about the center of the waveform; "Bursts or Not" characterizes if the unit tends to fire within blocks of time and is determined by the void parameter as described in the section "Materials and Methods" of a previous study focused on characterizing inter-spike-intervals and bursts in neuronal activity[54]. Briefly, the void parameter is a statistic based on the distribution of the logarithm inter-spike interval (ISI), which captures short and long scale spike timing. Precisely, the definition of the void parameter is 1−g(minimum)/sqrt(g(peak1)g∗(peak2)), where g(.) is distribution of the log ISI.

2.5.2 Cross Correlation Analysis

Cross correlograms between depth and surface spikes were computed for depth and surface spikes. Cross correlograms are computed by counting the number of times neuron Y (surface unit) fired after or before neuron X (depth unit) within 5ms bins for a range of lags from −100 to 100ms. Cross correlograms are calculated either for baseline periods only (no auditory stimulus) or for both baseline and auditory stimulus periods.

Spike activity similarity between SUAs was characterized by using SPIKE-distance[55]. SPIKE-distance is a parameter-free method that uses the relative timing between spikes from two spike trains to determine their similarity. This distance metric ranges from 0 to 1. Zero indicates identical or synchronous spike trains, while larger distances indicate dissimilar or increasingly dyssynchronous spike trains. This measure uses both long and short duration relationships between compared spike trains and thus it is applied to contiguous periods of time that includes both baseline and auditory stimulus periods.

2.5.3 Analysis of Stimulus Evoked Response

For stimulus-based analysis, the spike counts were calculated within 5ms bins. A smoothed estimate of the average spike count was computed by taking the average across all trials and then smoothing with a 5th order moving average filter. The amplitude envelope of the auditory stimulus was estimated by using the Hilbert transform, low pass filtering and then downsampling to 200Hz to match the sample rate of 5ms binned spiking activity.

The delay between the auditory stimulus and neural response was estimated by using the cross correlation. That is, the cross correlation between the average smoothed spike count and the amplitude envelope of the auditory stimulus was computed for lags less than 200ms – lags greater than 200ms are assumed to be less physiologically relevant. The peak (in absolute value) lag was determined to be the delay, and the auditory stimulus was shifted forward by this amount so that the neural response and auditory stimulus are coherent.

We decided to focus our analyses on the initial response to the stimulus, as it yielded the largest and most robust neural response. The onset of the first sound was found by manually inspecting the spectrograms of the stimuli. 200ms prior to the onset and 300ms after the onset was taken to be the window of interest over which the subsequent metrics were computed.

The Pearson correlation is computed between the average spike count and envelope of the auditory stimulus. Since there are at most 2 auditory stimuli played to the subject per run, the one that yielded the higher correlation was considered. Correlations that had a $p > 0.01$ (Bonferroni corrected) were deemed spurious and not included in the presented analyses. Similarly, only the effect size and the lag of neural responses that were significantly correlated with the auditory stimulus are considered.

In order to quantify the magnitude of the response, a metric we call the effect size was computed. The definition of effect size is: $(\mu peak - \mu base)/\sigma base$, where $\mu peak$ is the average spike count in 5ms bins in a window of ± 50ms about the peak response. $\mu base$ is the average spike count in 5ms bins in a baseline window lasting 1s prior to the stimulus presentation. Finally, $\sigma base$ is the standard deviation of the spike counts in the baseline window. Unless specified otherwise, all analyses were performed using custom Matlab software (Natick, MA, United States).

2.6 Comparison between surface and depth electrophysiology

We record neural activity from the surface probe in all six subjects studied. Specifically, in five out of the six subjects, single unit activity (SUA) is detected, whereas multi-unit activity (MUA) is detected in all subjects. To validate putative surface-recorded SUA, waveform shape and spiking statistics are evaluated, demonstrating characteristics consistent with SUA. Surface-recorded SUAs are shown to be correlated with depth-recorded SUAs; Surface-recorded SUAs are also consistently modulated by the presence of auditory stimulus in a manner that is similar to that of depth-recorded SUAs.

2.6.1 Comparison of Depth- and Surface-Recorded Single Unit Waveform Characteristics

Examples of SUA detected on depth and surface probes are shown in Figures 12A and 12B along with their respective inter-spike interval (ISI). Note that the ISI histograms are consistent with the presence of a refractory period, as we would expect for a single neuron isolation. The unit yield is defined to be the number of channels where there is SUA (or MUA) divided by the total number of functional electrodes (Figures 12C and 12D); the average SUA yields for surface and depth units are 13.7 and 28.7%, respectively.

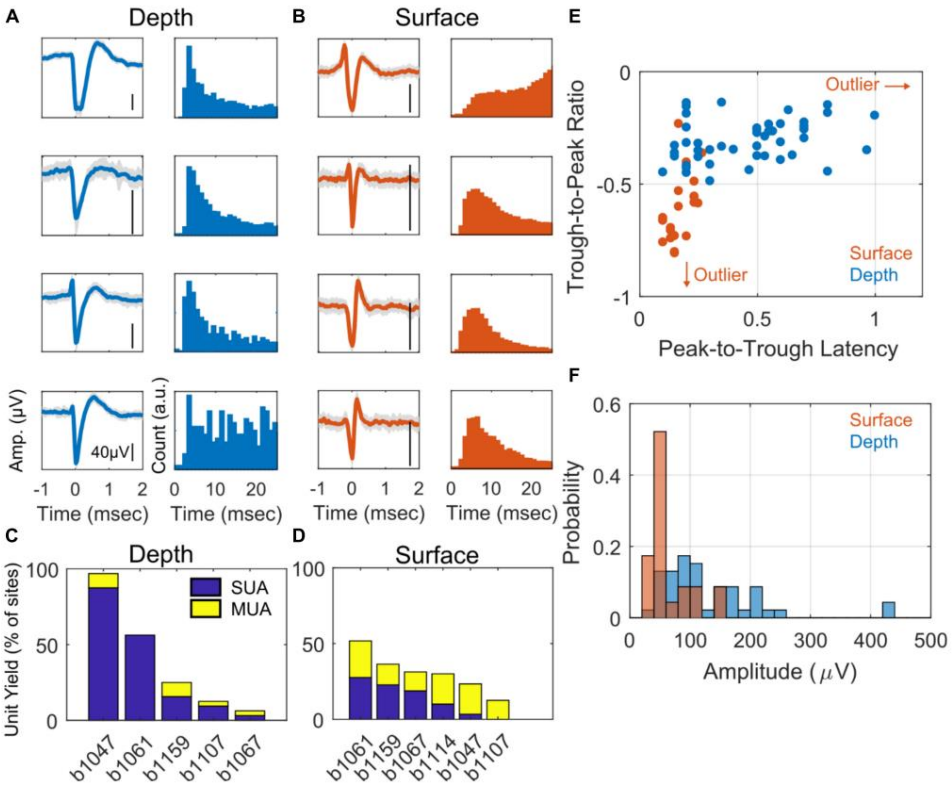


Figure 12 Single unit characteristics. Example of four depth-recorded (A) and four surface-recorded (B) single unit voltage waveforms and the respective inter-spike interval (ISI) histograms. Waveforms are averaged over 50 uniformly sampled spike events. The y-scale bar indicates 40μV in amplitude. C Unit yield for depth (C) and surface (D) arrays as a percentage of total number of contacts. The stacked bar plot shows the percentage of single units (SUA) and multi-units (MUA) for each subject. E Scatter plot showing trough-to-peak ratio vs. peak-to-trough interval for all putative neurons (units) recorded from the surface (red) and depth arrays (blue), respectively. The red arrows indicate an outlying sample from a surface SUA in the direction that the arrows point. F Histogram of surface (red) and depth (blue) single unit amplitudes in μV.

The depth and surface spike waveforms tend to differ with respect to shape-based features, such as duration and relative trough and peak amplitudes. In the analyses, peak is defined as the minimum point in the waveform (initial depolarization) and the trough is the maximum point that occurs after the peak. Furthermore, duration, or peak-to-trough latency, is defined to be the time between the peak and trough. In general, the depth spikes tend to have a longer duration and larger peak relative to trough than do the surface spikes. This is consistent over the entire dataset of depth and surface SUA as shown in Figure 10E. There is a clear cluster of surface SUA in the lower left portion of the graph, whereas the depth SUA occupies the upper portion of the graph. Furthermore, depth units are more likely to have a larger amplitude than surface units (Figure 10F). Additional spike statistics are computed for depth and surface SUA and are summarized in Table 1. Waveform characteristics (duration, amplitude, trough/peak, symmetry) differ significantly ($p < 0.01$) between depth and surface SUA, although the duration of both surface and depth units is consistent with a previously reported duration range for depth SUA of 0.18–0.85ms[45]. Spiking characteristics (spike rate and bursting), in contrast, are not significantly different between depth and surface units in this anesthetized experimental setting.

2.6.2 Correlation Between Putative Surface SUA and Depth SUA

An analysis across baseline and auditory stimulus periods of cross-correlograms calculated between spike rasters of depth- and surface-recorded single unit pairs is summarized in Figure 13. Figure 13A illustrates how pairs are formed between a depth electrode and a surface electrode. Example cross-correlograms between a single surface electrode and two different depth electrodes are shown in Figures 13B and 13C. In Figure 13D, the calculated SPIKE-distance of depth and surface spike raster pairs are plotted versus the physical distance between the electrodes that the corresponding units were recorded on. From this plot, we can see that the closest surface and depth

electrodes from which SUAs were detected are at least 600µm apart. Thus, it is highly unlikely for any pair of surface and depth electrodes to be recording from the same neuron. There is a statistically significant positive correlation between the SPIKE-distance measure[55] and physical distance. SPIKE-distance is 0 for identical spike trains and the measure increases up to a value of 1, which indicates two complete dyssynchronous spike trains. Thus, the positive correlation indicates that as the distance between the electrodes on which depth and surface units increases, their rasters tend to become less synchronous. The histogram of peak lag values appears to be positively skewed, suggesting that depth units may tend to precede surface units; however, the distribution does not significantly deviate from 0ms, indicating no significant average lag between surface and depth units (Figure 13E).

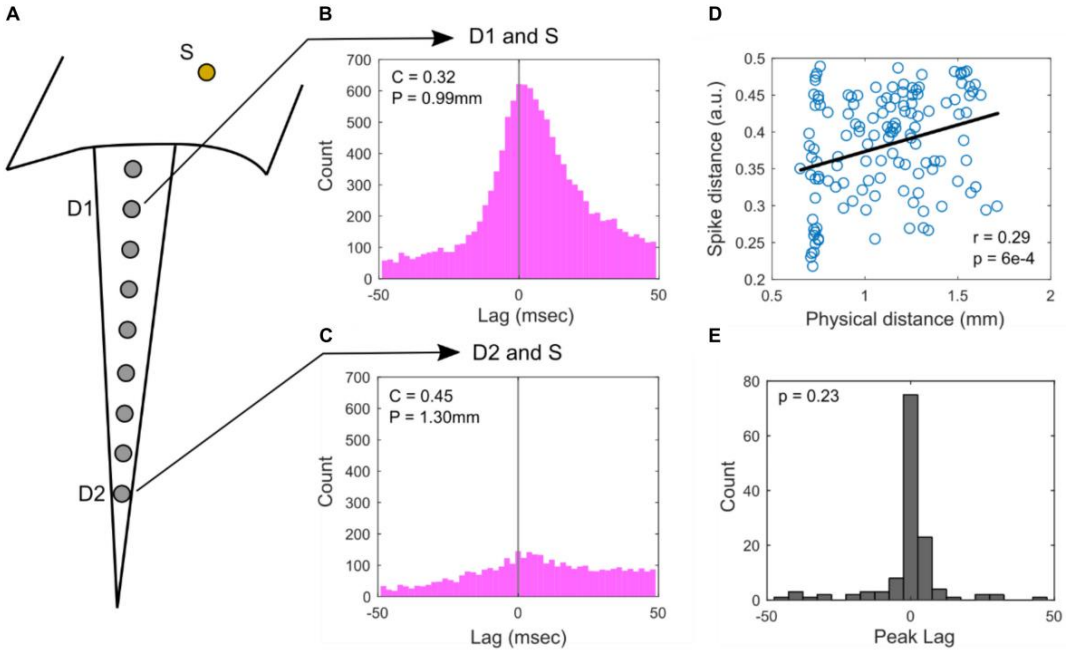


Figure 13 Cross-correlograms. A Illustration of electrode locations: surface (S) and superficial depth electrode (D1) and deep depth electrode (D2). SUAs were detected on these electrodes and their correlograms were computed in B and C. B Cross correlation of S and D1, showing high co-occurrence. Spike distance, C and physical distance, P are relatively low. C Cross correlation of S and D2, showing lower co-occurrence. Spike distance, C and physical distance, P are relatively high. D Population analysis of all surface and depth SUA pairs comparing spike distance vs. physical distance. There is a significant Pearson correlation of r = 0.29 (p = 6e-4, n = 131, Student's t-distribution). E Histogram of the peak lag appears to be positively skewed; however, the distribution does not significantly deviate from 0, suggesting no significant positive or negative lag between surface and depth units (p = 0.23, n = 131, rank-sum test).

2.6.3 Auditory Stimulus Driven Modulation of Putative Surface SUA and Depth SUA

The SUA recorded from depth and surface arrays is modulated by auditory stimuli. An example of this modulation from a depth and a surface single unit can be seen in Figures 14A–D. In Figures 14A–C, the spectrogram of a single auditory stimulus presentation, bird's own song in this example, is plotted alongside the temporally smoothed trial-averaged spike rate for each unit. The spike rate of both the depth- and surface-recorded units appears to be modulated by features of the stimulus, particularly at the beginning of the stimulus. Figures 14C and 14D zooms in to highlight the first 4.5s of the stimulus. Panel C is the spectrogram of the stimulus with the stimulus amplitude envelope plotted on top of the spectrogram. Panel D shows spike raster plots with average spike rate plotted on top. Here, a strong response due to the initial sound and a smaller response at 3s aligned to a more complex vocal element of the birdsong can be observed. When a variant of this complex vocal element reoccurs at around 4s, it elicits a smaller response. Responses of HVC neurons to natural auditory stimuli, and in particular the BOS, are very well-documented in multiple songbird species[45,50,51]. Previous reports in starlings show that individual syllables from BOS and conspecific song evoke auditory responses with varying specificity[45,56]. It is well known, at least in other species, that HVC auditory responses can integrate over long time scales and are sensitive to specific temporal (and harmonic) combinations of song elements[57,58].

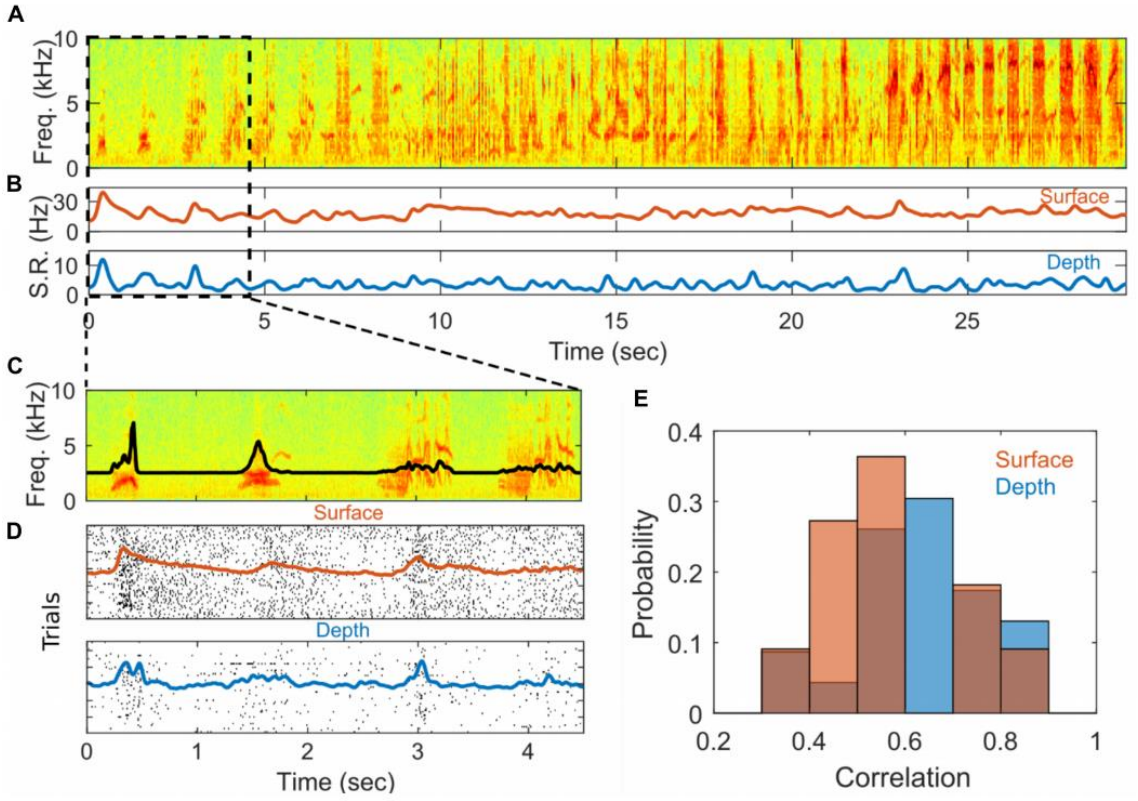


Figure 14 Stimulus driven responses. A Example spectrogram of a stimulus, Bird's-own-song presented during electrophysiological recording. B Averaged smoothed spike rate for single units recorded from the surface (red) and depth (blue) arrays. The average spike rates were smoothed with a 5-point Gaussian window with a standard deviation of 0.4. C Zoom-in of first 4.5s of A. The black line shows the amplitude envelope of the stimulus. D Spike raster plots showing the times of individual spiking events on each of 54 successive stimulus presentations for the surface (red) and depth (blue) SUAs in B. The red and blue lines show the smoothed spike rates averaged across stimulus presentations for the surface and depth units, respectively. The spike rates were smoothed with a 30-point Gaussian window a standard deviation of 0.4. E Distribution of correlation values for depth (blue) and surface (red) for units that are significantly correlated with onset of the auditory stimulus.

As a simple test to determine if the recorded SUA is modulated by the auditory stimuli, we characterize the response at the initial onset of each stimulus following a prolonged inter-stimulus interval (7–12s) during which no stimulus is presented. The initial SUA response is quantified by first computing the Pearson correlation between the average spike count and the amplitude envelope of the stimulus over a 500ms window centered around the stimulus onset (after correcting for a delay in the neural response, see section "Materials and Methods"). Correlations are deemed spurious if they have an associated $p > 0.01$ (Bonferroni corrected). To quantify the magnitude of the response, an effect size metric is computed for SUA with responses that are significantly

correlated with the stimulus. The effect size metric captures the difference in spiking activity between a peak response window and a baseline window and is normalized by variation in the baseline spiking activity. Finally, the lag between auditory stimulus and spiking activity is computed for depth and surface. The histogram for depth and surface correlation is in Figure 14E. The distributions of correlation values for depth and surface units appear to be similar. Hypothesis testing also indicates that the distribution of correlation values is not significantly different from each other within the constraints of these data points (nsur = 11 and ndep = 23). These statistics are summarized in Table 2.

Table 2 Number of single units significantly with auditory onset for each subject

	Depth	Surface
b1061	7	6
b1047	16	0
b1067	0	2
b1114	0	1
b1107	0	0
b1159	0	2

2.7 Discussion

Stimulus modulated SUA recorded from the surface of sensorimotor regions in the songbird brain is presented. Average spike rates from putative surface-recorded neurons show a marked increase during stimulus presentation, particularly at the start of song stimuli. In total, about half of the depth and surface single units are significantly correlated to the amplitude envelope of the initial phase of the stimuli. Stimulus correlation values of surface SUA are comparable to depth SUA and no significant differences in effect size are found.

Raster cross-correlation analyses do not indicate a specific relative timing bias between surface and depth units. However, spike raster similarity analyses indicate that SUA recorded at depth and SUA recorded at surface tend to be more similar if they are recorded at electrodes that

a physically closer together. Since surface unit recording locations in this study are at least 600μm from the closest depth locations, this similarity is very unlikely to be the result of recording the same neural unit from a depth electrode and a surface electrode. Overall, the analyses of spiking characteristics, both stimulus conditioned and not, suggest that the response properties of surface and depth units are similar.

Surface-recorded SUA waveform characteristics appear to be distinct from those of depth-recorded SUAs. In particular, peak-to-trough latency is significantly shorter for surface SUA than depth SUA (Figure 12). Furthermore, the ratio of trough-to-peak amplitudes as well as absolute amplitude appear to be significantly different between surface and depth SUA (Figures 12E, 12F and Table 1). One possibility is that these differences are due to unmatched filtering characteristics between the depth and surface recordings. As the same amplifiers were used to record from surface and depth, if such a difference exists it would likely be driven by the electrical characteristics of the physical electrode-brain interface. Another possibility is that surface and depth recordings are biased to sample different cell types or different locations on a cell (or both). Waveform shapes difference can be explained by both the biased cell type and location hypotheses[59]. HVC contains several types of neurons including multiple classes of projection neurons targeting the robust nucleus of the arcopallium (RA) and basal ganglia nucleus Area X, as well as multiple interneurons, who project locally within HVC[53]. These different neuron types have different morphologies[60], but the heterogeneity in their spatial distribution (if any) remains mostly unresolved. A previous report indicates that a group of cells with a tendency toward longer or bursting responses is centered in the ventral part of HVC[45], and this would be consistent with our measurements of a higher ratio of bursting in the cells recorded with the penetrating probe. More detailed understanding of the biases in our surface electrodes for sensing a particular neuron type

or its projections remains a topic for future work. In mammalian brain, cortical neuronal organization and morphology have been better characterized, and it may be possible to design electrodes that target specific cell classes.

Low surface area and low impedance electrode contacts, along with the conformality of the arrays to the brain surface, are important characteristics for recording putative action potential activity from the brain surface as demonstrated in this study and in previous mammalian studies[1,61]. In a modeling study[62] evaluating critical characteristics for recording action potentials from the cortical surface of the rat, small electrode surface area facilitates retention of action potential amplitude relative to larger electrodes. However, as surface area decreases for an electrode of a given material, the impedance will increase and, consequently, thermal recording noise will also increase. Thus, it is crucial to fabricate small surface area electrode contacts with materials that permit a low impedance electrical interface to the brain surface. We note that our electrodes have over three times the surface area of the electrodes in previous mammalian studies[1,61]. This may have contributed to our lower and variable yield of electrodes with single- and/or multi-unit activity (Figure 12D) relative to previous cortical recordings in rat [55–93% yield as reported in Khodagholy et al.[1]]. However, yield in human recordings (27–37%)[1] is closer to our yield. These yields and their variability could be due to a wide range of factors beyond electrode design, including species differences and specifics of surgical and recording procedures. For example, the rodent recordings were conducted while the animal was awake and behaving; while our starling recordings and their human recordings were conducted under anesthesia, potentially influencing the probability of neural spiking.

Electrode array conformality is also of importance for recording quality. According to the modeling study[62], neuron cell bodies (in the rat preparation) must be within 60μm of a 100μm^2

electrode contact (our electrodes have a 314 μm^2 surface area, which should reduce the distance requirement). Furthermore, if electrodes are further from the cortical surface and have cerebral spinal fluid (CSF) under electrode contacts, this could cause shunting that would obscure action potential recording. The modeling study[62] also suggests that the conformal insulation of the electrode array substrate around the electrode may also be important for resolving action potentials. Surface insulation effectively creates a reflection of charges that does not exist at the natural conductive CSF interface. Thus, insulation can effectively boost the action potential signal relative to thermal noise. A previous rat study[63] suggested that multi-unit activity could be recorded from the brain surface, but did not demonstrate single-unit like activity. In that study an array of 50μm diameter microwires were brought to the cortical surface. Beyond the larger surface area relative to the electrodes in the current study, those microwire electrodes have higher impedance and lack the planar insulation of thin film electrode arrays. These design characteristics of the microwire bundle may have resulted in reduced signal quality, obscuring single unit activity. Electrode characteristics at the micro and nanoscale provide avenues for future enhancements of recording quality. For example, electrodes in planar arrays for in vitro recording preparations can be modified to have a 3D mushroom-like shape, resulting in more intimate contact with cell membranes and higher signal to noise ratio recording[64]. Electrode arrays for in vivo surface recordings could employ similar design strategies to improve the quality and reproducibility of tissue contact.

While the current study is acute, thin film micro-ECoG preparations have been employed for chronic recordings in multi-day awake behaving chronic preparations in small animal models, including mouse[65] and in rat[66]. Chronic studies with the electrode arrays used in the current acute study would require additional device and surgical technique development, as well as longevity

testing. Such development would allow for richer study of the unit activity to assess stability and response characteristics during free behavior and song production.

In summary, we demonstrate the ability of micro-ECoG electrode arrays coated with PEDOT:PSS on a 4–5μm thin Parylene C substrate to sense single units over HVC in anesthetized European Starling. These single units are found in five out of six subjects with an average yield of 13.7%. An increase in spiking activity is observed at the onset of the auditory stimulus for both surface and depth single units. Roughly half of the single units for both surface and depth are significantly correlated with the onset of the auditory stimulus. These results reproduce and extend an important finding, which is that single units can be sensed from the surface of the brain, and their activity can be modulated with sensory relevant stimuli. By providing a first demonstration of stimulus driven response from surface recorded units, the results of this study increase confidence that these units are indeed single neurons and that micro-ECoG is an effective tool for observing neural activity with high-fidelity. Furthermore, by demonstrating these capabilities in songbird, we provide a new paradigm for studying the neural basis of speech and language and a development platform for cortically driven speech prostheses.

Chapter 2, in full, is a reprint of the material as it appears in Frontiers in Neuroscience, 2020. Hermiz, John; Hossain, Lorraine; Arneodo, Ezequiel; Ganji, Mehran; Rogers, Nicholas; Vahidi, Nasim; Halgren, Eric; Gentner, Timothy Q.; Dayeh, Shadi A.; Gilja, Vikash, Frontiers, 2020. The dissertation author was the primary author of this paper with two other first co-authors. The statistical analysis reported in the paper was conducted by fellow first co-author Dr. John Hermiz.

Chapter 3 Diameter and material dependence for recording single unit activity

3.1 Experimental Design

The ability to detect single units from the surface of the brain has been a relatively new milestone in neurophysiology. Typically impedance scales inversely with diameter of the electrode, which increases the listening sphere of individual electrodes and consequently hinders the isolation of single unit activity. With the enhanced electrochemical properties of electrode contact surfaces like PEDOT:PSS and platinum nanorods (PtNRs), the electrode diameter – and listening sphere – can be decreased without losing the signal to noise quality. This raises the question what is the cutoff diameter with which we see single units from the surface. To answer this question, PtNR surface electrodes were fabricated with varying diameters ranging from 20µm to 2000µm. Figure 15A shows the dark PtNR electrode surface for all the diameter sizes, and Figure 15B shows the device implanted over HVC in a European starling. The impedances scaled with the diameter as reported in our lab for both PtNR and PEDOT:PSS electrodes[31].

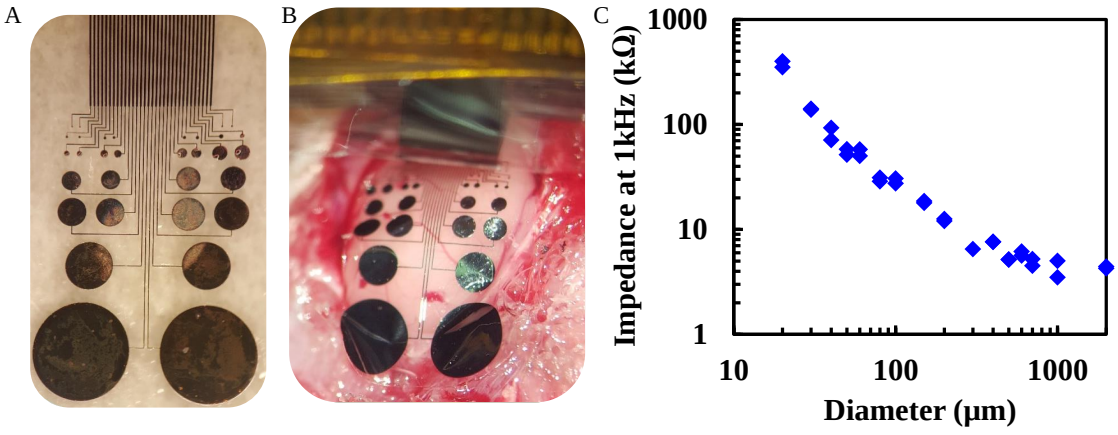


Figure 15 Device geometry for variable diameter experiment. A Device with 32 PtNR electrodes of varying diameters. B Placement of variable diameter device over HVC in European starling. C Impedance measured at 1kHz vs. electrode diameter.

The large spatial coverage of the device required a larger craniotomy, which increases the chance of cooling on the brain and potential swelling of the brain tissue, which can reduce the time a recording can last. For this reason the larger electrodes with 2000µm diameters did not fit within the open region, yet detection of single units at such large diameter is not likely.

3.2 Analysis of diameter and material dependent spike recording

Similar to Section 2.5.1, Kilosort was initially used to spikesort the resulting data. Classifications of units detected by the Kilosort software were segregated into four types: single unit, multi-unit, noise, and artifact, as seen in the figure below. Single unit clusters exhibit a refractory period, seen as the initial dip at about 1ms in the inter-spike-interval histogram for single units in Figure 16.

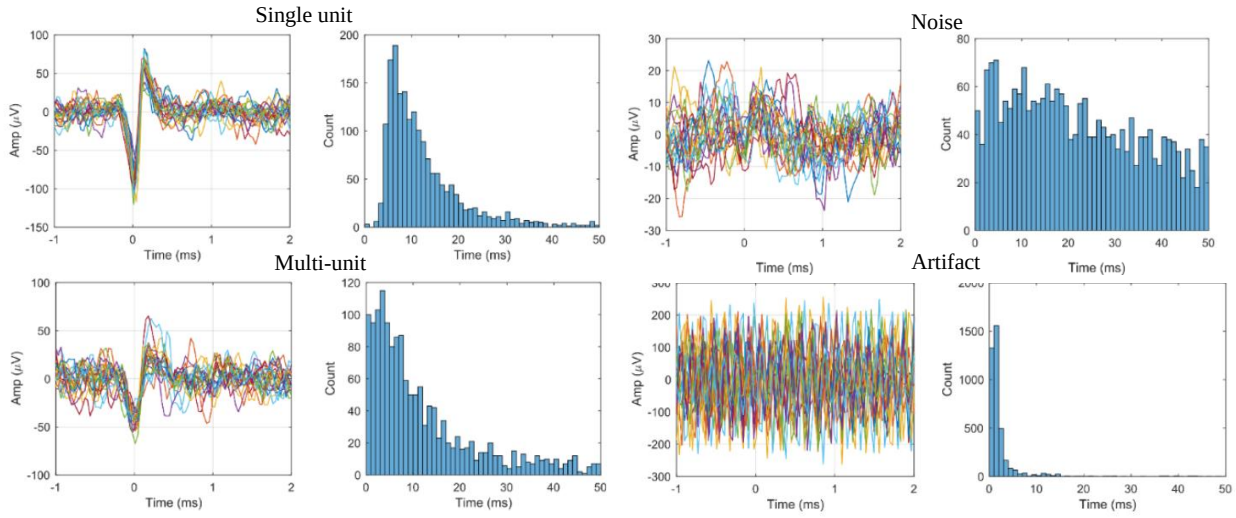


Figure 16 Classification of unit labeling: single unit, multi-unit, noise, and artifact. The waveform plots are 50 snippets from that specific cluster sampled uniformly over the recordings. The blue histograms show the inter-spike-interval histograms showing the number of spikes that occur within a certain period ranging from 0 to 50ms after all spikes occurred.

Refractory periods help validate the presence of single units by representing the time a neuron recovers before firing a subsequent spike[67,68]. Clusters with a refractory period violation while still maintaining a defined trough and peak in the waveform are classified as multi-unit.

Clusters in which the waveform is obscured within the baseline are classified as noise, and clusters exhibiting oscillatory waveforms demonstrate the presence of an artifact.

One challenge in analyzing the recordings with Kilosort software is the assumed crosstalk between electrodes during recording, as Kilosort was originally created for tetrode devices. To address this, Spike2 software (CED) was utilized to process the same dataset to allow spike sorting of individual electrodes regardless of geometrical location of the electrode on the array. When processing the data from the same electrode in the same recording, both sorting techniques were able to detect single units, with similar waveforms and inter-spike-interval properties.

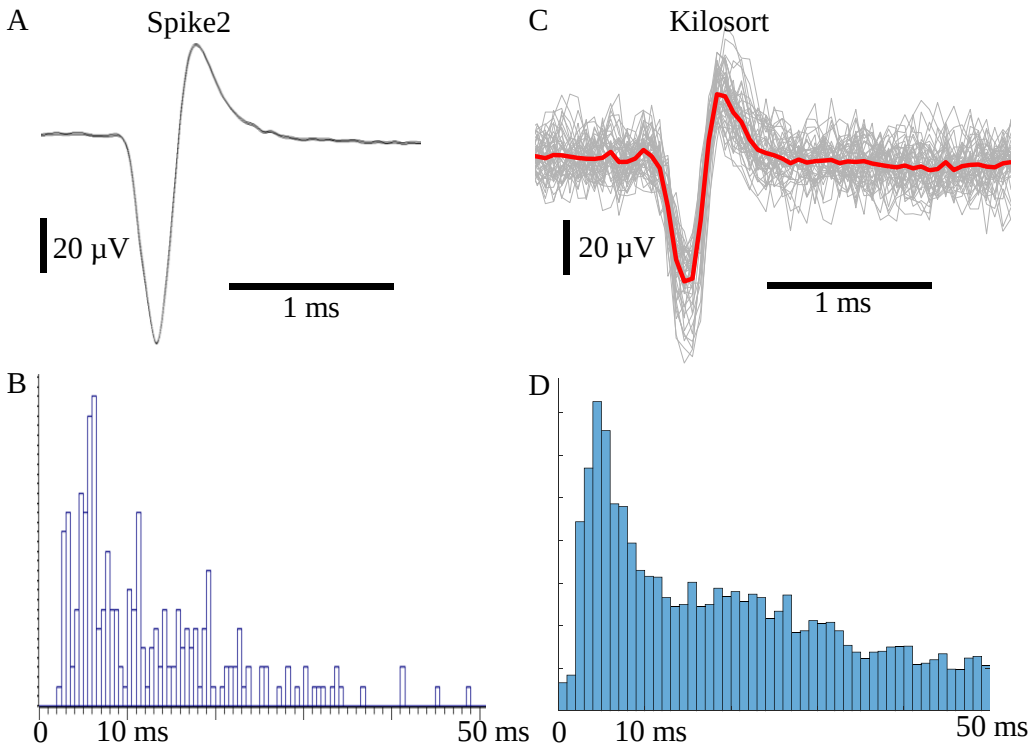


Figure 17 Comparison on the same dataset for two different spike sorting software: Spike2 (A-B) and Kilosort (C-D). A/C Average waveform of a single unit detected using with the corresponding inter-spike-interval histogram B/D.

Spike2 allowed easier manual exclusion of falsely classified spikes that were grouped within a unit. This procedure led to slightly larger waveform average amplitudes and less refractory

period violations. When plotting the trough to peak amplitudes of the waveform averages and plotting across the varying diameters, however, both spike sorting software showed similar decreasing trends.

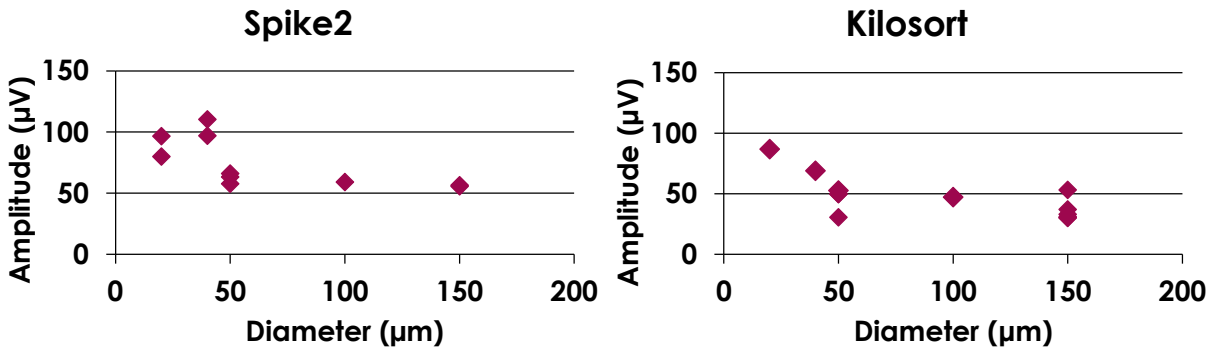


Figure 18 Peak to trough amplitude of the average waveform for single units vs. electrode diameter comparison between two spike-sorting software: Spike2 and Kilosort.

Due to the added control that Spike2 allows for post-processing of the detected units without the assumed influence of neighboring electrodes, Spike2 was used for the subsequent analyses. The next device geometry was designed with the goal of incorporating many more diameter sizes between 10µm and 250µm to better determine the diameter cutoff for single unit detection. Additionally, the electrodes with different diameters were arranged in three clusters that are slightly larger than the HVC nucleus in order to account for placement errors and record from an active region with all diameter variants.

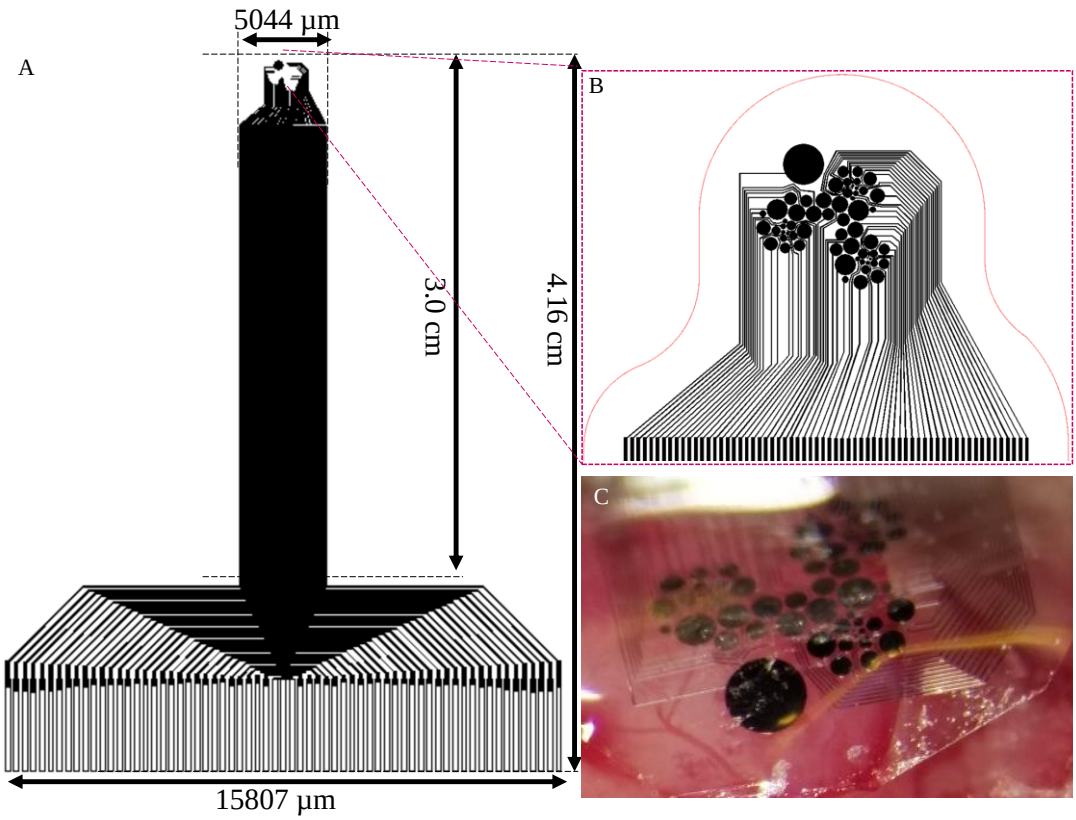


Figure 19 Device geometry for 64 channel variable diameter array. A Mask design with B inset of the electrode active area. C Implantation in vivo of the device.

Once more, the spatial coverage of the device exceeded the craniotomy, one electrode cluster was centered over the HVC region. Three sets of devices were fabricated with different electrode contact materials: PEDOT:PSS, PtNR, and planar Au as the conventional metal. The impedances of the electrodes scaled with the diameter is plotted with Figure 20 and exhibit a behavior that is expected from previous literature and our previous work as discussed below[31].

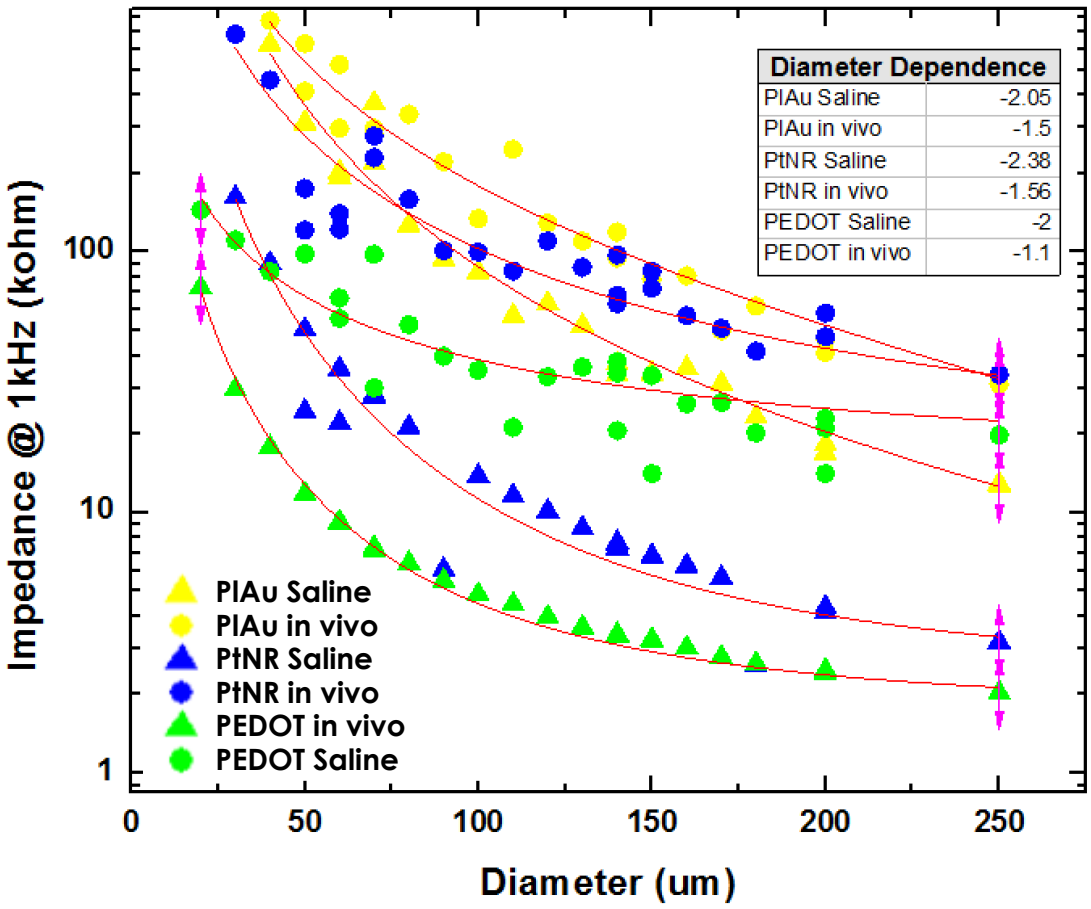


Figure 20 Impedance measured in both saline solution and in vivo at 1kHz for large scale variable diameter device shows inverse relationship between impedance and electrode diameter.

As expected, the planar Au electrodes exhibited much higher impedance values compared to the PEDOT:PSS and PtNR electrodes. Upon implantation *in vivo*, the impedances increased for all three devices regardless of electrode material, with the diameter dependence trend became less prominent compared to the saline measurements. After spikesorting each dataset in Spike2, the average waveforms of the single units were generated for each electrode diameter size and each material, as seen in the Figure 21. The PtNR electrodes exhibited noticeably higher amplitude than PEDOT:PSS or planar Au as shown in Fig. 21.

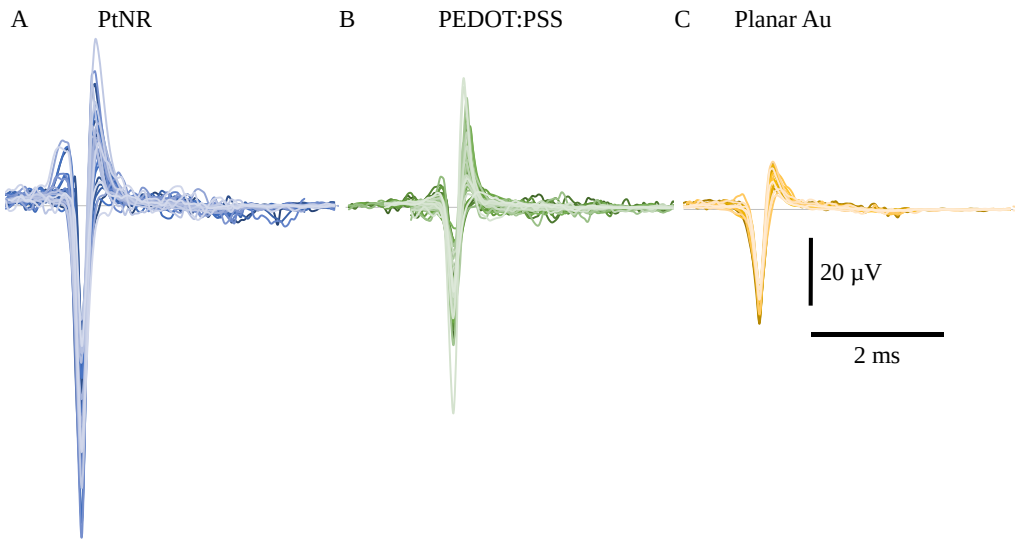


Figure 21 Average waveform of single units for three electrode materials: PtNR, PEDOT:PSS, and Planar Au. The colors range up in electrode diameter size from 20µm to 250µm with fainter colors representing larger diameters.

The trend based on diameter is hard to determine by examining the waveforms on their own as seen in Fig. 21. Therefore, the trough to peak amplitudes for each waveform was calculated. Unlike the prior preliminary experiments, the amplitude didn't show a strong diameter dependence. The planar Au electrodes showed a very slight decrease in amplitude with increasing diameter, but overall, the diameter dependence was inconclusive.

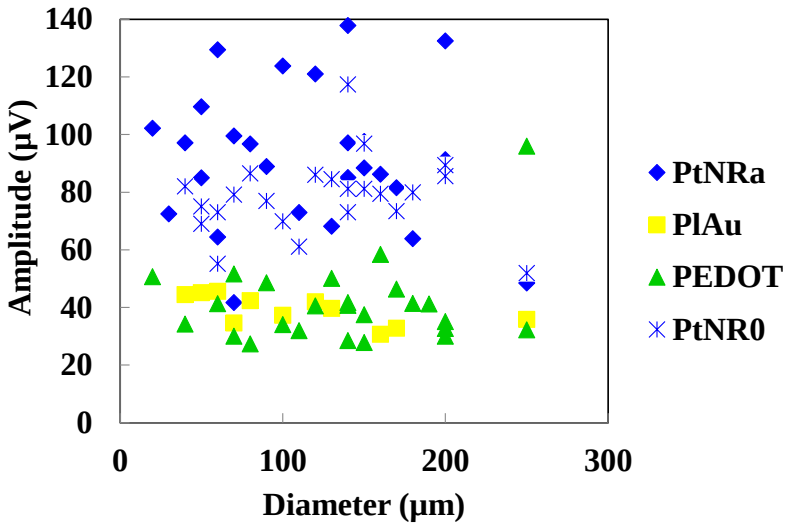


Figure 22 Amplitude vs. Diameter for different electrode interfaces

Again, the PtNR electrode exhibited higher amplitude than PEDOT:PSS or planar Au; however, the standard deviation of non-stimulated baseline recording, which we consider to be the electrode noise, showed that the average noise detected on the PtNR electrodes was higher than the PEDOT:PSS and planar Au electrodes. As observed in Figure 23, the PtNR electrodes exhibited higher baseline noise. When dividing the amplitude by the baseline standard deviation to calculate the overall signal to noise ratio (SNR), no apparent differences were obvious between materials or diameter.

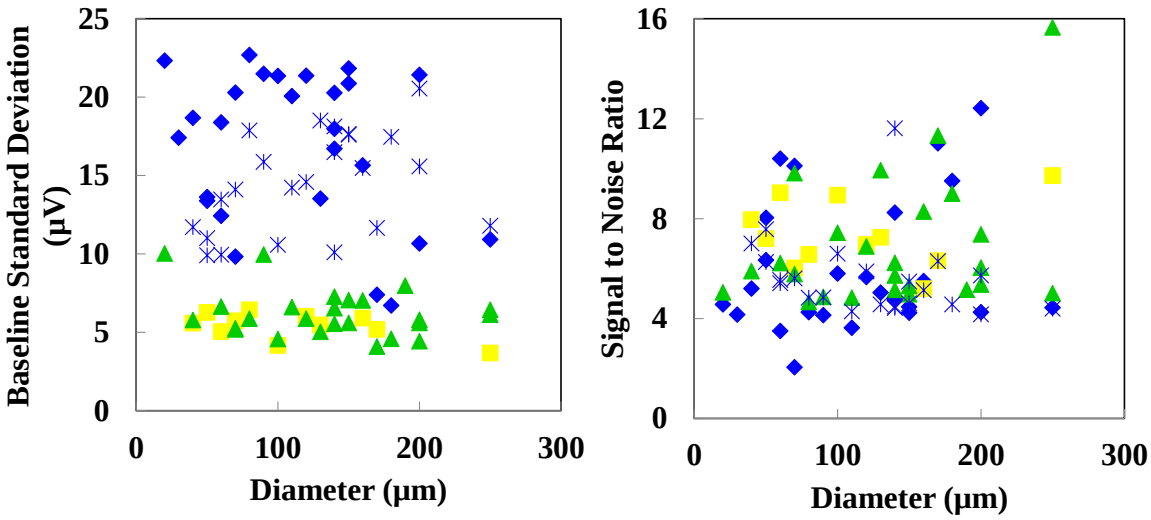


Figure 23 Baseline standard deviation vs. diameter and signal to noise ratio vs. diameter for different electrode interfaces.

It is uncertain what exactly caused the drastic change in the amplitude and baseline noise for the PtNR electrode. The different devices were implanted and recorded individually, with the PtNR device implanted first, then removed to be replaced by the PEDOT:PSS device, which was then removed and replaced by the planar Au device. This introduces the possibility that the quality of the signal can be affected over time due to tissue damage, as well as non-uniform placement of the devices even though each placement centered one group of contacts to the HVC area.

Another analysis was conducted regarding the full width of the average waveforms for units at half of the amplitude of the initial trough. The full width half max (FWHM) measurement was done by interpolating the average waveform, dividing the minimum (trough) by 2, finding the positions of the waveform that cross the half max value, and calculating the distance between the two positions. This is summarized in Figure 24.

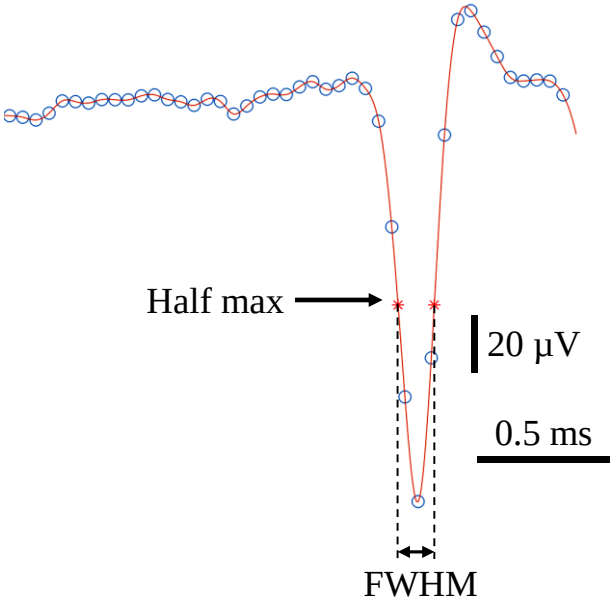


Figure 24 Example full width half max calculation for a single unit. The red line shows interpolation from the waveform average. The measured FWHM for this particular unit was 0.13757ms.

Plotting the FWHM values as a function of the diameter of the electrode that detected that unit, we see the following trend: As seen in Figure 25, the PtNR and PEDOT:PSS electrodes exhibited slightly increasing FWHM with increasing diameter. However, the planar Au electrodes showed a sparser layout of the FWHM with increasing diameter, suggesting no diameter dependence to the FWHM for the planar Au.

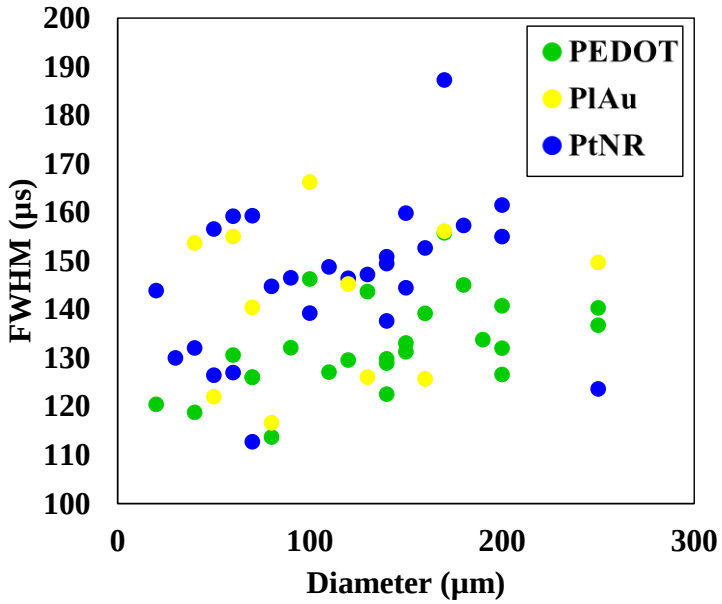


Figure 25 Full width half max vs. diameter for three electrode materials.

Some studies have reported the ability to discern different types of neurons based on clustering of the FWHM and spontaneous firing rate of the single unit[69,70]. Plotting the FWHM vs. the spike rate, the spikes are clustered in Figure 26.

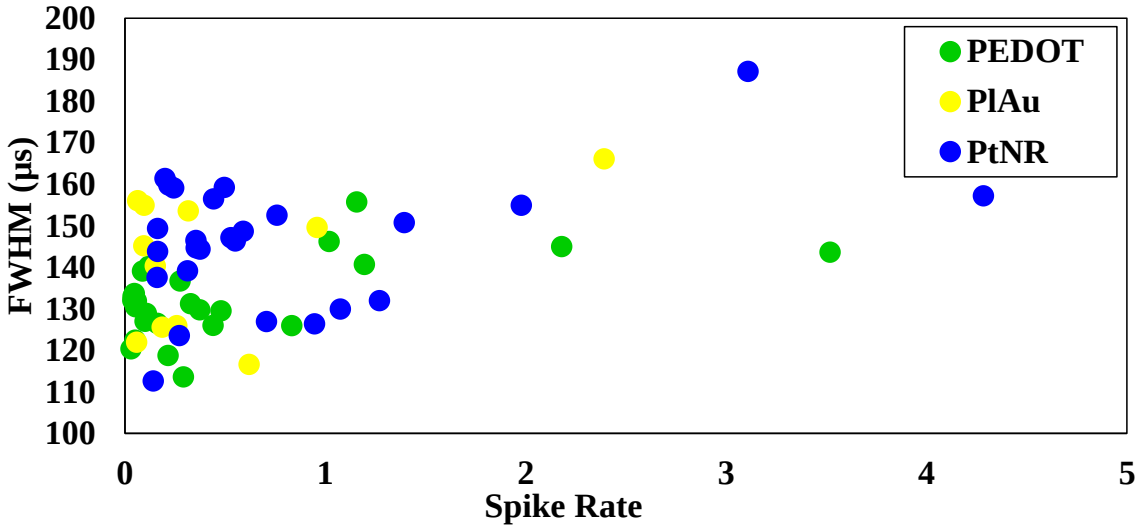


Figure 26 Full width half max vs. spike rate for three electrode materials.

The PtNR electrodes appear to detect units that cluster with a larger FWHM than the PEDOT:PSS electrodes, while the planar Au electrodes fail to show strong clustering for the units

detected. This opens up the possibility that the PtNR electrodes recorded units from a different set of neurons than the PEDOT:PSS electrodes. As for the difference in the amplitude and baseline noise observed in Figure 22 and Figure 23, another possible explanation for the substantial change between electrode materials could be from detecting different types of neurons. Jeanne et al. described that correlations of the signal and noise is cell-type specific[71]. In their paper, though, the spike width was defined as the time between the minimum of the trough and the maximum of the peak, rather than the FWHM[71]. The Trough-to-Peak width is plotted in Fig. 27. Both the PEDOT:PSS and planar Au electrodes showed bimodal clustering around a boundary between 210µs – 250µs which is lower than the reported value of 430µs as seen Fig. 27. However, Jeanne et al. claimed that their filtering technique increased the spike widths above previously reported boundaries[71]. Another work by Mitchell et al. reported a boundary between narrow action potentials and broad action potentials of 200µs[72], which is closer to the boundary observed by the PEDOT:PSS electrodes and the planar Au electrodes.

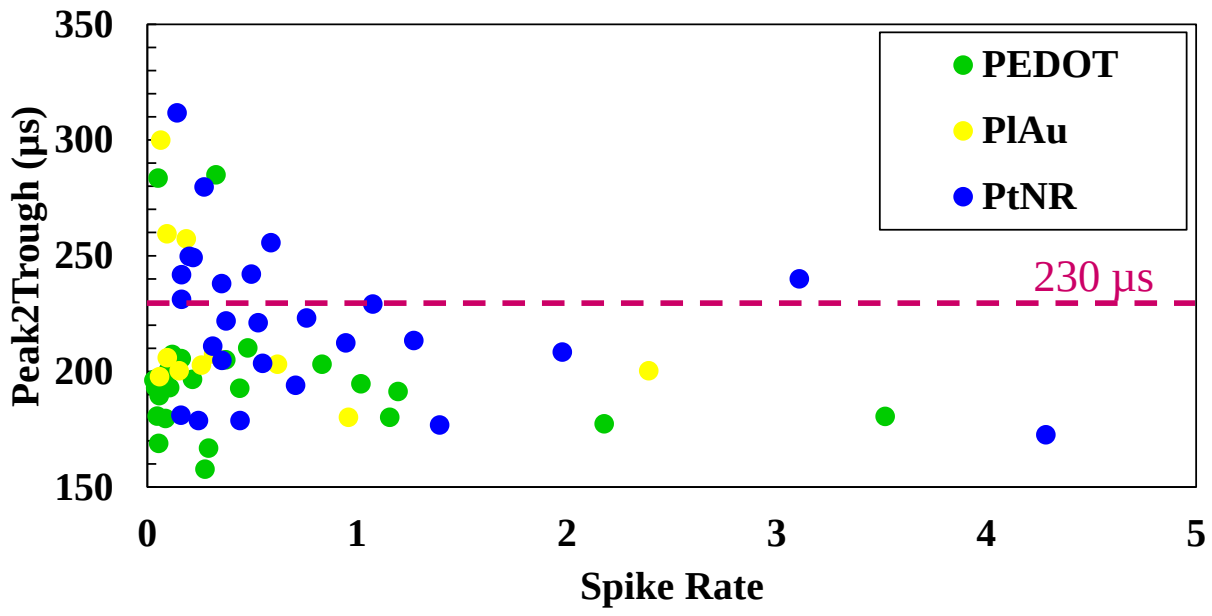


Figure 27 Peak-to-trough vs. spike rate for units detected from three different materials.

Whether this clustering of spike widths suggests the presence of different neuron types between electrode materials or the electrode materials detect differences in the waveform shape due to differences in their electrochemical properties is still uncertain. To rule out the possibility of tissue damage affecting the quality of the signal and different placements from subsequent recordings resulting in recording from different neuronal populations, a new variable diameter electrode design was developed that has different materials on the same device for simultaneous recording.

3.3 Combined form factor for diameter and material dependence analysis

The electrode materials utilized for these devices were PEDOT:PSS, PtNR, and planar Pt as the conventional metal, and the same diameters were grouped in triodes to ensure electrodes detect response from the same neuronal populations. Fabrication of these multi-material electrodes was conducted by the Integrated Electronics and Biointerfaces lab member Dr. Hongseok Oh. Like the previous device form factor, impedance scaled with diameter for all three materials with the conventional Pt electrode reporting much higher values. Upon implantation onto the cortical surface, the impedances increase and the diameter dependence shifts to a less severe power than as measured in saline solution.

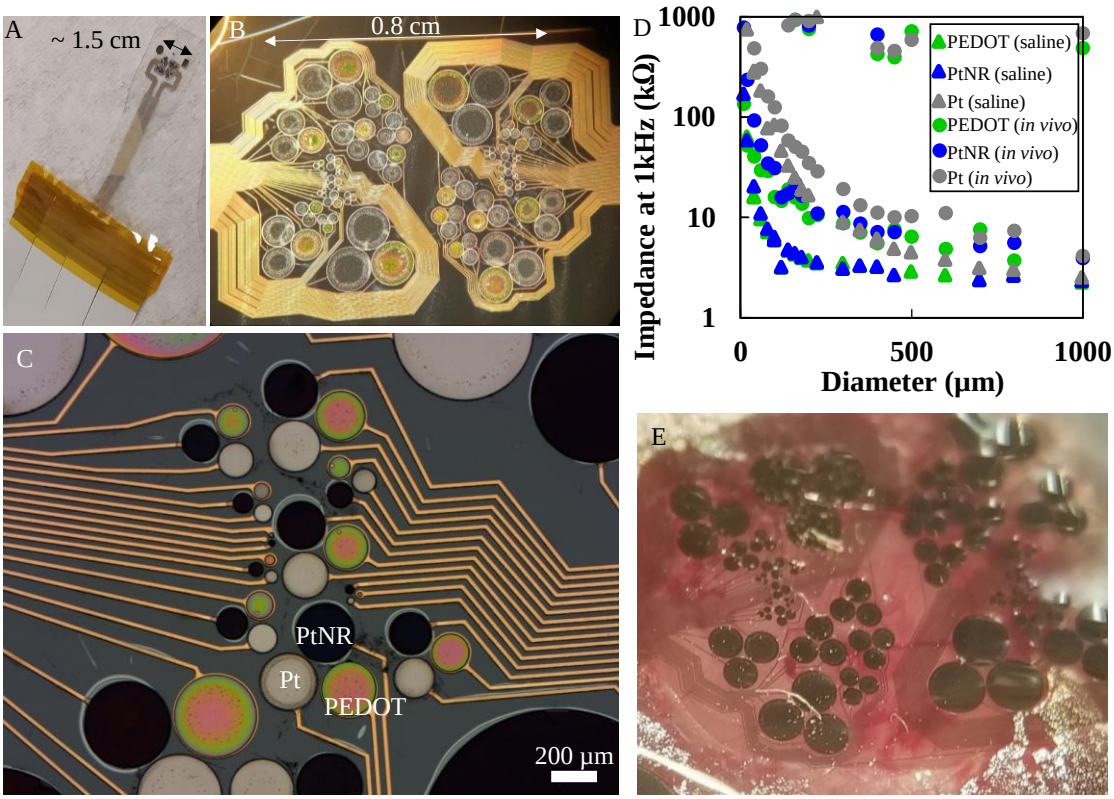


Figure 28 Device geometry for variable diameter multi-material device. A Overview of 128 channel device bonded to ribbon cable. B and C Zoom-in look at diameter clusters with three different electrode materials. D Impedance vs. diameter for three electrode materials during saline measurements and in vivo. E Implantation of device over HVC region of a European Starling.

Since the device structure was larger than the craniotomy, half of the electrodes were centered over the HVC during the recording. Comparing the raw electrophysiology from electrodes with the same material (PEDOT:PSS) but different diameters, the overall shape of the response appeared to be very similar. After high pass filtering the data, the presence of putative spiking activity could be observed as shown in Figure 29, but spikes should be detected across all the electrodes, which seems to be the case here.

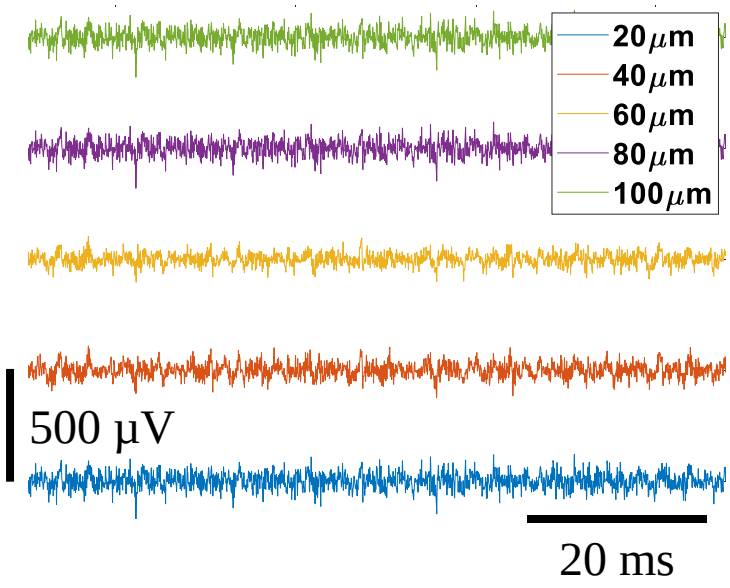


Figure 29 HPF electrophysiology data for electrodes with the same material (PEDOT:PSS) and varying diameters.

Analysis between varying materials while fixing the electrode diameter (80μm) yielded additional similarities between the electrodes.

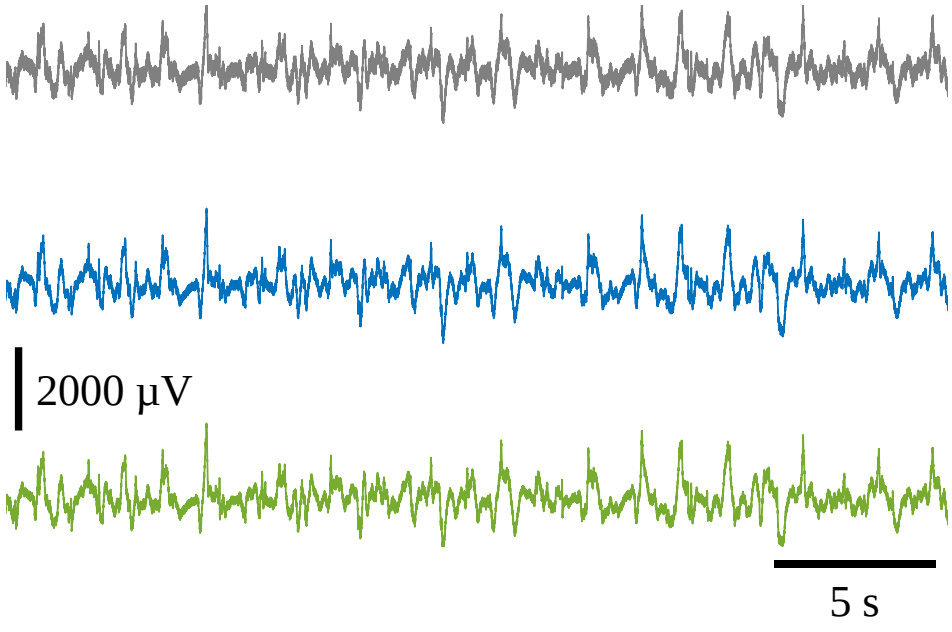


Figure 30 Raw electrophysiology data of electrodes with the same diameter (80 μm) and varying material. The gray trace is planar Pt, the blue trace is PtNR, and the green trace is PEDOT:PSS.

The planar Pt electrodes (gray trace) were slightly more susceptible to noise as shown in Fig. 30, yet the traces across electrode materials looked generally the same. Running the high pass

filtered data through Spike2 some detected units are shown in Fig. 31. The waveforms from all three electrodes show an oscillatory pattern attributed to noise.

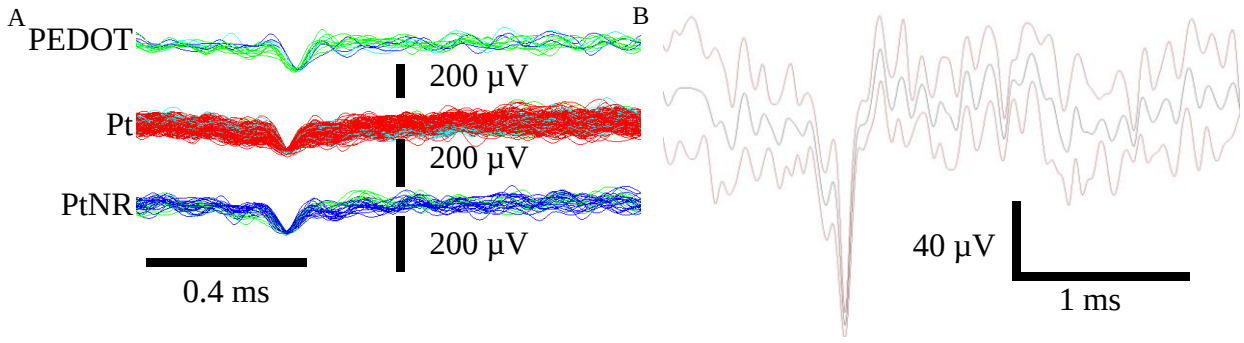


Figure 31 Waveforms of single units detected across three electrodes with varying material. Wave snippets from units detected on PEDOT:PSS (top), Pt (middle), and PtNR (bottom) electrodes. B Average waveform from PtNR electrode.

Several attempts were made to remove the noise, which seemed to affect all of the channels. Noise removal methods were conducted using custom Matlab scripts. The one attempted method was creating a common reference, essentially subtracting the trace from another channel farther away with the hope that noise seen across all channels will be removed while maintaining the single unit activity seen locally on an electrode. The electrodes used for this method as the common reference had diameters of 1000µm and were sufficiently far from the target electrode being analyzed. Table 3 describes the impedances of the electrodes used for this method.

Table 3 Diameter and impedance for common reference analysis

	Material	Diameter (µm)	Impedance at 1kHz (kΩ)
Target	PEDOT	60	40.424
Ref	Pt	1000	4.123
Ref	PEDOT	1000	3.704
Ref	PtNR	1000	3.922

The larger diameter electrodes measured smaller impedance values than the target electrode, as demonstrated in Fig. 28D. Two subtractions were made, one using the average of all three reference traces, and the other of just the PEDOT:PSS reference trace.

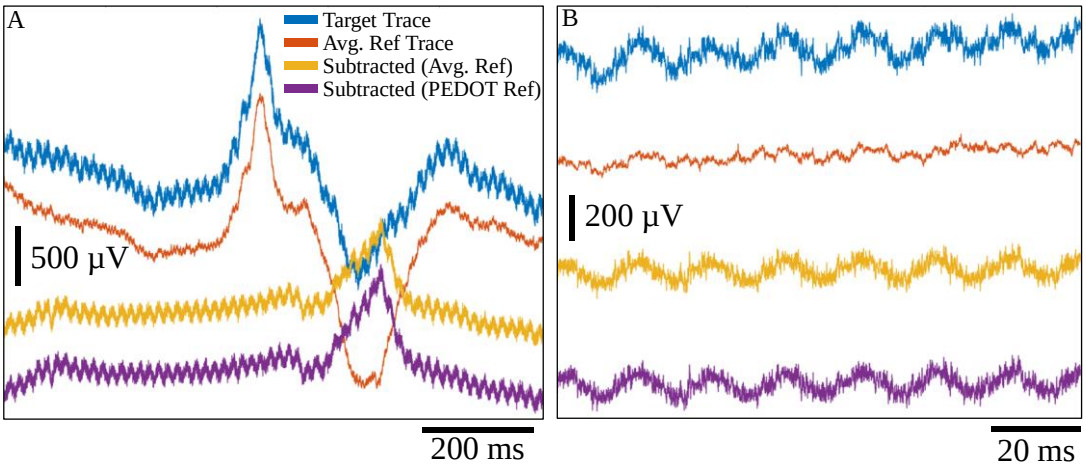


Figure 32 Common reference subtraction to remove noise artifact from target trace.

The subtraction of both an average of three electrode traces and a single reference trace removed the low frequency pattern from the target trace, yet failed to remove the oscillation from the noise artifact as can be observed in Fig. 32. High pass filtering the traces removes the oscillation, yet exposed slight distortions in the traces. Subtracting a common reference channel seemed to distort the data without removing the noise properly as can be concluded from Fig. 33.

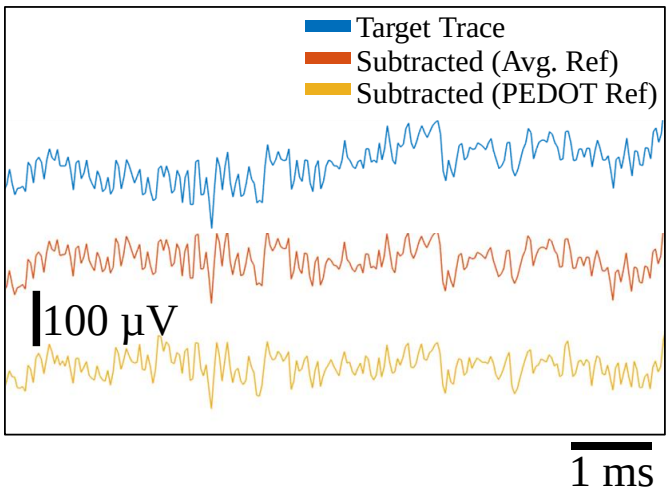


Figure 33 High pass filtered traces of common reference subtraction analysis.

Another method to remove the noise was custom notch filtering. The frequencies removed were determined using periodograms of the trace. Strong 60Hz noise was detected in the data as

can be seen in Fig. 34, which is prominent in power supply that is standardized at 60Hz in the US. Additionally, an 8000Hz frequency component was detected as shown in Figure 34C, which was likely attributing to the high frequency oscillation observed in Figure 31. The notch filter suppressed the power of the 60Hz and its harmonics as well as the 8000Hz component.

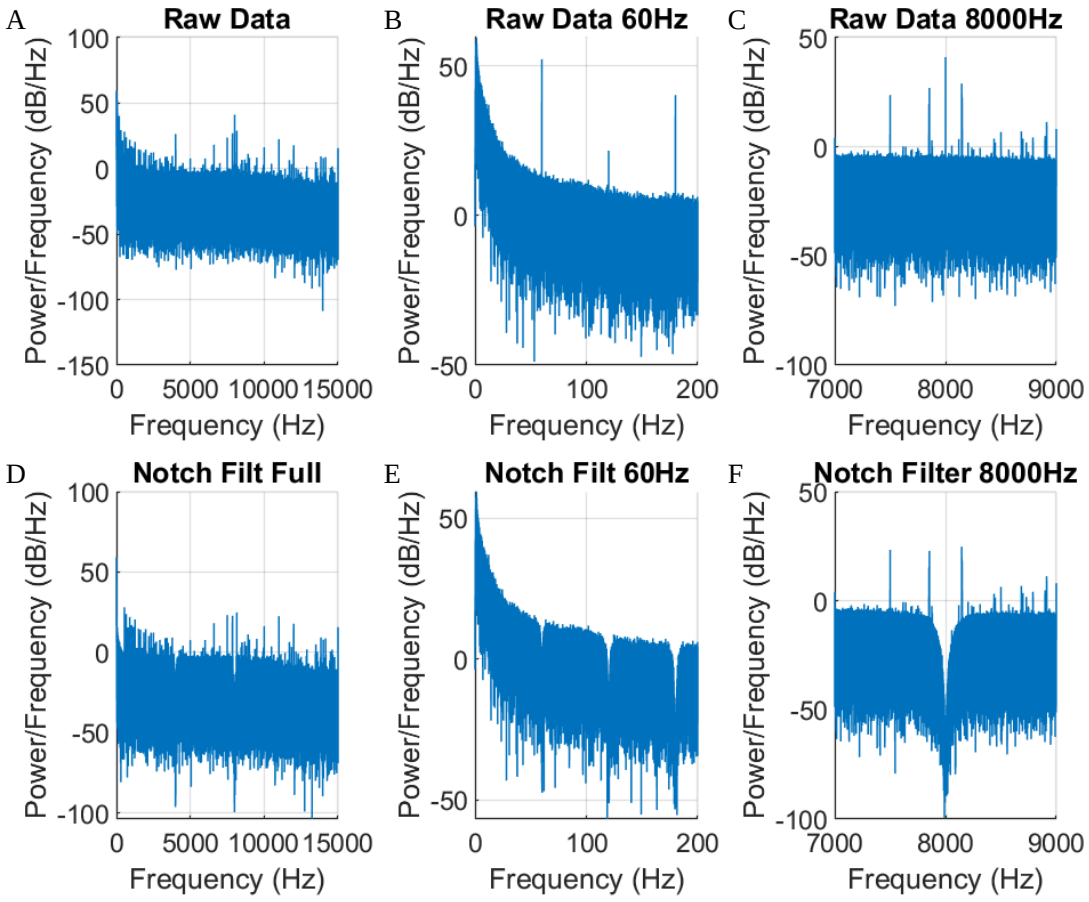


Figure 34 Periodograms to determine the frequencies to remove through notch filtering.

The notch filtering method maintained the low frequency shape of the raw data and removed the oscillation as seen in Figure 35A. After spikesorting the notch filtered data, the average waveform of the detected unit was much smoother than that of the original trace as described in Figure 31.

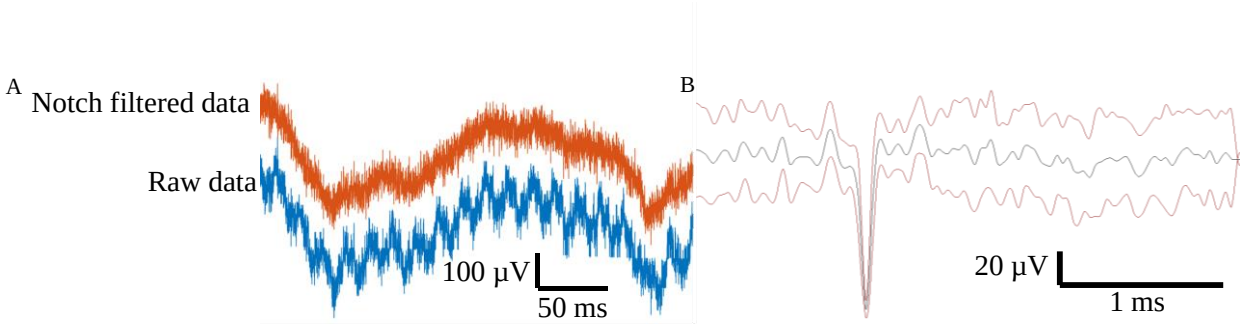


Figure 35 Noise removal through notch filtering.

Unfortunately the presence of the noise artifact made spikesorting inconclusive, since further filtering manipulated and distorted the data. Further experiments are needed to address the noise issue before conclusive analysis can be made.

Chapter 3, in part, is currently being prepared for submission for publication of the material. Hossain, Lorraine; Arneodo, Ezequiel M.; Oh, Hongseok; Gentner, Timothy Q.; Dayeh, Shadi A. The dissertation author will be the primary author of this material.

Chapter 4 Multimodal Chronic Recordings in Awake Mice

Acquiring neural activity from the surface of the brain is considered less-destructive than penetrating electrodes in the context of next generation brain-machine interfaces. Surface probes have are increasingly being applied to neurophysiological investigations in rodents. One such instance involves a 64 channel polyimide array implanted chronically in rats for at least 100 days, with recordings beginning after a two week recovery period[73]. They reported auditory cortex stimulation with 200μs pulse speaker clicks, though it was noted that there were difficulties in presenting the same stimulus amplitude each day[73]. Another group implanted the electrodes on the rat's somatosensory cortex, covered the implant with bioabsorbable gelatin compressed sponge (Gelfoam), and sealed the craniotomy with silicone elastomer[74]. Stimulation was delivered by the means of electric pulses in the hind limb contralateral to the implant until visible movement was observed. Additionally, sleep epochs were recorded to observe sleep spindles and gamma oscillation in NREM, though the stability of the recordings over time was challenging[74]. With implants in the barrel cortex of mice, responses are expected to exhibit spatiotemporal variations along the depth of the cortical column to chronic whisker stimulation[75]. A paper in 2004 found that a stimulus consisting of three whisker deflections result in a nonlinear response and a method could be predicted of neuronal response to various stimulus patterns using a second order representation[76]. Higley et al. saw both linear and nonlinear response in the somatosensory region with synaptic excitation seen through amplitude and spatial distribution of current sinks[77]. Civillico et al. discovered that responses to paired whisker deflection was monophasic with larger amplitude than single response and plotted a linearity index map of the barrel cortex using voltage sensitive dyes through optical recordings in conjunction with electrophysiological response[78]. Previously, Civillico et al. compared optical recordings of whisker and electrical stimulation with respect to

activated cortical areas and speed of activation in the mouse barrel cortex[79]. They found that the initial spreading speed of the response determines total activated area for both types of activation and that there were similar single-response kinetics for whisker and electrical stimulation, but whisker responses had more paired-pulse depression than electrical[79].

Previously, by adapting the use of conformally thin parylene C in conjunction with conductive polymer PEDOT:PSS coating on the electrode sites, we were able to record over several months in mice with chronically implanted devices. In agreement with Schander et al. (2016), we demonstrated minimal tissue response to PEDOT arrays implanted for 10 weeks in rodents through immunohistochemical staining of neurons, astrocytes, and microglial cells[22,30]. Here, we extend this work to show simultaneous 2-photon optical imaging and electrophysiological recordings of cortical neuronal activity in awake mice with chronic PEDOT:PSS microelectrode array implants.

4.1 Sensitivity verification in acute setting

All experimental procedures were performed in accordance with the guidelines established by the University of California San Diego (UCSD) Institutional Animal Care and Use Committee (IACUC). Prior to the surgery, dexamethasone was injected to prevent brain swelling. Mice were anesthetized with Ketamine (100 mg kg^{-1}) and Xylazine (10 mg kg^{-1}), and a single dose of Buprenorphine (0.05 mg kg^{-1}) was applied. A 3 mm diameter craniotomy with the center coordinates of anterior-posterior (A–P) 2 mm and left-right (L–R) 3 mm (relative to bregma) was performed. After bone removal, the electrode array was placed on the dura mater for recording electrophysiological responses seen on the barrel cortex to piezoelectric stimulation of the contralateral whiskers.

By plotting the filtered electrophysiology data according to the spatial geometry of the electrodes, patterns of higher response on certain electrodes can be observed as shown in Fig. 36.

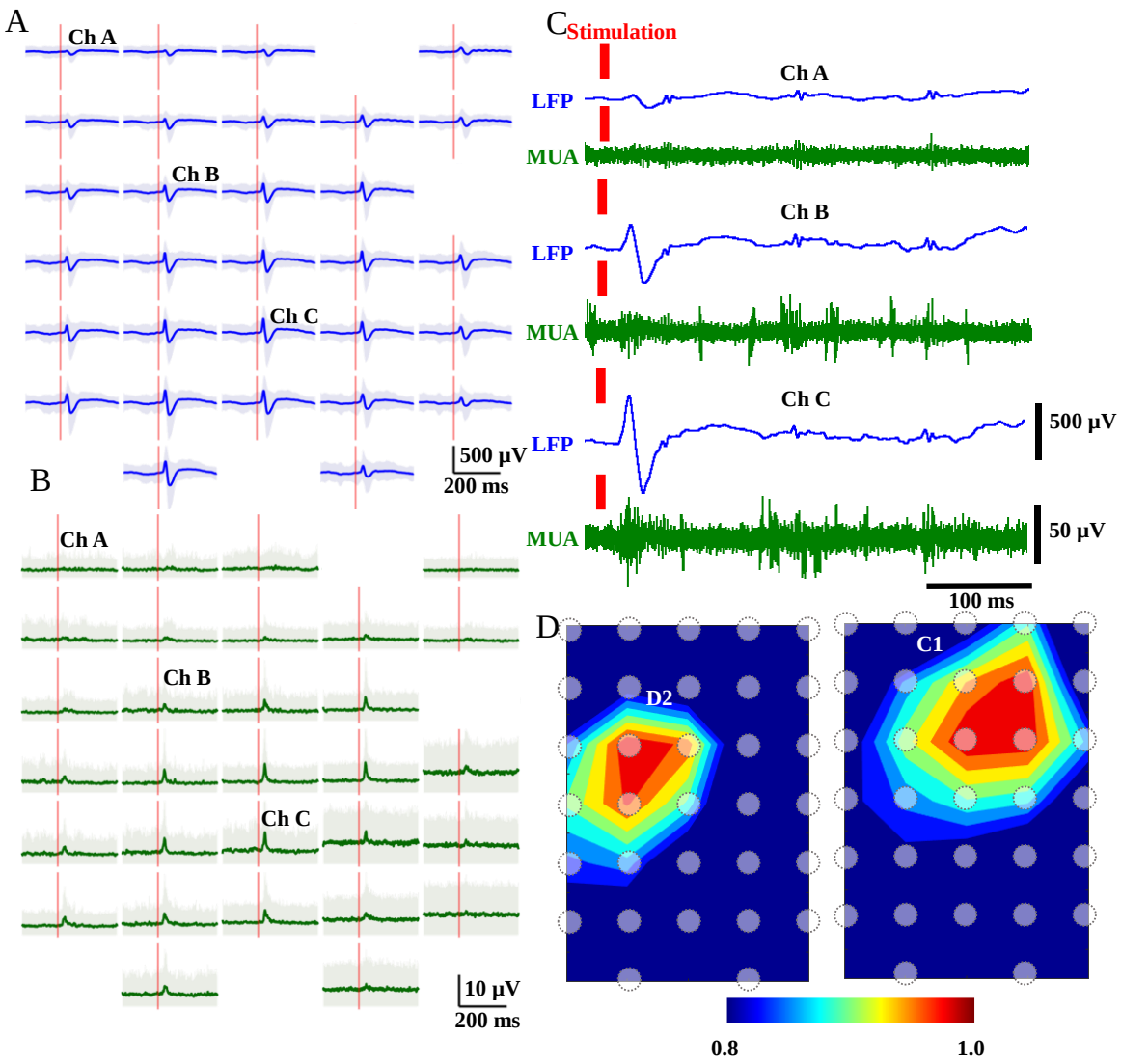


Figure 36 Localized electrophysiological response in acute setting. A Spatial mapping of low pass filtered (250Hz) data, with the average response to the piezoelectric whisker stimulation overlaying individual trials. B Spatial mapping of high pass filtered (270Hz) and rectified data. C Traces from a single trial of stimulation for three channels show decreased response from the epicenter of the stimulation response. D Heat maps of the average waveform amplitude for local field potential activity that shows correlation of the response epicenter on the barrel cortex with the whisker being stimulated.

Both the low pass filtered and the high pass filtered and rectified traces showed that there was a response epicenter localized by the whisker being stimulated, seen with the increasing

amplitude from channel A to channel C in Fig. 36. The strong peak observed in the low pass filtered data in Panel A corresponds to a local field potential (LFP), which is an amalgamation of signal from neighboring neurons. The high pass filtered and rectified traces in Fig. 36B shows a peak of multi-unit activity (MUA), which is an indistinguishable overlay of spikes from multiple neurons. The heatmaps in Figure 36D show the localization of response to piezoelectric stimulation of individual whiskers from two separate recordings, where the D2 and C1 whiskers were stimulated, respectively.

4.2 Chronic recording setup in awake subjects

For chronic awake recordings, validation of evoked response can be better isolated with optogenetic stimulation as opposed to piezoelectric stimulation due to convolution of responses with movement in awake mouse. To this end, we selected Emx1-Cre/Ai32 mice expressing Channelrhodopsin-2 in excitatory neurons[80,81]. Expression of the calcium indicator jRGECO1a was induced via transduction with pAAV.Syn.NES-jRGECO1a.WPRE.SV40[82]. The craniotomy followed the same procedure described in Section 4.2, with the addition of an aluminum headpost mounted over the other (right) hemisphere and a glass window assembly (made of two 3 mm coverslips and one 5 mm coverslip bonded together with optical adhesive) which was fit within the exposure on top of the array. Then, the circumference of the glass window was sealed with dental acrylic. A combination of Sulfatrim and Ibuprofen was given via drinking water from 1 day before until 5 days after surgery to prevent and treat infections and trauma induced by the surgery.

4.2.1 Custom device connectivity

Several iterations of the device form factor were performed to create implants that produced stable recordings in a chronic experiment. The ribbon cables utilized during acute experiments had a large and heavy structure that would not be suitable for the mice to sustain for

long periods of time. The mask design of the device was modified to that seen in Figure 1, so that the device could be bonded to an Omnetics connector, which would connect directly to the Intan chip used during recordings as illustrated in Fig. 37.

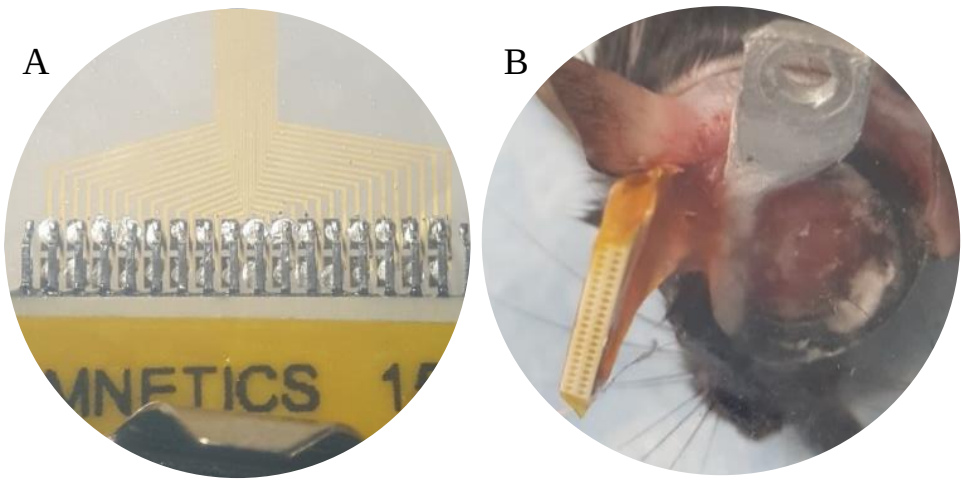


Figure 37 Chronic device form factor with Omnetics connector for direct connection to Intan chip.

The thin parylene C substrate could not sustain numerous connections of the male and female Omnetics connectors throughout the chronic experiment, and the electrodes became damaged over time. To protect the device from the mechanical force of the Omnetics connection, an intermediary set of printed circuit boards (PCB) was designed. This way the Intan chip is connected to the larger PCB, which is then connected via a Molex connector to the smaller PCB that is bonded to the device. While the electrodes seemed to be stable throughout the experiment, the Molex connector was damaged over time, to the point where connection to the larger PCB was impossible. This damage was likely caused while the mouse was moving freely within its cage and rubbing against the food apparatus. Additionally, the non-transparency of the PCB made alignment of the Molex connector rather challenging during recordings.



Figure 38 Chronic implantation with custom PCB utilizing Molex connector. A Chronic device during the first week of implantation. B Chronic device after five weeks of implantation shows degradation of the Molex connector. C Connection of larger PCB board to interface with the Intan recording chip.

Another aspect that needed to be optimized was bonding the device to the glass window before placing the device over the craniotomy. Bonding to the glass coverslip prior to implantation as shown in Fig. 39A maintains optical visibility beneath the device, as shown in Fig. 39C. When the device was not bonded to the glass coverslip prior to implantation, tissue regrowth occurred above the device as shown in Fig. 39B, which greatly impedes the imaging capability. The new tissue introduces a great deal of shadowing.

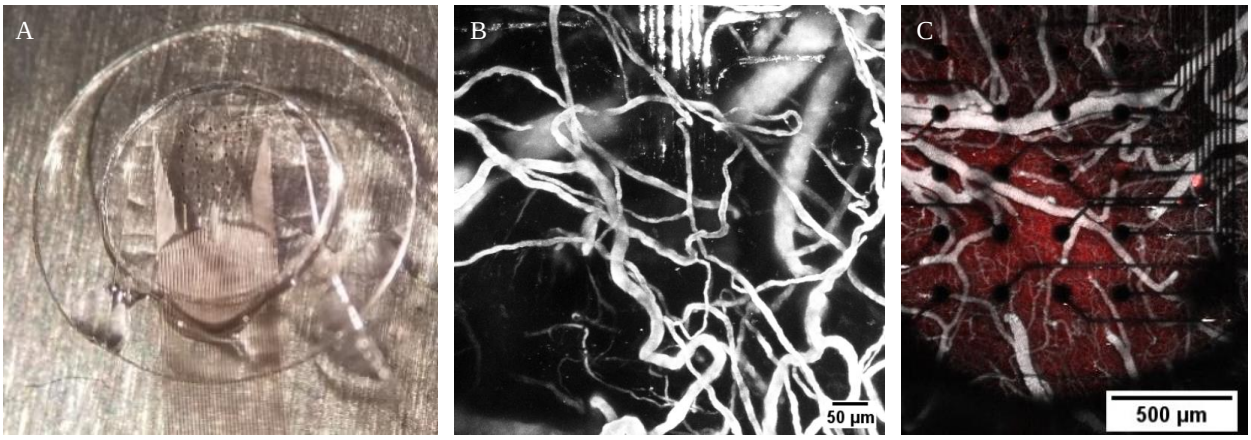


Figure 39 Importance of bonding device to glass window prior to implantation. A Device is secured to glass window with a UV curable epoxy. B Tissue regrowth occurs above the device when not bonded to the glass window. C Bonding the device to the glass window maintains the imaging capability.

The optimized device form factor is shown in Fig. 40. Figure 40A shows the device bonded to the PCB with the electrodes facing up. Figure 40B shows the device within the 3D printed case and with the back of the device bonded to the glass coverslip. The FFC connector proved easier to connect for recordings, and the 3D PCB case successfully maintained the integrity of the PCB throughout the experiment. The entire implant remained small enough for the mouse to move around and exhibit normal behaviors in its cage when not being recorded from as seen in Figure 40C.

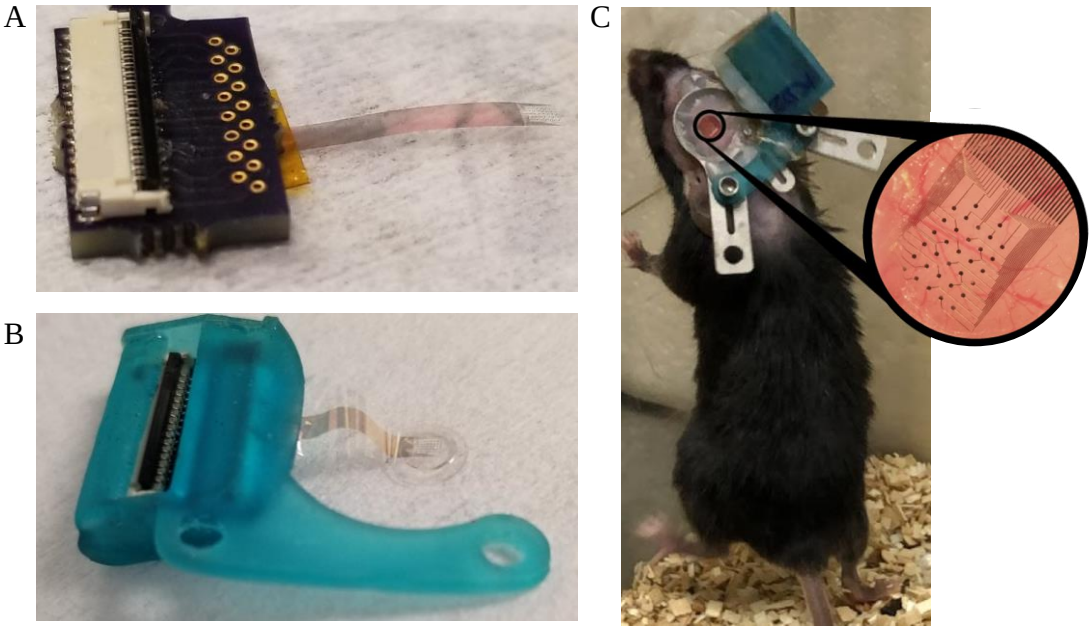


Figure 40 Optimized chronic device. A Flexible parylene C/PEDOT:PSS device bonded to custom PCB board with FFC connector bonded to the back for ribbon cable connectivity. B Custom 3D printed PCB case to protect the PCB while implanted on the rodent. C Fully implanted chronic device with small form factor allows rodent to move freely when not being recorded. Glass window enables simultaneous imaging beneath the device with electrophysiological recordings.

Collaborators also designed and manufactured a custom headstage to improve the stability of the imaging, as seen in Figure 41. The screw holes marked in red on the metal plate allow a secure fit for the PCB board with the implant, and the larger screw holes on the rectangular wings of the plate align with holes on the larger stage during recording. A y-shaped piece, shown as dark

gray in Figure 41B sits atop the metal plate for added security and ease while securing the mouse to the larger stage.



Figure 41 Custom headstage for chronic rodent implants. A Metal plate that is secured above the rodent's skull and is fastened to the implant. B Schematic of the headstage setup for recordings. C Mockup of a rodent secured for recording with the custom PCB case fastened to the metal plate.

When it comes time for recording, the mouse is first secured to the headstage under the 2-photon microscope, and then the electrophysiology equipment is connected as shown in Fig. 42.

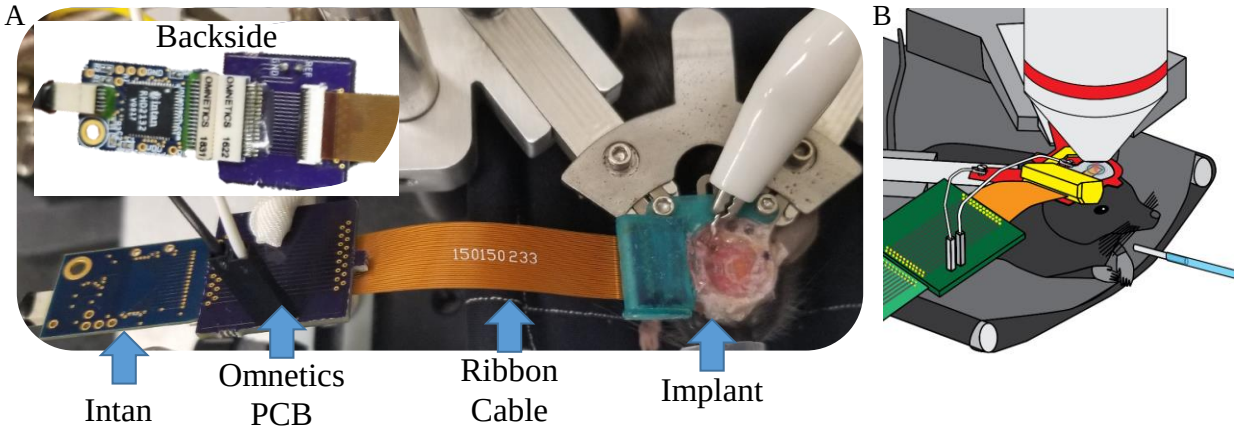


Figure 42 Recording setup for chronic recording of an awake mouse. A Connection of the chronic device via ribbon cable to the larger PCB, which is connected to the Intan chip. B Schematic of recording setup for simultaneous electrophysiology and 2-photon recordings

The reference screw was connected via alligator clips to the PCB board and the ground of the device is connected to the headstage, which is grounded through the microscope table to Earth.

4.2.2 Electrophysiology recording

Electrophysiology data was recorded using Intan recording acquisition electronics, as described in Section 2. The implanted rodent was first put under isoflurane anesthesia before being connected to the headstage setup, after which the anesthesia source is removed. Baseline electrophysiology was recorded as the rodent woke up, and recordings with stimulation only began once the electrophysiology showed awake behavior. Impedance measurements were taken for each recording to track the stability of the electrode-tissue interface over time and is presented in Fig. 43. Impedances remained relatively stable throughout the experiment, with the exception of the increase in impedance from ideal condition measurements in saline solutions to the measurements *in vivo*.

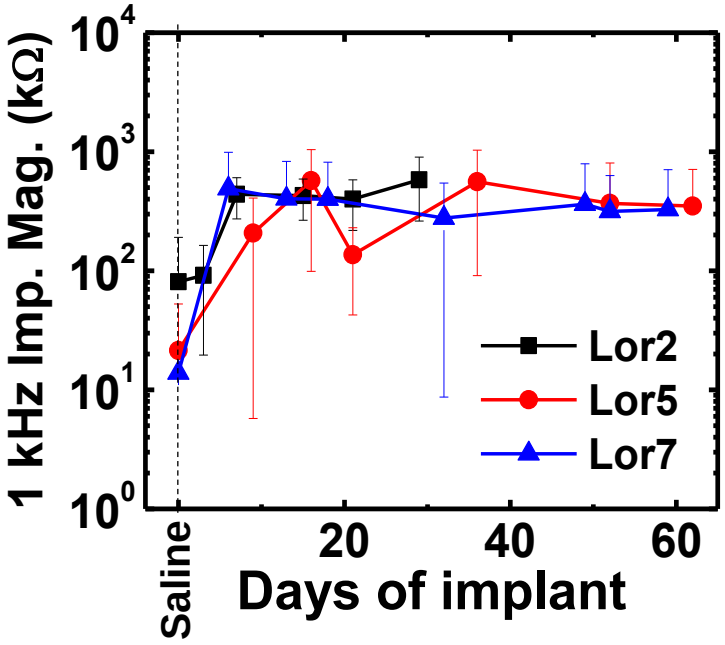


Figure 43 Impedance measurements of chronic implants for up to 60 days.

Three stimuli paradigms were used to evoke electrophysiological responses: optogenetic, as well as airpuff, and sandpaper mechanical displacement of whiskers. The optogenetic

stimulation was delivered through the 2-photon microscope objective with a 473nm cylinder-shaped CW laser beam with a FWHM diameter of 210µm. Duration of the stimulation was modulated with a shutter and typically lasted 5ms or 10ms. A strong LFP response was detected to optogenetic stimulation, as seen in Figure 44. To validate that this response was biophysiological and not caused by an artifact from the light source, recordings were done before and after euthanizing the subject. Under the same recording conditions, the response detected by the PEDOT:PSS/parylene C device was drastically reduced in the post-mortem recordings in Figure 44B. This supports that these electrodes detect neural response to the stimulus.

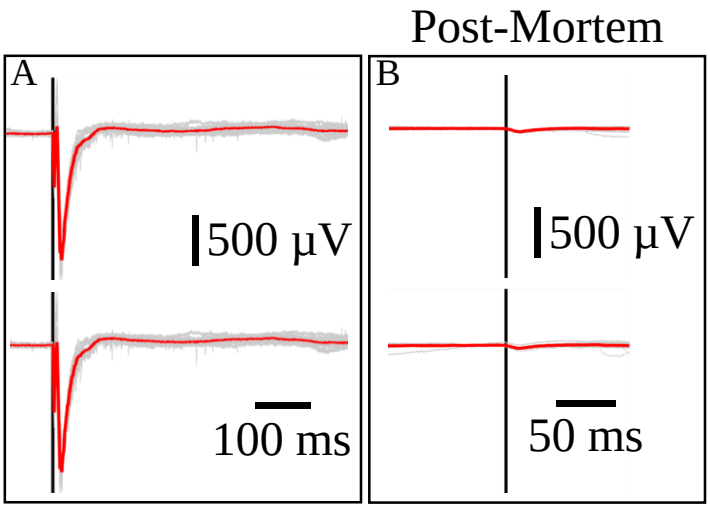


Figure 44 Trial averaged electrophysiological response to optogenetic stimulation on two electrodes. A Recordings while the mouse was awake. B Recordings during the same day with the same conditions after euthanizing the mouse.

Sandpaper stimulation involved a piece of sandpaper adhered to a dowel rod connected to a motor far from the recording setup so as not to introduce noise. When the onset of the stimulus is induced, the dowel rod moves the sandpaper in close proximity to the mouse's whiskers, allowing the whiskers to feel the rough surface. After a stimulus duration of 2s, the sandpaper was moved away from the mouse, followed by a 10s delay before the next stimulus event. Response was weaker to the sandpaper stimulation, as the mouse gradually reacted to the presence of the

rough sandpaper, though an increase in high frequency bursting can be observed after the LFP response.

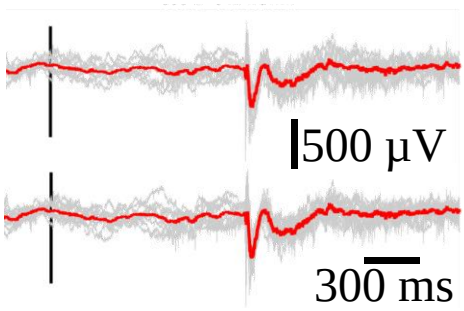


Figure 45 Trial average electrophysiological response to sandpaper stimulation for two electrodes. Black line indicates onset of stimulus. Individual trials shown in gray.

Airpuff stimulation consisted of a rubber tube attached to a PV820 Pneumatic PicoPump (WPI) sending a puff of oxygen at a pressure of 26psi, followed by a 5s delay before the next stimulus event. Response to airpuff stimulation of the whiskers again showed localization like in the acute experiment, although isolation of responses for individual whiskers was not possible.

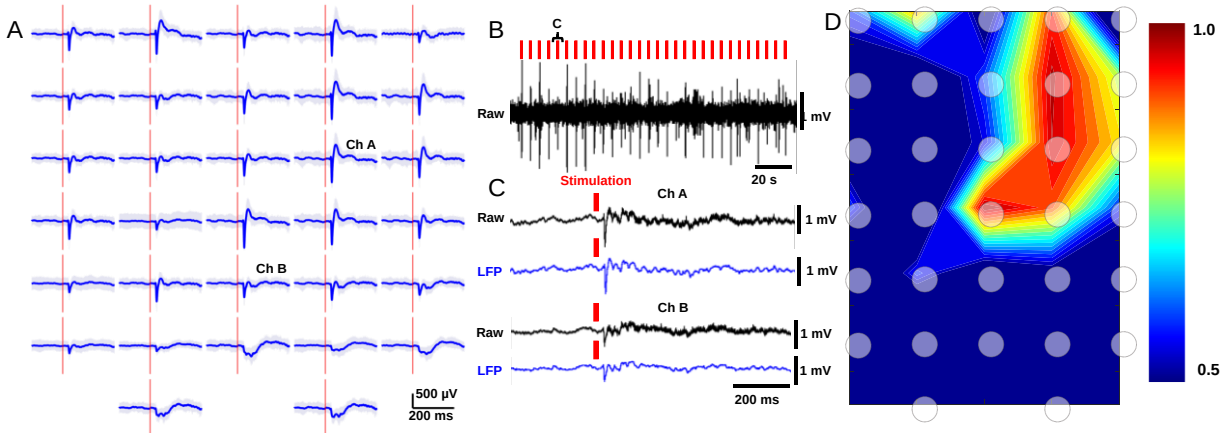


Figure 46 Low pass filtered electrophysiology response to airpuff stimulation shows sensitivity to response.

A strong LFP peak is observed after the onset of the stimulus, with bursting activity in the raw data observed after the stimulus as well, as shown in Fig. 46. The response is consistent throughout the recording, as seen in the raw electrophysiology trace of channel A in Figure 46B,

and Figure 46C shows the change in response intensity from channel A to channel B. The heatmap shows that response to the stimulus was localized on the upper right quadrant of the device.

4.2.3 Calcium imaging using 2-photon microscopy

The transparency of the parylene C and thin metal leads enabled imaging hundreds of microns deep into the cortex.

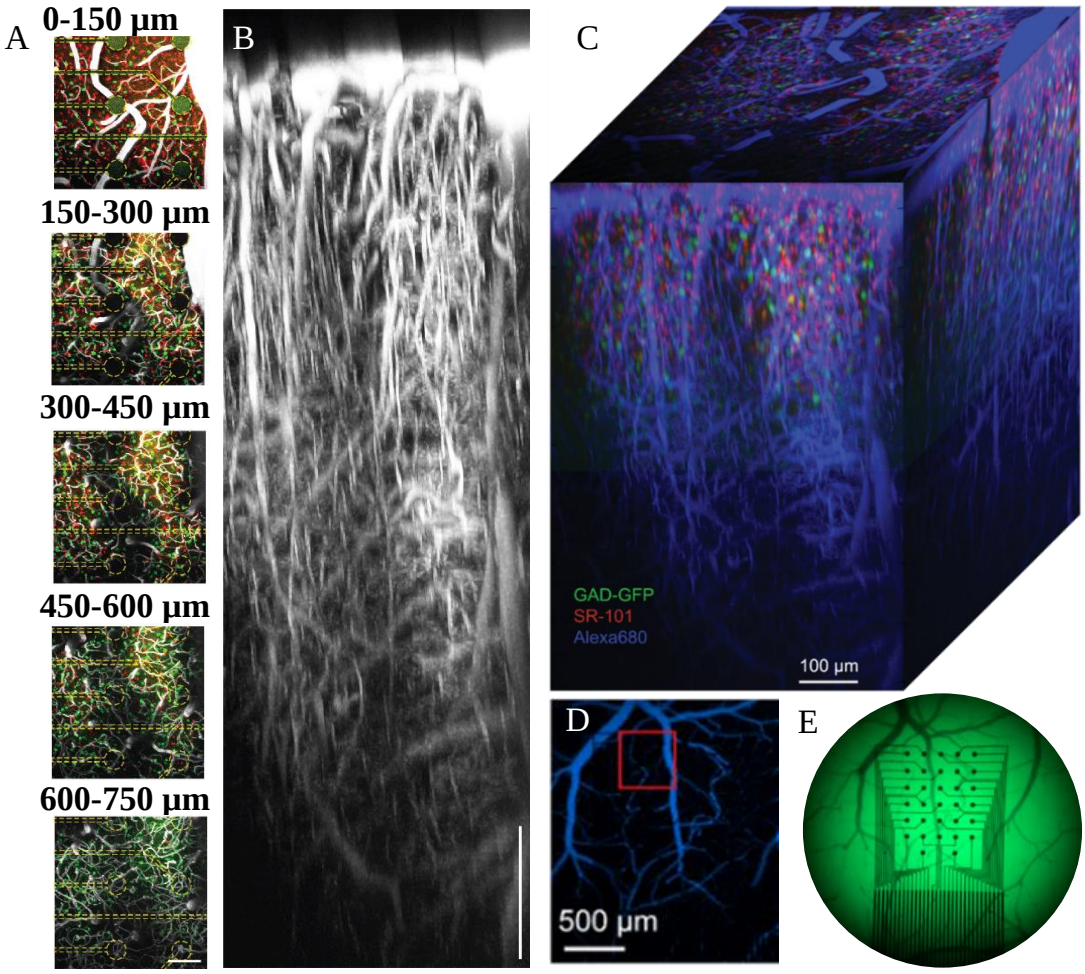


Figure 47 Two-photon imaging of cortical column through an implanted parylene C/PEDOT:PSS device. A Images taken at varying depths beneath the array show minimal shadowing from the metal leads (yellow outline). For these images a GAD67-GFP transgenic mouse expressing enhanced green fluorescent protein (GFP, green) in all inhibitory (GABAergic) cortical neurons, with intravascular injected Alexa680 (white) and Sulforhodamine 101 (SR-101, red) was used. B Orthogonal (XZ) representation of the images sampled in A. C 3D cube representation of the z-stack image with D showing the region of interest for the imaging and E showing the implanted device.

The two-photon images were acquired using an Ultima two-photon laser scanning microscopy system from Bruker Fluorescence Microscopy using an optical parametric oscillator tuned to 1360nm (Chameleon Compact OPO, Coherent) that was pumped by a Ti:sapphire laser at 790nm, with a 20x water immersion objective (UMPLFLN20XW, Olympus). Intravascular injection of Alexa Fluo 680-dextran (2 MDa) enabled detection of the vasculature, Sulforhodamine 101 (SR-101) enabled detection of astrocytes, and the GAD67-GFP transgenic nature of the mouse enabled fluorescent expression of inhibitory (GABAergic) cortical neurons.[83,84]

Although the electrophysiology was not affected by an optogenetic artifact, as seen in Figure 44, the use of the optogenetic light source during calcium imaging introduced an artifact. This was because a shutter was time-synced to initiate during the optogenetic stimulation to protect the sensitive PMT crystals of the 2-photon capture. The absence of 2-photon imaging during this time was read during image processing as darkness, which falsely caused a dip in the fluorescence intensity trace. Also occasionally the line scan of 2-photon imaging caught the tail end or brief start of the stimulus. The brightness from the optogenetic source then skewed the image processing of the calcium fluorescence intensity beyond the normal fluctuations of calcium indicator in the cells, making removal of the artifact challenging. For this reason, analysis of combined electrophysiology and calcium imaging was focused on airpuff and sandpaper stimulation.

4.3 Behavioral electrophysiological recordings and calcium imaging

By plotting the electrophysiology and calcium traces, time-locked response to stimulation events were observed.

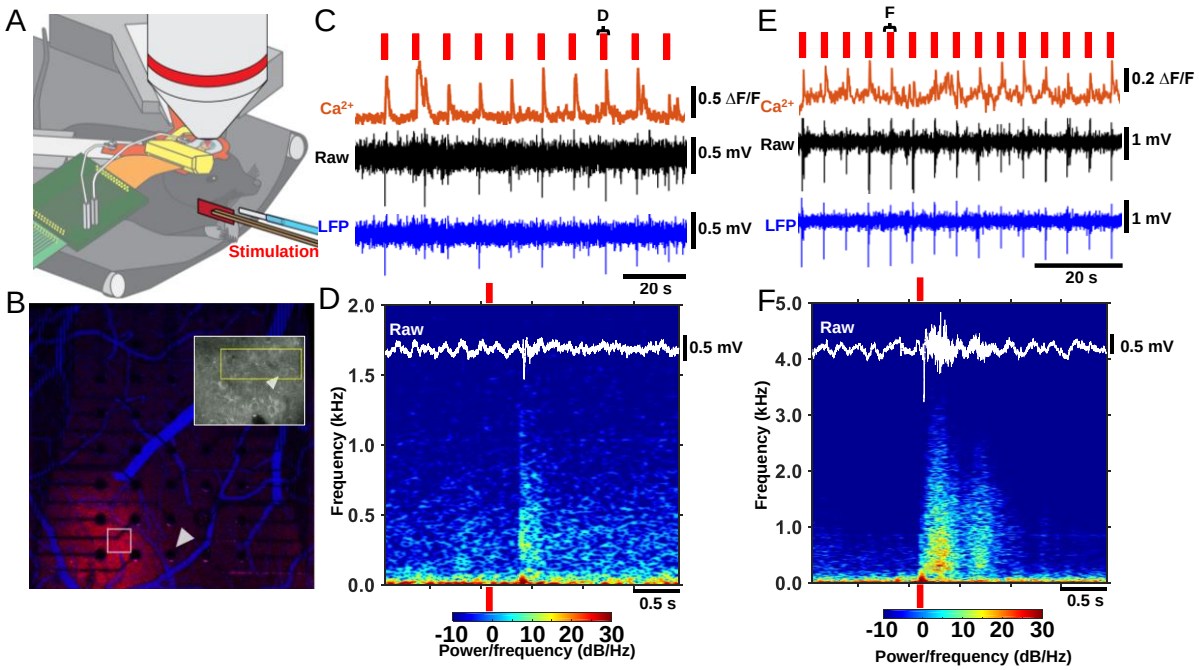


Figure 48 Simultaneous Ca imaging and electrophysiology in chronically implanted, awake mice. A Schematic of recording setup for airpuff and sandpaper stimulation. B Region of interest for Ca imaging. The white arrow in the larger image indicates the electrode used for the electrophysiology analysis, and white arrow within the inset marks the neuron plotted as the Ca^{2+} trace in C and E. C Traces of the change in fluorescence intensity for calcium data, the raw electrophysiology data, and the low pass filtered electrophysiology data for sandpaper stimulation. D Spectrogram of the raw electrophysiology response to a single sandpaper stimulation event. E Response traces as in C but to airpuff stimulation. F Spectrogram of the raw electrophysiology response to a single airpuff stimulation event.

Electrodes directly adjacent to the region of interest exhibited an artifact from the 2-photon beam, so a neighboring electrode was selected for the analysis. The orange traces in Figures 48C and 48E represent the change in fluorescence intensity due to calcium indicator expression of a single cell. The time-locked peaks indicate that the observed cell is activated with the sandpaper or airpuff stimulation, respectively. Concurrently, the electrophysiology also exhibited strong event related potentials, with strong LFP peaks observed in the blue traces. The optical modality has distinguished merits compared to the electrophysiology modality including cellular specificity and volumetric recordings. Electrophysiological recordings, on the other hand, can capture the fast neuronal dynamics that might be missed with the slower temporal resolution of calcium imaging.

This is why combining the two recording modalities can enable further understanding of neural behavior.

4.4 Single unit analysis

Apart from LFP response, activity was observed in the high frequency regime, indicating the presence of multi- and single units. The inter-spike-interval histogram in Fig. 49D shows a refractory period without violation, which is indicative for the recording of single unit activity. As Figure 49A shows, there was activity visible in the high pass filtered trace not contained within the cluster of the unit presented in Figure 49B-D.

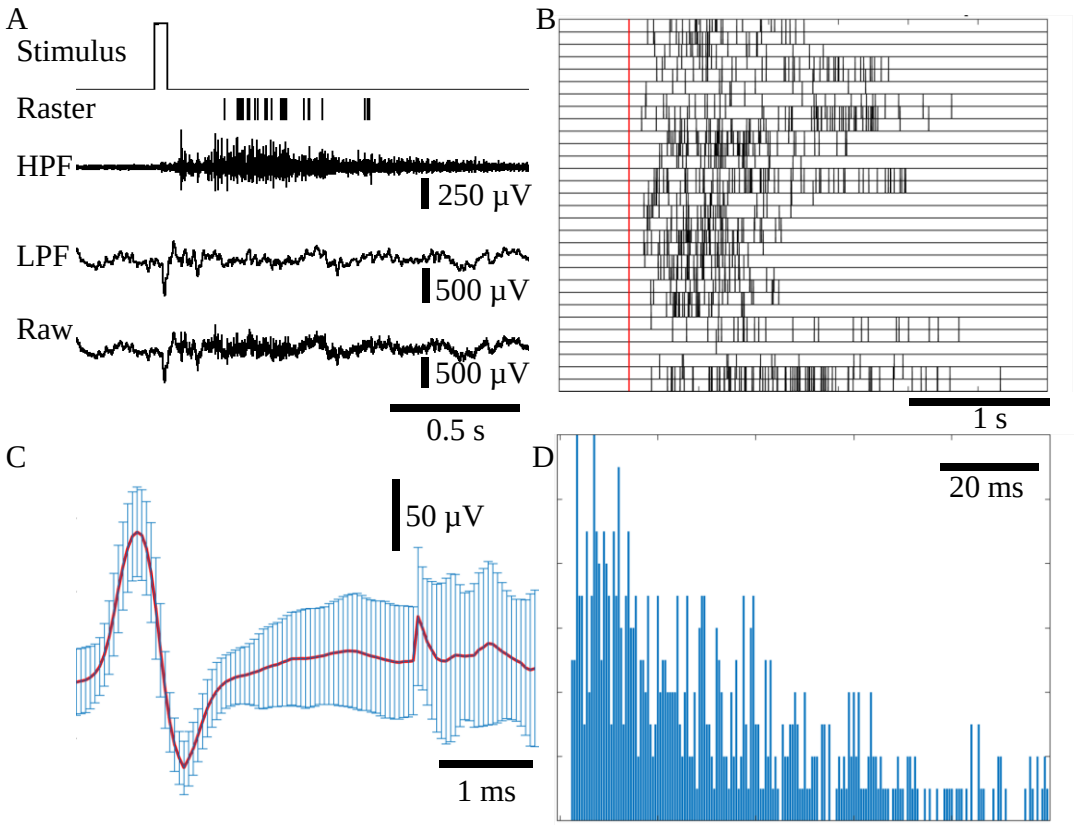


Figure 49 High frequency activity detection in response to airpuff stimulation. A Electrophysiology response to one stimulus event in order from top to bottom: trigger onset of the stimulus, raster of a single unit detected, high pass filtered (270Hz) data, low pass filtered (230Hz) data, and raw electrophysiology data. B Raster plot of spiking activity from a single unit in response to airpuff stimulus (red line marks onset). Each row is a trial during the continuous recording. C Average waveform from one unit Blue marks the standard deviation. D The inter-spike-interval histogram for the unit in B and C.

The bursting of high frequency activity not contained within a single cluster suggests either the presence of additional units detected on that particular electrode, or noise artifact in the high frequency regime. Certainly, video recording of the awake mouse showed that the mouse moved throughout the recording, especially after the onset of airpuff stimulation. As Figure 50 shows, increased MUA activity, seen as the black trace, coincides with increased motion of the mouse. Typically the bursting events aligned with the stimulation onset (red line) with a secondary burst following shortly afterwards, as in Figure 50A, but occasionally the mouse exhibited spontaneous motion not aligned with the stimulus onset, as in Figure 50B. Even if a bursting event began before the stimulus onset, however, a strong MUA response is still observed after the stimulus was presented.

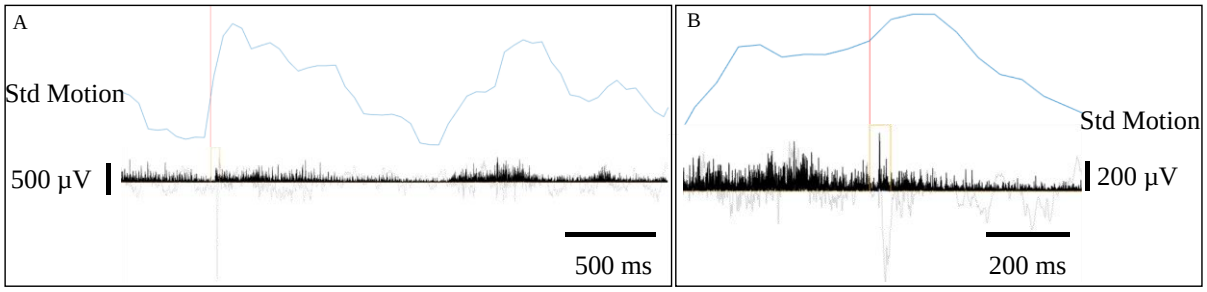


Figure 50 Time locking of the mouse motion, measured as the standard deviation or variation in the region of the mouse whiskers as detected from a webcam and the electrophysiology traces of LFP (gray) and MUA (black).

Whether this motion induced artificial artifacts in the electrophysiology recordings or indicated whisking response to the stimulus – which would correspond with spiking activity in the barrel cortex – is hard to conclusively say with the current experiments. More experiments would need to be conducted to try isolating the motion effect from the neurophysiological response.

4.5 Discussion

Upon whisker stimulation through an airpuff, we observed an electrophysiological response as well as calcium response in awake mice without anesthesia or sedation. The average

amplitude of electrophysiological response to the stimulation yielded over 1 mV across channels, while cells observed around 20-60% change in fluorescence intensity. This is the first instance of simultaneous chronic neurorecordings using PEDOT:PSS microelectrode devices, 2-photon calcium imaging, and whisker stimulation in awake mice that can detect broadband electrophysiology of stimulus-related response as well as spontaneous activity. Notably, stimulus-locked spiking activity recorded together with Ca^{++} transients from individual cells were attained opening the door for future localization of cells contributing to single unit activity measured with PEDOT devices in our[85,86] and in prior work[1].

Chapter 4, in part, is currently being prepared for submission for publication of the material. Hossain, Lorraine; Rogers, Nick; Oh, Hongseok; Lee, Keundong; Lee, Sang Heon; Kılıç, Kıvılcım; Gilja, Vikash; Devor, Anna; Dayeh, Shadi A.; Thunemann, Martin; The dissertation author will be the primary author of this material.

Chapter 5 Conclusion

The flexible nature of the thin parylene C substrate enables conformal contact with the biological tissue, and the enhanced electrochemical properties of the PEDOT:PSS coating improves the signal quality. These features combined allowed for improved electrophysiological recording quality, from detecting single units from the cortical surface in birds and rodents to detecting broadband activity after three months in chronic implants. The transparency of the parylene C and thin metal leads allowed investigation of 2-photon imaging deep into the barrel cortex of rodents during simultaneous electrophysiology recordings. The fabrication process can be modified and scaled according to the subject species and recording goals, which opens up the possibility to explore numerous questions about neurophysiological investigations of behavior.

REFERENCES

1. Khodagholy, Dion, Gelinas, Jennifer N., Thesen, Thomas, Doyle, Werner, Devinsky, Orrin, Malliaras, George G. & Buzsáki, György. t e c h n ic a l r e p o r t s NeuroGrid : recording action potentials from the surface of the brain. **18**, 310–316 (2015).

2. Khodagholy, Dion, Gelinas, Jennifer N., Thesen, Thomas, Doyle, Werner, Devinsky, Orrin, Malliaras, George G. & Buzsáki, György. NeuroGrid : recording action potentials from the surface of the brain. *Nature neuroscience* (2014) doi:10.1038/nn.3905.

3. Devor, Anna, Bandettini, Peter A., Boas, David A., Bower, James M., Buxton, Richard B., Cohen, Lawrence B., Dale, Anders M., Einevoll, Gaute T., Fox, Peter T., Franceschini, Maria Angela, Friston, Karl J., Fujimoto, James G., Helmchen, Fritjof, Hyman, Bradley T., Jasanoff, Alan, Jernigan, Terry L., Judd, Lewis L., Kim, Seong gi, Kleinfeld, David, *et al.* The Challenge of Connecting the Dots in the B.R.A.I.N. *Neuron* **80**, 270–274 (2013).

4. Alivisatos, A. Paul, Chun, Miyoung, Church, George M., Deisseroth, Karl, John, P., Greenspan, Ralph J., Mceuen, Paul L., Roukes, Michael L. & Terrence, J. The Brain Activity Map. *Science* **339**, 1284–1285 (2013).

5. Carmena, Jose M., Lebedev, Mikhail A., Crist, Roy E., O'Doherty, Joseph E., Santucci, David, Henriquez, Craig S. & Nicolelis, Miguel A. L. Learning to Control a Brain–Machine Interface for Reaching and Grasping by Primates. *PLoS Biology* **1**, E42 (2003).

6. Serruya, M. D., Hatsopoulos, N. G., Paninski, L., Fellows, M. R. & Donoghue, J. P. Brain-machine interface: Instant neural control of a movement signal. *Nature* **416**, 141–142 (2002).

7. Hochberg, L. R., Serruya, M. D., Friehs, GM, Mukand, J. A., Saleh, M., Caplan, A. H., Branner, A., Chen, D., Penn, RD & Donoghue, J. P. Neuronal ensemble control of prosthetic devices by a human with tetraplegia. *Nature* **442**, 164–171 (2006).

8. Hochberg, L. R., Bacher, D., Jarosiewicz, B., Masse, NY, Simeral, J. D., Vogel, J., Haddadin, S., Liu, J., Cash, Sydney S., van der Smagt, P. & Donoghue, J. P. Reach and grasp by people with tetraplegia using a neurally controlled robotic arm. *Nature* **485**, 372–375 (2012).

9. Woods, Virginia, Wang, Charles, Bossi, Silvia, Insanally, Michele, Trumpis, Michael, Froemke, Robert & Viventi, Jonathan. A low-cost, 61-channel uECoG array for use in rodents. *International IEEE/EMBS Conference on Neural Engineering, NER* 573–576 (2015) doi:10.1109/NER.2015.7146687.

10. Ha, Sohmyung, Park, Jongkil, Chi, Yu M., Viventi, Jonathan, Rogers, John & Cauwenberghs, Gert. 85 dB Dynamic Range 1.2 mW 156 kS/s Biopotential Recording IC for High-Density ECoG Flexible Active Electrode Array. *IEEE* 141–144 (2013).

11. Du, Zhanhong Jeff, Luo, Xiliang, Weaver, Cassandra, Cui, Xinyan Tracy & Jolla, La.

Poly(3, 4-ethylenedioxythiophene)-ionic liquid coating improves neural recording and stimulation functionality of MEAs. *J Mater Chem C Mater Opt Electron Devices* **3**, 6515–6524 (2015).

12. Thongpang, S., Richner, T. J., Brodnick, S. K., Schendel, a., Kim, J., Wilson, J. a., Hippensteel, J., Krugner-Higby, L., Moran, D., Ahmed, a. S., Neimann, D., Sillay, K. & Williams, J. C. A Micro-Electrocorticography Platform and Deployment Strategies for Chronic BCI Applications. *Clinical EEG and Neuroscience* **42**, 259–265 (2011).

13. Wang, Wei, Degenhart, Alan D., Collinger, Jennifer L., Vinjamuri, Ramana, Sudre, Gustavo P., Adelson, P. David, Holder, Deborah L., Leuthardt, Eric C., Moran, Daniel W., Boninger, Michael L., Schwartz, Andrew B., Crammond, Donald J., Tyler-Kabara, Elizabeth C. & Weber, Douglas J. Human motor cortical activity recorded with micro-ECoG electrodes during individual finger movements. *Proceedings of the 31st Annual International Conference of the IEEE Engineering in Medicine and Biology Society: Engineering the Future of Biomedicine, EMBC 2009* 586–589 (2009) doi:10.1109/IEMBS.2009.5333704.

14. Schalk, Gerwin & Leuthardt, Eric C. Brain-Computer Interfaces Using Electrocorticographic Signals. *IEEE Reviews in Biomedical Engineering* **4**, 140–154 (2011).

15. Schalk, G., Miller, K. J., Anderson, N. R., Wilson, J. A., Smyth, M. D., Ojemann, J. G., Moran, D. W., Wolpaw, J. R. & Leuthardt, E. C. Two-Dimensional Movement Control Using Electrocorticographic Signals in Humans. *Journal of Neural Engineering* **5**, 75–84 (2009).

16. Kim, Dae hyeong, Viventi, Jonathan, Amsden, Jason J., Xiao, Jianliang, Kim, Yun soung, Blanco, Justin a, Panilaitis, Bruce, Frechette, Eric S., Contreras, Diego, Kaplan, David L., Omenetto, Fiorenzo G., Huang, Yonggang, Zakin, Mitchell R., Litt, Brian & Rogers, John a. Dissolvable Films of Silk Fibroin for Ultrathin, Conformal Bio-Integrated Electronics. *Nature Materials* **9**, 511–517 (2011).

17. Khodagholy, Dion, Doublet, Thomas, Gurfi, Moshe, Quilichini, Pascale, Ismailova, Esma, Leleux, Pierre, Herve, Thierry, Sanaur, Sébastien, Bernard, Christophe & Malliaras, George G. Highly Conformable Conducting Polymer Electrodes for In Vivo Recordings. *Advanced Healthcare Materials* **23**, 268–272 (2011).

18. Khodagholy, Dion, Rivnay, Jonathan, Sessolo, Michele, Gurfinkel, Moshe, Leleux, Pierre, Jimison, Leslie H., Stavrinidou, Eleni, Herve, Thierry, Sanaur, Sébastien, Owens, Róisín M. & Malliaras, George G. High transconductance organic electrochemical transistors. *Nature communications* **4**, 2133 (2013).

19. Stavrinidou, Eleni, Leleux, Pierre, Rajaona, Harizo, Khodagholy, Dion, Rivnay, Jonathan, Lindau, Manfred, Sanaur, Sébastien & Malliaras, George G. Direct Measurement of Ion Mobility in a Conducting Polymer. *Advanced Materials* 1–6 (2013) doi:10.1002/adma.201301240.

20. Crispin, X., Jakobsson, F. L. E., Crispin, A., Grim, P. C. M., Andersson, P., Volodin, A., Haesendonck, C. Van, Auweraer, M. Van Der, Salaneck, W. R. & Berggren, M. The Origin of the High Conductivity of (PEDOT-PSS) Plastic Electrodes. *Chem. Mater.* **18**, 4354–4360 (2006).

21. Starbird, Ricardo, García-gonzález, Carlos A., Smirnova, Irina, Krautschneider, Wolfgang H. & Bauhofer, Wolfgang. Synthesis of an organic conductive porous material using starch aerogels as template for chronic invasive electrodes. *Materials Science & Engineering C* **37**, 177–183 (2014).

22. Schander, A., Teßmann, T., Strokov, S., Stemmann, H., Kreiter, A. K. & Lang, W. In-vitro Evaluation of the Long-term Stability of PEDOT : PSS Coated Microelectrodes for Chronic Recording and Electrical Stimulation of Neurons. *IEEE* 6174–6177 (2016).

23. Turner, J. N., Shain, W., Szarowski, D. H., Andersen, M., Martins, S., Isaacson, M. & Craighead, H. Cerebral Astrocyte Response to Micromachined Silicon Implants. *Experimental Neurology* **49**, 33–49 (1999).

24. Biran, Roy, Martin, David C. & Tresco, Patrick A. Neuronal cell loss accompanies the brain tissue response to chronically implanted silicon microelectrode arrays. *Experimental Neurology* **195**, 115–126 (2005).

25. Mols, Katrien, Musa, Silke, Nuttin, Bart, Liesbet, L. & Vincent, B. In vivo characterization of the electrophysiological and astrocytic responses to a silicon neuroprobe implanted in the mouse neocortex. *Nature Scientific Reports* **7**, 1–10 (2017).

26. Liu, Xindong, Mccreery, Douglas B., Carter, Randy R., Bullara, Leo A., Yuen, Ted G. H. & Agnew, William F. Stability of the Interface Between Neural Tissue and Chronically Implanted Intracortical Microelectrodes. *IEEE Transactions on Rehabilitation Engineering* **7**, 315–326 (1999).

27. Lecomte, Aziliz, Descamps, Emeline, Bergaud, Christian, Hara, Seth A., Kim, Brian J., Xu, Huijing, Hirschberg, Ahuva Weltman, Interfacing, Neural, Ramadi, Khalil B. & Cima, Michael J. Silk and PEG as means to stiffen a parylene probe for insertion in the brain : toward a double time-scale tool for local drug delivery. *J Micromech. Microeng.* **25**, (2015).

28. Szarowski, D. H., Andersen, M. D., Retterer, S., Spence, A. J. & Isaacson, M. Brain responses to micro-machined silicon devices. *Brain Research* **983**, 23–35 (2003).

29. Zhong, Yinghui & Bellamkonda, Ravi V. Dexamethasone-coated neural probes elicit attenuated inflammatory response and neuronal loss compared to uncoated neural probes. *Brain Research* **1148**, 15–27 (2007).

30. Ganji, Mehran, Hossain, Lorraine, Tanaka, Atsunori, Thunemann, Martin, Halgren, Eric, Gilja, Vikash, Devor, Anna & Dayeh, Shadi A. Monolithic and Scalable Au Nanorod Substrates Improve PEDOT-Metal Adhesion and Stability in Neural Electrodes. *Advanced Healthcare Materials* **7**, 1800923 (2018).

31. Ganji, Mehran, Paulk, Angelique C., Yang, Jimmy C., Vahidi, Nasim W., Lee, Sang Heon, Liu, Ren, Hossain, Lorraine, Arneodo, Ezequiel M., Thunemann, Martin, Shigyo, Michiko, Tanaka, Atsunori, Ryu, Sang Baek, Lee, Seung Woo, Tchoe, Youngbin, Marsala, Martin, Devor, Anna, Cleary, Daniel R., Martin, Joel R., Oh, Hongseok, *et al.* Selective Formation of Porous Pt Nanorods for Highly Electrochemically Efficient Neural Electrode Interfaces. *Nano Letters* **19**, 6244–6254 (2019).

32. Doupe, Allison J. & Kuhl, Patricia K. BIRDSONG AND HUMAN SPEECH : Common Themes and Mechanisms. *Annu. Rev. Neurosci.* **22**, 567–631 (1999).

33. Prather, Jonathan F. & Bolhuis, Johan J. Brains for birds and babies : Neural parallels between birdsong and speech acquisition. *Neuroscience and Biobehavioral Reviews* (2017) doi:10.1016/j.neubiorev.2016.12.035.

34. Abe, Kentaro & Watanabe, Dai. Songbirds possess the spontaneous ability to discriminate syntactic rules. *Nature Publishing Group* **14**, 1067–1074 (2011).

35. Bregman, Micah R., Patel, Aniruddh D. & Gentner, Timothy Q. Songbirds use spectral shape, not pitch, for sound pattern recognition. *Proceedings of the National Academy of Sciences* **113**, 1666–1671 (2016).

36. Hulse, Stewart H., Cynx, Jeffrey & Humpal, John. Relative and absolute pitch discrimination in serial pitch perception by birds. *Journal of Experimental Psychology: General* **113**, 38–54 (1984).

37. Plantinga, Judy & Trainor, Laurel J. Memory for melody: Infants use a relative pitch code. *Cognition* **98**, 1–11 (2005).

38. Page, SC, Hulse, SH & Cynx, J. Relative pitch perception in the European starling (Sturnus vulgaris): further evidence for an elusive phenomenon. *J Exp Psychol Anim Behav Process* **15**, 137–146 (1989).

39. Kozlov, Andrei S. & Gentner, Timothy Q. Central auditory neurons have composite receptive fields. *Proceedings of the National Academy of Sciences* **113**, 1441–1446 (2016).

40. Margoliash, Daniel & Bankes, Steven C. Computations in the Ascending Auditory Pathway in Songbirds Related to Song Learning. *Am. Zool.* **33**, 94–103 (1993).

41. Volman, S. F. Quantitative assessment of song selectivity in the zebra finch 'high vocal center'. *J Comp Physiol A* **178**, 849–862 (1996).

42. Margoliash, D. Evaluating theories of bird song learning: implications for future directions. *J Comp Physiol A* **188**, 851–866 (2002).

43. McCasland, James S. & Konishi, Masakazu. Interaction between auditory and motor activities in an avian song control nucleus. *Proc. Natl. Acad. Sci. USA* **78**, 7815–7819 (1981).

44. Yu, Albert C. & Margoliash, Daniel. Temporal Hierarchical Control of Singing in Birds. *Science* **273**, 1871–1875 (1996).

45. George, Isabelle, Cousillas, Hugo, Richard, Jean Pierre & Hausberger, Martine. Auditory responses in the HVC of anesthetized starlings. *Brain Research* **1047**, 245–260 (2005).

46. Schmidt, Marc F. & Konishi, Masakazu. Gating of auditory responses in the vocal control system of awake songbirds. *Nature neuroscience* **1**, 513–518 (1998).

47. Arneodo, Ezequiel M., Chen, Shukai, Gilja, Vikash & Gentner, Timothy Q. A neural decoder for learned vocal behavior. *bioRxiv* **193987**, (2017).

48. Lakatos, Peter, Shah, Ankoor S., Knuth, Kevin H., Ulbert, Istvan, Karmos, George, Schroeder, Charles E., Shah, Ankoor S., Knuth, Kevin H., Ulbert, Istvan, Karmos, George & Schroeder, Charles E. An Oscillatory Hierarchy Controlling Neuronal Excitability and Stimulus Processing in the Auditory Cortex. 1904–1911 (2005) doi:10.1152/jn.00263.2005.

49. Ganji, Mehran, Kaestner, Erik, Hermiz, John, Rogers, Nick, Tanaka, Atsunori, Cleary, Daniel, Lee, Sang Heon, Snider, Jospeh, Halgren, Milan, Cosgrove, Garth Rees, Carter, Bob S., Barba, David, Uguz, Ilke, Malliaras, George G., Cash, Sydney S., Gilja, Vikash, Halgren, Eric & Dayeh, Shadi A. Development and Translation of PEDOT:PSS Microelectrodes for Intraoperative Monitoring. *Advanced Functional Materials* 1700232 (2017) doi:10.1002/adfm.201700232.

50. Hermiz, John, Rogers, Nick, Kaestner, Erik, Ganji, Mehran, Cleary, Dan, Snider, Joseph, Barba, David, Dayeh, Shadi, Halgren, Eric & Gilja, Vikash. A clinic compatible, open source electrophysiology system. *Proceedings of the Annual International Conference of the IEEE Engineering in Medicine and Biology Society, EMBS* **2016-Octob**, 4511–4514 (2016).

51. Siegle, Joshua H., López, Aarón Cuevas, Patel, Yogi A., Abramov, Kirill, Ohayon, Shay & Voigts, Jakob. Open Ephys: An open-source, plugin-based platform for multichannel electrophysiology. *Journal of Neural Engineering* **14**, (2017).

52. Pachitariu, Marius, Steinmetz, Nick, Kadir, Shabnam, Carandini, Matteo & Harris, Kenneth. Fast and accurate spike sorting of high-channel count probes with KiloSort. *Advances in Neural Information Processing Systems* 4455–4463 (2016).

53. Rossant, Cyrille, Kadir, Shabnam N., Goodman, Dan F. M., Schulman, John, Hunter, Maximilian L. D., Saleem, Aman B., Grosmark, Andres, Belluscio, Mariano, Denfield, George H., Ecker, Alexander S., Tolias, Andreas S., Solomon, Samuel, Buzski, György, Carandini, Matteo & Harris, Kenneth D. Spike sorting for large, dense electrode arrays. *Nature Neuroscience* **19**, 634–641 (2016).

54. Selinger, Jonathan V., Kulagina, Nadezhda V., O'Shaughnessy, Thomas J., Ma, Wu & Pancrazio, Joseph J. Methods for characterizing interspike intervals and identifying bursts in neuronal activity. *Journal of Neuroscience Methods* **162**, 64–71 (2007).

55. Kreuz, Thomas, Chicharro, Daniel, Houghton, Conor, Andrzejak, Ralph G. & Mormann, Florian. Monitoring spike train synchrony. *Journal of Neurophysiology* **109**, 1457–1472 (2013).

56. George, I., Cousillas, H., Richard, J. P. & Hausberger, M. New insights into the auditory processing of communicative signals in the HVC of awake songbirds. *Neuroscience* **136**, 1–14 (2005).

57. Margoliash, D. Preference for autogenous song by auditory neurons in a song system nucleus of the white-crowned sparrow. *Journal of Neuroscience* **6**, 1643–1661 (1986).

58. Margoliash, D. & Fortune, E. S. Temporal and harmonic combination-sensitive neurons in the zebra finch's HVc. *Journal of Neuroscience* **12**, 4309–4326 (1992).

59. Buzsáki, György, Anastassiou, Costas A. & Koch, Christof. The origin of extracellular fields and currents — EEG , ECoG , LFP and spikes. **13**, 407–420 (2012).

60. Benezra, Sam E., Narayanan, Rajeevan T., Egger, Robert, Oberlaender, Marcel & Long, Michael A. Morphological characterization of HVC projection neurons in the zebra finch (Taeniopygia guttata). *Journal of Comparative Neurology* **526**, 1673–1689 (2018).

61. Khodagholy, Dion, Gelinas, Jennifer N., Zhao, Zifang, Yeh, Malcolm, Long, Michael, Greenlee, Jeremy D., Doyle, Werner, Devinsky, Orrin & Buzsáki, György. Organic electronics for high-resolution electrocorticography of the human brain. *Science Advances* **2**, (2016).

62. Hill, Mackenna, Rios, Estefania, Sudhakar, Shyam Kumar, Roossien, Douglas H., Caldwell, Ciara, Cai, Dawen, Ahmed, Omar J., Lempka, Scott F., Cynthia, A., Arbor, Ann, Arbor, Ann, Arbor, Ann, Arbor, Ann, Arbor, Ann, Arbor, Ann & Arbor, Ann. Quantitative simulation of extracellular single unit recording from the surface of cortex. *J Neural Eng* **15**, 1–25 (2018).

63. Tsytsarev, Vassiliy, Taketani, Makoto, Schottler, Frank, Tanaka, Shigeru & Hara, Masahiko. A new planar multielectrode array: Recording from a rat auditory cortex. *Journal of Neural Engineering* **3**, 293–298 (2006).

64. Spira, Micha E., Shmoel, Nava, Huang, Shun Ho M. & Erez, Hadas. Multisite attenuated intracellular recordings by extracellular multielectrode arrays, a perspective. *Frontiers in Neuroscience* **12**, 1–8 (2018).

65. Jonak, Carrie R., Lovelace, Jonathan W., Ethell, Iryna M., Razak, Khaleel A. & Binder, Devin K. Reusable multielectrode array technique for electroencephalography in awake freely moving mice. *Frontiers in Integrative Neuroscience* **12**, 1–9 (2018).

66. Insanally, Michele, Trumpis, Michael, Wang, Charles, Chiang, Chia Han, Woods, Virginia, Palopoli-Trojani, Kay, Bossi, Silvia, Froemke, Robert C. & Viventi, Jonathan. A low-cost, multiplexed μECoG system for high-density recordings in freely moving rodents. *Journal of Neural Engineering* **13**, 0–37 (2016).

67. Chacron, M. J., Longtin, A. & Maler, L. Negative interspike interval correlations increase the neuronal capacity for encoding time-dependent stimuli. *The Structure of Large-Scale Synchronized Firing in Primate Retina* **21**, 5328–5343 (2001).

68. Lindner, Benjamin, Chacron, Maurice J. & Longtin, Andre. Integrate-and-fire neurons with threshold noise: A tractable model of how interspike interval correlations affect neuronal signal transmission. *Phys Rev E Stat Nonlin Soft Matter Phys* **72**, 2 Pt 1 (2005).

69. Kröner, Sven & Güntürkün, Onur. Afferent and efferent connections of the caudolateral neostriatum in the pigeon (Columba uvia): A retro- and anterograde pathway tracing study. *Journal of Comparative Neurology* **407**, 228–260 (1999).

70. Starosta, Sarah, Güntürkün, Onur & Stüttgen, Maik C. Stimulus-Response-Outcome Coding in the Pigeon Nidopallium Caudolaterale. *PLoS ONE* **8**, (2013).

71. Jeanne, James M., Sharpee, Tatyana O. & Gentner, Timothy Q. Associative learning enhances population coding by inverting inter-neuronal correlation patterns. *Neuron* **78**, 352–363 (2013).

72. Mitchell, Jude F., Sundberg, Kristy A. & Reynolds, John H. Differential Attention-Dependent Response Modulation across Cell Classes in Macaque Visual Area V4. *Neuron* **55**, 131–141 (2007).

73. Yeager, John D., Phillips, Derrick J., Rector, David M. & Bahr, David F. recording in awake rats. *J Neurosci Methods* **173**, 279–285 (2009).

74. Tybrandt, Klas, Khodagholy, Dion, Dielacher, Bernd, Stauffer, Flurin, Renz, Aline F., Buzsáki, György & Voros, Janos. High-density stretchable electrode grids for chronic neural recording. *Advanced Materials* **30**, 1706520 (2018).

75. Quairiaux, Charles, Armstrong-james, Michael & Welker, Egbert. Modified Sensory Processing in the Barrel Cortex of the Adult Mouse After Chronic Whisker Stimulation. *Journal of neurophysiology* **97**, 2130–2147 (2007).

76. Webber, Roxanna M. & Stanley, Garrett B. Nonlinear Encoding of Tactile Patterns in the Barrel Cortex. *Journal of Neurophysiology* **91**, 2010–2022 (2004).

77. Higley, Michael J. & Contreras, Diego. Cellular Mechanisms of Suppressive Interactions Between Somatosensory Responses In Vivo. *Journal of Neurophysiology* **97**, 647–658 (2007).

78. Civillico, Eugene F. & Contreras, Diego. Integration of Evoked Responses in Supragranular Cortex Studied With Optical Recordings In Vivo. *Journal of Neurophysiology* **96**, 336–351 (2006).

79. Civillico, E. F. & Contreras, D. Comparison of Responses to Electrical Stimulation and Whisker Deflection Using Two Different Voltage-sensitive Dyes in Mouse Barrel Cortex in Vivo. *J Membrane Biol.* **208**, 171–182 (2005).

80. Gorski, Jessica A., Talley, Tiffany, Qiu, Mengsheng, Puelles, Luis, Rubenstein, John L. R. & Jones, Kevin R. Cortical excitatory neurons and glia, but not GABAergic neurons, are produced in the Emx1-expressing lineage. *Journal of Neuroscience* **22**, 6309–6314 (2002).

81. Madisen, Linda, Mao, Tianyi, Koch, Henner, Zhuo, Jia min, Berenyi, Antal, Fujisawa, Shigeyoshi, Hsu, Yun Wei A., Garcia 3rd, Alfredo J., Gu, Xuan, Zanella, Sebastien, Kidney, Jolene, Gu, Hong, Mao, Yimei, Hooks, Bryan M., Boyden, Edward S., Buzsáki, György, Ramirez, Jan Marino, Jones, Allan R., Svoboda, Karel, *et al.* A toolbox of Cre-dependent optogenetic transgenic mice for light-induced activation and silencing. *Nature neuroscience* **15**, 793–802 (2012).

82. Dana, Hod, Mohar, Boaz, Sun, Yi, Narayan, Sujatha, Gordus, Andrew, Hasseman, Jeremy P., Tsegaye, Getahun, Holt, Graham T., Hu, Amy, Walpita, Deepika, Patel, Ronak, Macklin, John J., Bargmann, Cornelia I., Ahrens, Misha B., Schreiter, Eric R., Jayaraman, Vivek, Looger, Loren L., Svoboda, Karel & Kim, Douglas S. Sensitive red protein calcium indicators for imaging neural activity. *eLife* **5**, 1–24 (2016).

83. Tamamaki, Nobuaki, Yanagawa, Yuchio, Tomioka, Ryohei, Miyazaki, Jun Ichi, Obata, Kunihiko & Kaneko, Takeshi. Green fluorescent protein expression and colocalization with calretinin, parvalbumin, and somatostatin in the GAD67-GFP knock-in mouse. *J Comp Neurol.* **467**, 60–79 (2003).

84. Nimmerjahn, Axel, Kirchhoff, Frank, Kerr, Jason N. D. & Helmchen, Fritjof. Sulforhodamine 101 as a specific marker of astroglia in the neocortex in vivo. *Nature Methods* **1**, 31–37 (2004).

85. Hermiz, John, Hossain, Lorraine, Arneodo, Ezequiel M., Ganji, Mehran, Rogers, Nicholas, Vahidi, Nasim, Halgren, Eric, Gentner, Timothy Q., Dayeh, Shadi A. & Gilja, Vikash. Stimulus Driven Single Unit Activity From Micro-Electrocorticography. *Frontiers in Neuroscience* **14**, (2020).

86. Paulk, Angelique, Yang, Jimmy, Cleary, Daniel, Soper, Daniel, Lee, Sang Heon, Ganji, Mehran, Ro, Yun Goo, Oh, Hongseok, Hossain, Lorraine, Rogers, Nick, Kiliç, Kivilcim, Ryu, Sang Baek, Lee, Seung Woo, Hermiz, John, Gilja, Vikash, Lee, Jong Woo, Maus, Douglas, Devor, Anna, Fried, Shelley, *et al.* Microscale physiological events on the human cortical surface detected with PEDOT:PSS Electrodes. *bioRxiv* (2019) doi:10.1101/770743.